Universitat de Girona

CHARACTERIZATION AND OPTIMIZATION OF DISPERSED COMPOSITE LAMINATES FOR DAMAGE RESISTANT AERONAUTICAL STRUCTURES

Tamer Ali Abdella SEBAEY ABDELLA

UNIVERSITAT DE GIRONA

PHD THESIS

CHARACTERIZATION AND OPTIMIZATION OF
DISPERSED COMPOSITE LAMINATES FOR
DAMAGE RESISTANT AERONAUTICAL
STRUCTURES

TAMER ALI ABDELLA SEBAEY ABDELLA

2012

UNIVERSITAT DE GIRONA

PHD THESIS

CHARACTERIZATION AND OPTIMIZATION OF DISPERSED COMPOSITE LAMINATES FOR DAMAGE RESISTANT AERONAUTICAL STRUCTURES

TAMER ALI ABDELLA SEBAEY ABDELLA

2012

TECHNOLOGY DOCTORATE PROGRAM

ADVISORS

DR. NORBERT BLANCO
Universitat de Girona, Spain

DR. CLÁUDIO SAÚL LOPES
IMDEA Materials, Spain

A thesis submitted for the degree of Doctor of Philosophy by the Universitat de Girona

To whom it might concern,

Dr. Norbert Blanco, Associate Professor at the *Universitat de Girona* of the Department of *Enginyeria Mecànica i de la Construcció Industrial,* and Dr. Cláudio Saúl Lopes, Researcher at the *IMDEA Materials,*

CERTIFY that the study entitled *Characterization and Optimization of Dispersed Composite Laminates for Damage Resistant Aeronautical Structures* has been carried out under their supervision by Tamer Ali Abdella Sebaey Abdella to apply for the doctoral degree with the European Mention. We also certify that Tamer Ali Abdella Sebaey Abdella was a full time graduate student at Universitat de Girona, Girona, Spain, from October 2009 to present.

Dr. Norbert Blanco
Universitat de Girona, Spain

Dr. Cláudio Saúl Lopes
IMDEA Materials, Spain

IN THE NAME OF ALLAH

To the New Family Member
AHMED TAMER SEBAEY

Acknowledgements

I would like to express my gratitude to my advisors, Dr. Norbert Blanco and Dr. Cláudio Lopes, for the indefatigable help and for the key contributions that have allowed the development of the present thesis.

I would like to thank also the help received from Prof. Josep Costa, Prof. Joan Andreu Mayugo, Dr. Albert Turon, Dr. Pere Maimi, Dr. Dani Trias, Dr. Jordi Renart, Dr. Marc Gascons and Dr. Emilio González, who spent a lot of time making the work easy and clarified many things, not only related to composite materials, also in many other things which are required to continue forward. This help has existed always, since the first day that I started to work with the research group AMADE on Monday 4$^{\text{th}}$ of October 2009.

I have to do a special mention to my friends Giuseppe Catalanotti, Hilal Ercin, Miguel Bessa and Antóonio Melro, with whom I have shared great moments and I have learned a lot from them during my research stages at the INEGI of the University of Porto. In addition, I will not ever forget our discussions with Prof. Pedro Camanho during this research stay.

Of course, I am grateful to all members of the research group AMADE of the University of Girona for the help and nice moments that I have received from each one.

I would also like to thank my family for the support they provided me through my entire life and in particular, I must acknowledge my parents, my wife Heba and my kids Sama and Omar for their support and being without me for a long time throughout my stay in Girona.

Funding

Publications

The papers published and submitted during the development of this thesis are listed below:

1. **T.A. Sebaey**, C.S. Lopes, N. Blanco and J. Costa. Ant Colony Optimization for dispersed laminated composite panels under biaxial loading. *Composites Structures*, Vol. 92: pp. 31-36, 2011.

2. **T.A. Sebaey**, N. Blanco, C.S. Lopes and J. Costa. Numerical investigation to prevent crack jumping in Double Cantilever Beam tests of multidirectional composite laminates. *Composites Science and Technology*, Vol. 71: pp. 1587-1592, 2011.

3. **T.A. Sebaey**, N. Blanco, J. Costa and C.S. Lopes. Characterization of crack propagation in mode I delamination for multidirectional CFRP laminates. *Composites Science and Technology*, Vol. 72: pp. 1251-1256, 2012.

4. **T.A. Sebaey**, E.V. González, C.S. Lopes, N. Blanco and J. Costa. Damage resistance and damage tolerance of dispersed CFRP laminated: Design and optimization. *Composite Structures*, In Press 2012.

5. **T.A. Sebaey**, C.S. Lopes, N. Blanco and J. Costa. Two-pheromone Ant Colony optimization to design dispersed laminates for aeronautical structure applications. *Computers & Structures*, Submitted Dec. 2011.

6. **T.A. Sebaey**, E.V. González, C.S. Lopes, N. Blanco, P. Maimí and J. Costa. Damage resistance and damage tolerance of dispersed CFRP laminates: Effect of the mismatch angle between plies. *Composites Science & Technology*, Submitted Oct. 2012.

List of Symbols

Symbol	Description
A_d	The projected delamination area
B_t	Parameter to indicate the skewness of the crack profile due to bending/twisting coupling
C	The load line compliance (delamination tests)
CO	The normalized crack opening
D^*	The plate effective bending stiffness
D_C	Parameter to indicate the curvature due to longitudinal/transverse bending coupling
D_{ij}	The bending stiffness matrix coefficients
E_{11}	Unidirectional modulus of elasticity in the fiber direction
E_{22}	Unidirectional modulus of elasticity in the transverse to fiber direction
E_i	The impact energy
F_{d1}^{stat}	The threshold delamination load for single delamination
F_{dn}^{stat}	The threshold delamination load for arbitrary number of delaminations
FI_{FC}	Fiber compression failure index
FI_{FT}	Fiber tensile failure index
FI_{MC}	Matrix compression failure index
FI_{MT}	Matrix cracking failure index under tensile loading
$\bar{F}_{max}$	Maximum normalized impact force

Symbol   Description

Symbol	Description
F_{per}^{sh}	The perforation threshold load
g	The fracture toughness ratio
G_{12}	Unidirectional shear modulus of elasticity
G_{Ic}	Fracture toughness under mode I delamination
G_{IIc}	Fracture toughness under mode II delamination
G_{IIIc}	Fracture toughness under mode III delamination
H_i	The impactor drop height
h	The plate thickness
K_{bs}	The plate bending-shear stiffness
K_α	The contact stiffness
M_i	Impactor mass
M_p	Plate mass
N	The load block correction factor (delamination tests)
OOS	The crack front out of symmetry
p and q	The number of half waves in both x and y direction under biaxial compression
Q_α	The effective contact modulus
R_i	The impactor radius
S_{is}^L	In situ longitudinal shear strength
S^L	Unidirectional shear strength
S^T	The transverse shear strength
$\bar{t}$	The normalized contact time
V_0	The initial impactor velocity
X^C	Unidirectional Compressive strength in the fiber direction
X^T	Unidirectional tensile strength in the fiber direction
Y^C	Unidirectional Compressive strength in the transverse to fiber direction
Y_{is}^T	In situ transverse tensile strength

Symbol   Description

Symbol	Description
Y^T	Unidirectional tensile strength in the transverse to fiber direction
α	A parameter to denote the degree of importance of pheromone
β	The non-linearity of shear stress shear strain relation parameter
ε_{ij}^{all}	The allowable strain vector
ζ	A parameter used to control the pheromone level
ζ_w	The loss factor, relative plate mobility or inelastic parameter
λ	The relative stiffness (low velocity impact)
λ_c	The load multiplier factor in biaxial in-plane loading
λ_v	The crack front visual deviation
ρ	The pheromone evaporation rate
σ_{ij}	The components of the stress vector
τ_{ij}	The pheromone matrix components
ν_{12}	Unidirectional Poisson's ratio

List of Acronyms

Acronym	Description
ADCB	Asymmetric Double Cantilever Beam
ADL	The Allowable Damage Limit
AFP	Automated Fiber Placement
AITM	AIrbus Test Method
AC	Ant Colony (optimization algorithm)
ASTM	American Society for Testing Materials
BVID	Barely Visible Impact Damage
CAI	Compression After Impact
CDT	The Critical Damage Threshold
CFRP	Carbon Fiber Reinforced Plastic
DCB	Double Cantilever Beam
FE	Finite Element
FAR	Federal Aviation Administration
GA	Genetic Algorithms (An optimization algorithm)
GP	Generalized Pattern (An optimization algorithm)
JAR	Joint Aviation Requirements
LaRC	Langley Research Center
LEFM	Linear Elastic Fracture Mechanics
NDI	Non-Destructive Inspection
PS	Particle Swarm (An optimization algorithm)
SA	Simulated Annealing (An optimization algorithm)
SS	Scatter Search (An optimization algorithm)
TS	Tabu-Search (An optimization algorithm)

Acronym	Description
VCCT	Virtual Crack Closure Technique
VUMAT	User MATerial subroutine (Abaqus/Explicit code)

List of Figures

List of Tables

Contents

Resum

Els materials compòsits són àmpliament emprats en la fabricació de components pel sector aeronàutic. En l'actualitat s'està posant molt d'interès en les propietats dels laminats no-convencionals com a una tècnica molt prometedora en substitució dels laminats convencionals. El terme laminat no-convencional fa referència aquells laminats amb orientacions de fibra no limitades a 0°, ±45° i 90°. Els laminats no-convencionals es poden classificar en panells amb rigidesa variable (aquells amb trajectòries corbes dels feixos de fibra) i laminats dispersos (aquells amb trajectòries rectilínies dels feixos de fibra però amb orientacions disperses en tot el rang de 0 a 90°). Des del punt de vista de la fabricació, aquests tipus de laminats es poden fabricar de forma senzilla emprant la tecnologia del posicionament automatitzat de fibra (Automated Fibre Placement) ja que permet un total control sobre el posicionament dels feixos de fibra. Aquestes dues possibilitats, activades pel desenvolupament de les noves tecnologies de fabricació, amplien enormement les possibilitats de disseny dels compòsits avançats. Aquesta tesi es centra únicament en els laminats dispersos.

El principal objectiu de la tesi és valorar la resistència al dany i la tolerància al dany dels laminats no-convencionals dispersos i comparar la seva resposta amb la dels laminats convencionals. No obstant, part de l'atenció es dedica a comprendre el comportament de la delaminació en laminats multidireccionals. En la primera part de la tesi, s'analitza la delaminació en laminats multidireccionals. L'objectiu és dissenyar una seqüència d'apilament apropiada per evitar el dany intralaminar (migració de la delaminació) i permetre la caracterització de la tenacitat a la fractura en mode I. El resultats d'aquest estudi mostren que a major rigidesa a flexió dels braços de l'esquerda, menor és la tendència a la migració de l'esquerda. Aquest aspecte també s'ha analitzat experimentalment, obtenint les mateixes conclusions.

En la segona part de la tesi, s'utilitza l'algoritme d'optimització basat en les

colònies de formigues (Ant Colony Optimization) per dissenyar la seqüència d'apilament de compòsits laminats sota diferents condicions de càrrega. Les prediccions de resposta dels laminats dispersos es comparen amb les dels laminats convencionals sota estats de càrrega biaxials a tracció i compressió i impactes de baixa velocitat. En general, es detecta una millora en el comportament dels laminats dispersos respecte el dels laminats convencionals.

La revisió bibliogràfica de les formulacions analítiques per impactes de baixa velocitat en plaques laminades permet concloure que la diferència d'angles entre dues capes adjacents no influeix la resistència a l'impacte. Per tal d'avaluar aquesta idea, s'analitza experimentalment i es compara el comportament de dos laminats dispersos i un laminat convencional front a un impacte de baixa velocitat i la compressió després d'impacte. Les tres configuracions són optimitzades amb la mateixa rigidesa però amb diferents diferències d'angles entre làmines adjacents. Els resultats mostren una gran avantatge del laminat no-convencional amb menor divergència d'angles entre làmines pel que fa a indentació, energia absorbida, grandària de la delaminació i resistència residual, és a dir, tolerància al dany i resistència al dany.

Summary

Composite materials are extensively used in aeronautical composite parts. Nowadays, huge effort is oriented to the characteristics of non-conventional laminates as a promising technology to replace the conventional ones. The term non-conventional laminates correspond to those ones with fiber orientations not limited to 0°, ±45° and 90°. Non-conventional laminate can be divided into variable stiffness panels (in which the fiber path is curved) and dispersed laminates (where straight fibers are used but at angles dispersed throughout the whole 0-90° range). From the manufacturing point of view, these types of laminates can be easily manufactured using the fiber placement technology that allows steering of fibers. These two possibilities, triggered by the development of manufacturing technologies, greatly increase the design space of the advanced composites. The current thesis is only focussed on dispersed laminates.

The main objective of the thesis is to assess the damage resistance and damage tolerance of the non-conventional dispersed laminates and compare the response with the conventional ones. However, part of the effort is spent on understanding the delamination behavior in multidirectional laminates. In the first part of the thesis, the delamination in multidirectional laminates is studied. The objective is to design a proper stacking sequence, capable of avoiding intralaminar damage (crack jumping), to enable the fracture toughness characterization under pure mode I. The result of this study shows that the higher the crack arm bending stiffness, the lower the tendency to crack jumping. This phenomenon is also studied experimentally and the same conclusion is drawn.

In the second part of this thesis, the Ant Colony Optimization algorithm is used to tailor the stacking sequence of laminated composites under different loading conditions. The predicted responses of dispersed laminates are compared to the

conventional ones under biaxial tensile and compression loadings, and low velocity impact. Usually, there is a certain performance improvement by using the dispersed laminates when compared to the conventional ones.

The state-of-art of the analytical formulations on laminated plates under low velocity impact concludes that no relevant effect on impact resistance has been attributed to the mismatch angle between the orientation of each two adjacent plies. In order to evaluate this assumption, the behavior of two dispersed laminates under low velocity impact and compression after impact is studied experimentally and compared with the behavior of one conventional laminate. The three configurations are optimized to the same stiffness but different mismatch angles between adjacent plies. The results show a great advantage to the laminate with small mismatch angle in terms of indentation, absorbed energy, delamination size and residual strength, i.e. damage tolerance and damage resistance.

Chapter 1

Introduction and objectives

1.1 General Introduction

The history of composite materials can be dated back to the third Egyptian dynasty, in around 2780 B.C. The Egyptians realized that wood could be manipulated to achieve superior strength and resistance to thermal expansion as well as to swelling in the presence of moisture. Later, straw was used by the Egyptians, as well as the ancient Chinese, to strengthen mud bricks. By the end of World War II and later, high-performance fiber reinforced composites were being used extensively in weight-sensitive applications such as automotive, aircraft, and space vehicles [1–3].

Modern polymeric structural composites, frequently referred to as *Advanced Composites*, are a blend of two or more components, one of which is made up of stiff fibers, and the other, a binder or matrix which holds the fibers in place and transfers the load between the load carriers. The fibers are strong and stiff relative to the matrix and are generally orthotropic (having different properties in two different directions). The fiber, for advanced structural composites, is long, with length to diameter ratios of over 100. The fibers' strength and stiffness are usually much greater, several times more, than those of the matrix material. When the fiber and the matrix are joined to form a composite they retain their individual identities and both directly influence the composite's final properties. The resulting composite is generally composed of layers (laminae) of the fibers and matrix which are stacked to achieve the desired properties in one or more directions [4].

Carbon and glass fibers are the most common reinforcement materials. The ad-

vantages of fiberglass are its high tensile strength and strain to failure, but heat and fire resistance, chemical resistance, moisture resistance and thermal and electrical properties are also cited as reasons for its use. It is by far the most widely used fiber, primarily because of its low cost. However, their mechanical properties are not comparable with carbon fibers. Carbon fibers have demonstrated the widest variety of strengths and modulii and have the greatest number of suppliers [4], in spite of, their higher production and processing costs.

The overall properties of the composite strongly depend on the way the fibers are laid in the composites. Reinforcing fibers are found in different forms, from long continuous fibers to woven fabric and short chopped fibers. The fibre form is selected depending on the type of application (structural or nonstructural) and manufacturing method. For structural applications, continuous fibers or long fibers are recommended whereas, chopped fibres are recommended for non structural applications [5].

Modern composite materials have superior properties when compared to metals. These properties include high specific strength and stiffness, reducing structural weight, high wear resistance, good fatigue properties, excellent corrosion and chemical resistance, high dimensional stability, viscoelastic properties that reduce noise and the flexibility in designing complex shapes. Because of these properties, composite materials have the potential to replace widely used steel and aluminum. Replacing steel components with composite ones can save 60% to 80% in component weight, and 20% to 50% weight by replacing aluminum parts [6]. To this end, composites are being used extensively in aeronautical application.

1.2   Aeronautical Laminated Composites

The world energy supply has crossed a no-return threshold, because the era of "cheap oil" has ended. The design and production of lighter structural components is, nowadays, an economical and environmental demand. Accordingly, a lot of research effort is directed towards aeronautical composite structures, especially in Carbon Fiber Reinforced Plastics (CFRP), to be the main structural components in modern aircraft. Airbus, as one of the most important aircraft manufacturers, has a long history with composite materials that are used in aircraft design and

construction. The evolution of the use of composites in Airbus aircraft is shown in Figure 1.1(a) [7]. The same trend has also been adopted by Boeing (see for example the amount of carbon composites in the B787 commercial airplane, Figure 1.1(b)).
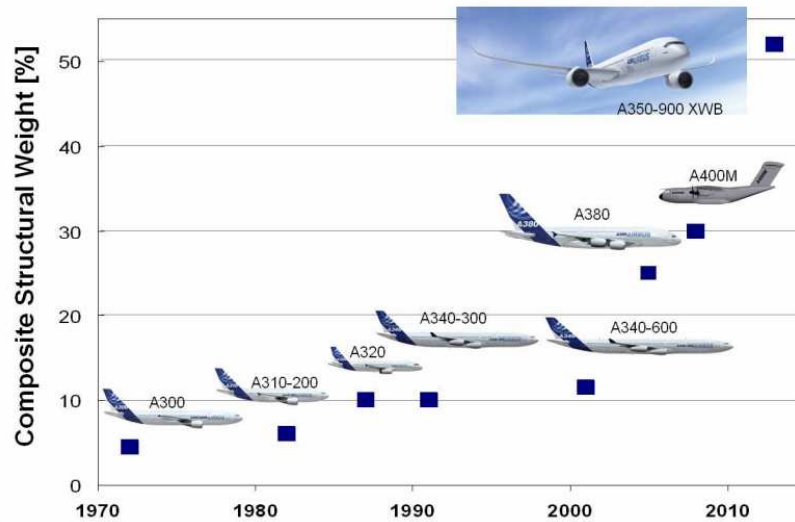
(a) Increase in Airbus composite parts as percentage of total aircraft weight (after [7])
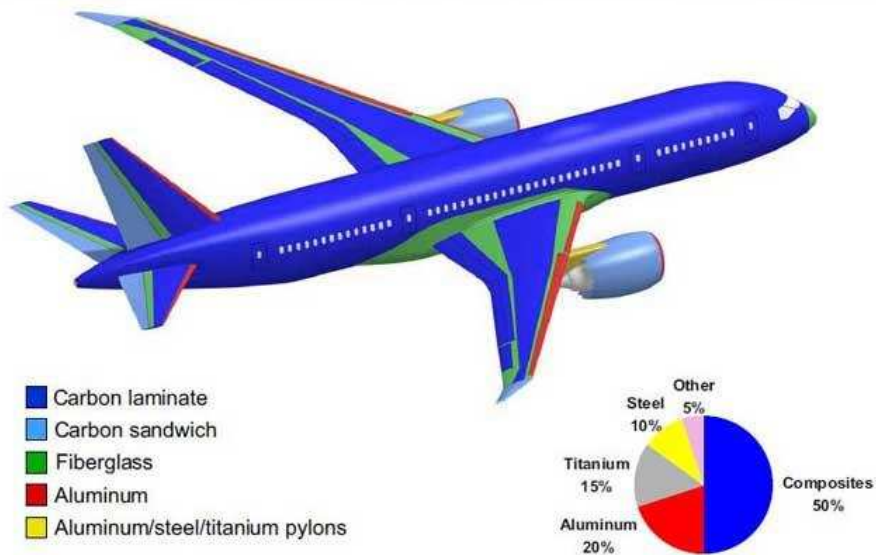
(b) Materials used in Boeing B787 aircraft (after [8])

Figure 1.1: Composite materials in aeronautical industry.

General guidelines to design an efficient aeronautical composite part were given by Baker et al. [9]. These guidelines include:

- Use balanced laminates to avoid warping

- A minimum fiber content of 55% by volume should be used

- A minimum of 10% of plies shall be used in each of the principal directions

- Use a maximum of four adjacent plies in any one direction

- Place $\pm 45°$ plies on the outside surfaces of shear panels to increase resistance to buckling

- Avoid highly directional laminates in regions around holes or notches

- Avoid manufacturing techniques that result in poor fiber alignment

- Minimize the number of joints by designing large components or sections

- Allow for repair in the design

Traditional manufacturing techniques, such as hand lay-up, spray-up, filament winding, pultrusion, resin transfer molding and injection molding [6], are still used in aeronautical composites. However, to reach the requirements and guidelines summarized in the former paragraph, the manufacturing techniques and procedures should be developed and optimized for both quality and manufacturing costs. Automated fiber laying and fiber placement technology grew rapidly in the 1970s and 1980s as a better means of laying up prepreg materials in terms of both precision and production rate. Compared to the other techniques, fiber placement is often used for high performance structures where the fiber path within a given layer is designed to be laid down more precisely to be in conformance to the major local load conditions [10].

1.3   Automated Manufacturing

The development of manufacturing and tooling of aircraft composites led to advanced fiber placement technology. The aerospace industry has responded to the low cost composites challenge by developing innovating manufacturing techniques, such as producing unitized parts with automated processes. The most significant

technology promising reduced cost fabrication is the fiber placement process, which allows large and complex shaped composite structures to be produced faster, approximately 40% cheaper, and with greater quality compared to traditional approaches. Fiber placement has been used to manufacture military hardware such as the duct of the Joint Strike Fighter and the landing gear pod fairing of the C-17 transport, as well as lighter aircraft for civil aviation [11].

An advanced fiber placement machine is a high-precision robot, capable of wide freedom of movement, and is computer-controlled to produce a composite component, Figure 1.2. Off-line programming is used to implement the desired configurations. The technology permits the design and production of components that would be extremely difficult or even impossible with other automated methods, let alone hand laying. Despite the novelty of the process and high machinery costs, the availability of automated fiber placement and tow-placement systems is rapidly growing [12, 13].

(a) The robot arm (after [14])   (b) The placement head (after [15])
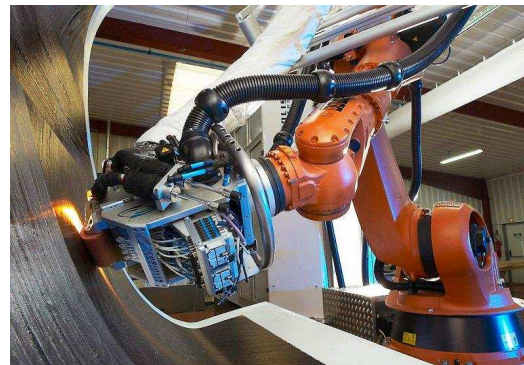
Figure 1.2: Fiber placement technology.

The primary advantage of fiber placement over manual lay-up of a composite part results from the automation of the manufacturing process. By automating the fibre laying procedure, the process repeatability is greatly improved, hence its speed is increased. Bullock et al. [13] estimate the fiber placement process to be as much as seven times faster than hand laying. Additionally, a part produced by a machine can be more faithful to the intended design, therefore showing better quality than if produced by hand. It should be mentioned that typical fiber placed parts may generate only from 2% to 15% of scrap, compared with 50% to 100% for conventional

lamination [11]. The head of the fiber placement machine (see Figure 1.2(b)) can move in several degrees of freedom. This wide range of motion allows the tows to be aligned in any direction, enabling the production of both straight and curved fiber composites [16], i.e. more possibilities to tailor the strength and stiffness to meet the different design requirements.

1.4   Non-Conventional Laminates

In spite of the great manufacturing capabilities summarized in Section 1.3, most aeronautical composite parts are built based on a combination of 0°, 90° and ±45° [9]. In some particular cases, fiber orientations such as ±30 and ±60 are also used [17]. However, the full potential of advanced composites can only be achieved by tailoring each laminate to each specific structural application. One way to do this is by turning to "non-conventional" laminates [18–21].

The term non-conventional laminates includes two main categories named dispersed laminates and variable stiffness laminates. In the case of straight fiber panels with ply orientations not limited to 0°, 90° and ±45°, the configuration is called dispersed laminate, Figure 1.3(a). The variable stiffness laminates, introduced by Hyer and Charette [22], were suggested to improve structural response by using curvilinear fiber instead of straight fiber paths. The approach was later generalized by Gürdal and Olmedo [23] by designing variable-stiffness laminates that use continuous curvilinear fiber paths, Figure 1.3(b). For such variable-stiffness panels, the stiffness properties are continuous functions of position. Ideally, by steering the fiber paths, the stiffness properties change at each point, throughout a single layer [24–26].

The variable stiffness concept has attracted far fewer researchers than constant stiffness design due to the higher design and manufacturing costs involved. The higher design cost is due to the inordinately large number of design variables required to define variable orientations and thicknesses as well as additional constraints required for maintaining the continuity in the structure, which in turn implies a need for higher computational resources compared to the constant stiffness design [28].

(a) Dispersed laminate   (b) Tow steered laminate (after [27])
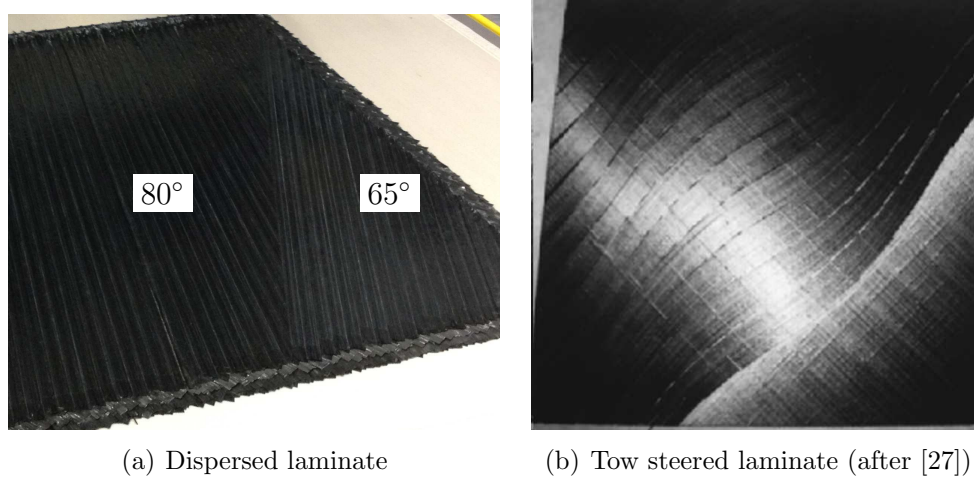
Figure 1.3: Non-conventional laminates.

1.5 Damage Tolerance Concept and Review

Prior to 1958, military airplane designs were based on static strength require-ments. However, numerous structural cracking problems occurred, since material and structural degradation due to repeated loadings were not properly accounted for. The Aircraft Structural Integrity Program (ASIP), initiated in 1958, was based on a fatigue initiation approach and was moderately successful. This essentially safe-life approach was replaced by the fracture mechanics (fatigue crack growth) approach in 1975 which essentially embraces the damage tolerance concept but with strong emphasis on the assumption that imperfections are present in an early stage of airplane service [29]. The idea behind the damage tolerance concept is to as-sess the ability of the airframe to operate safely for a specified period of time with periodic inspections of the airframe [30].

Damage tolerance is the ability of critical structures to withstand a level of service or manufacturing-induced damage or flaws while maintaining its function. However, the goal of this requirement is to allow operation of the aircraft over a specified period of time in order to assure continued safe operation. Safe operation must be possible until the defect is detected by scheduled routine maintenance or, if undetected, for the design life. Again, this requirement addresses a safety issue and applies only to primary structures necessary for safety of flight [30].

For civil aviation, damage tolerance was introduced in 1978. This requirement is

explicitly expressed by the Joint Aviation Requirements (JAR 25.571): "the damage tolerance evaluation of the structure is intended to ensure that should serious fatigue, corrosion, or accidental damage occur within the operational life of the airplane, the remaining structure can withstand reasonable loads without failure or excessive structural deformation until the damage is detected" [31, 32].

Damage tolerance is an integration of the allowable damage level, the propagation of this damage and the detection of this damage through inspection programs. The interactions between these elements define the design quality and the required inspection cost. Figure 1.4 shows interaction of damage tolerance elements and the preferred design characteristics [29].
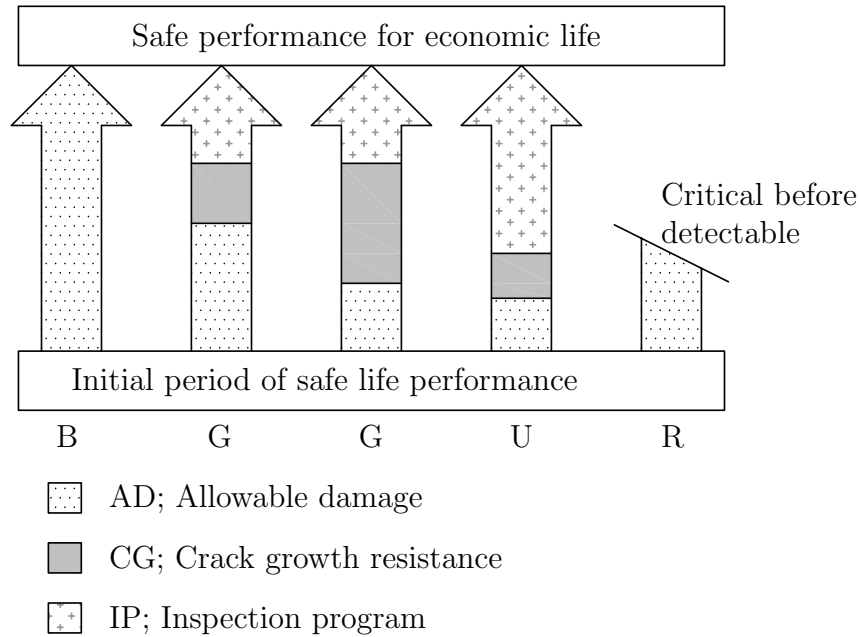
Figure 1.4: Interaction of damage tolerance elements (B: Best design; G: Good design; U: Undesirable inspection cost; R: Requires safe life design).

The allowable damage can be defined as the maximum damage that the structure can sustain under regulatory fail safe loading conditions which is usually higher than the maximum expected load during flight. In the presence of a certain damage, the strength of the structure is called the residual strength. The philosophy of residual strength of composite structures is defined by regulations such as JAR 25 and Federal

Aviation Administration of the United States of America FAR 25 and is illustrated, along general lines, in Figure 1.5.
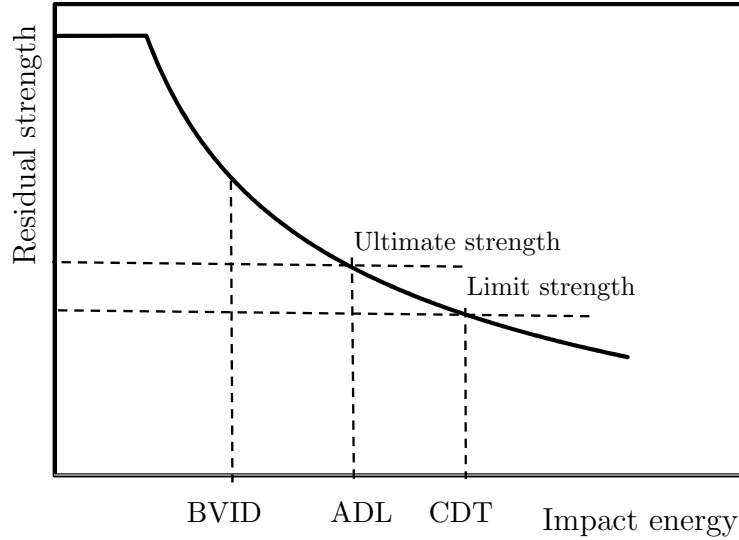
Figure 1.5: Damage tolerance concept. BVID: Barely Visible Impact Damage; ADL: Allowable Damage Limit; CDT: Critical Damage Threshold.

For a given configuration there is an energy threshold below which an impact does not result in any reduction of the structural residual strength. At higher impact energies, the laminate suffers some damage affecting its strength. At a certain energy level, an impact becomes detectable by the local indentation that results from matrix crushing and shear nonlinearity. This is commonly refereed to Barely Visible Impact Damage (BVID). There is no current universally accepted definition of the term BVID. Some authorities accept surface indentations of 1 mm [9] or 0.3 mm [33]. Others give more qualitative requirements, for example, that an indentation be observable from a given distance (say, 1 m) [9].

Although the indentation itself is not critical to the integrity of the part, it indicates underlaying extensive damage which may need to be repaired. This corrective action shall occur before this damage eventually grows (e.g. under the action of fatigue) to a Critical Damage Threshold (CDT) and the margin of safety for the design limit strength is totaly reduced [34]. An impact damage might not need

extensive repair if it is not larger than (and it will not grow more than) the Allow-able Damage Limit (ADL), corresponding to a margin of safety of 0% with respect to the design ultimate strength. These regulations implicate a regular inspection procedure. The residual strength limit, corresponding to the CDT, is such that it should not be violated by impacts within realistically admissible energy levels. In general aeronautical applications, realistic impacts are bounded by a 50 J energy level, except for the horizontal tailplane root, that typically must tolerate impacts up to 140 J [35]. Stronger impacts may be able to cause sufficient matrix cracking and fiber breakage to perforate the laminate altogether and reduce its Compression After Impact (CAI) strength even further. However, there is a lower asymptotic limit for which an increase in impact energy does not result in a larger strength reduction.

Very few impact tests have been conducted on dispersed laminates [19, 36]. The use of dispersed laminates could improve the damage resistance however, its effect on the damage tolerance is not clear. One of the most important features of the dispersed laminates is the mismatch angle between adjacent plies. This feature has not been addressed in the literature for dispersed laminates under low velocity impact loading. However, for conventional laminates, many authors [37–41] studied the mismatch angle/stacking sequence effect. Some articles [38, 42, 43] concluded that the stacking sequence has insignificant effect on the damage resistance of CFRP composites whereas, others [19, 37, 44] showed that the stacking sequence highly affects the damage resistance/tolerance. With respect to the damage tolerance, the stacking sequence effect is not clear [19]. Fuoss et al. [39, 40] recommended to avoid small mismatch angles, whereas Clark [45] and Cantwell et al. [46] concluded that small mismatch angles are desirable to improve the damage tolerance.

It is worth remarking that, in most of the studies found in the literature, the examined stacking sequences have different in-plane and out of plane stiffness. More-over, in some cases, the number of interfaces is not the same. These may add un-desirable effects when studying the mismatch angle effect. Actually, by using the conventional laminates, it is impossible to have two configurations with the same number of interfaces and the same in-plane and out-of-plane stiffness but with a different mismatch angle. This is one more advantage of the dispersed laminates.

The damage mechanisms induced by low velocity impact involves indentation,

matrix cracking, fiber matrix debonding, delamination and, eventually, fiber break-age [33]. These mechanisms can be visually observed on the impacted face in the form of indentation and on the non-impacted face as ply splitting. Internal matrix cracking and fiber breakage at the contact point appear prior to delaminations [38, 47]. The effects of matrix cracking on the residual strength are limited. However, the matrix cracks trigger delaminations which are the major damage mechanism causing degradation of the composite structure properties [48].

The main advantage of using dispersed laminates is the increase in the design space which enable more varieties of configurations. These varieties, given to the designer, can be used to improve the damage resistance and the damage tolerance. As an example, the back face splitting is controlled by the induced bending during impact. To reduce the back face splitting, the designer can increase the bending stiffness at which the splitting can be minimized or even vanished. This increase in the bending stiffness can also increase the delamination threshold load (the load at which many delaminations are instantaneously propagating), if considering the formulation presented in [49, 50].

One of the features of dispersed laminates is the mismatch angle between the individual plies. In conventional laminates the mismatch angle is limited to 90° and 45°, taking into account that plies with the same orientations behave as a single thick ply [51]. In dispersed laminates the mismatch angle can be any value in between 0° and 90° ($0 < \Delta\theta \leq 90$). As can be seen in [52, 53], the delamination resistance in mode II is a function of the mismatch angle. In addition to the fracture toughness, the induced interlaminar shear stresses are also affected by the mismatch angle, i.e. the higher the mismatch angle the higher the interlaminar shear stresses. This means that the mismatch angle controls the main reasons for strength degradation under impact loading. This adds more interest in the dispersed laminates as a promising concept to replace the conventional laminates.

In this thesis, the response of laminated composite plates is optimized and possibility of improving the damage resistance is proved. On the other hand, the effect of the mismatch angle on the damage resistance and tolerance is investigated however, the quantitative effect of the mismatch angle on the fracture toughness under pure mode II is still under investigation.

1.6   Delamination in Multidirectional Laminates

As mentioned in Section 1.5, for an impacted structure, the visible damage (indentation due to matrix plasticity, at the impact point, and ply splitting, at the back face, due to bending) are not the main source of strength degradation. Instead, internal delaminations are usually more severe. The propagation of a certain delamination is believed to be a function of the mismatch angle between the two layers surrounding the crack plan.

According to many authors [52–59], delamination tests for multidirectional layups frequently pose problems because of crack deviations of the delamination from the central plane, Figure 1.6. Some possible forms of these deviations are schematically plotted in Figure 2.2. This problem invalidates the measured fracture values due to the additional intraply damage mechanisms that become involved. For this reason, the interface fracture toughness values (evaluated by the critical energy release rate) measured using UD specimens are still used in the simulations. This may invalidate the numerical predictions.

(a) Jumping in ±45 sequence (After [59])   (b) Jumping in ±60 sequence (After [60])
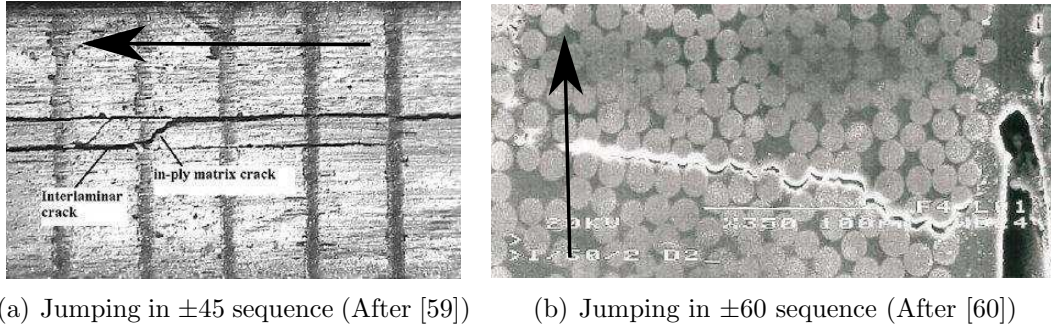
Figure 1.6: Crack jumping phenomenon in double cantilever beam delamination specimens (Crack advance direction is marked with an arrow).

Under pure mode I delamination, multidirectional laminates showed different responses with respect to the fracture toughness data. In some cases [61, 62], it has been concluded that there is an effect of the mismatch angle on the onset fracture toughness whereas, in other cases [63, 64], there is not. The later response is more reasonable because, at the insert tip, the effect of the interface angles is insignificant due to the existence of a resin rich area in front of the insert tip. Moreover, fiber bridging does not affect the onset process and, at the initiation point, the crack front is straight and perpendicular to the crack front advance direction (hence, the crack

(a) Crack branching   (b) Crack Jumping   (c) Double cracking
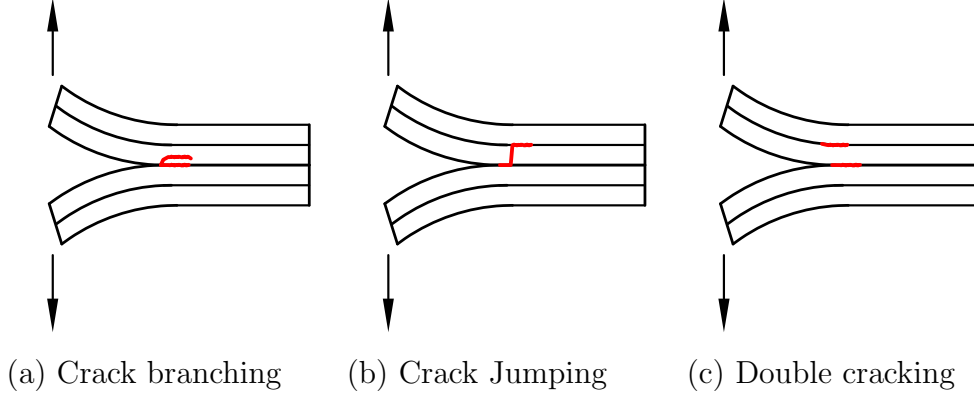
Figure 1.7: Some possible forms of crack deviations (crack propagation path is in red).

front shape effect also vanishes). With respect to the propagation fracture toughness values, the same controversial response is acknowledged. Laksimi et al. [63] and Trakas and Kortschot [65] reported that the dependence of the propagation toughness was insignificant. On the other hand, Robinson and Song [66] and Polaha[67] found a significant effect of the mismatch angle on the propagation toughness.

According to Andersons and König [52], there is a complicated dependence of toughness on interface lay-up and delamination growth direction. High toughness composites appear to exhibit relative interface-independent toughness as opposed to brittle matrix laminates. Similar, although moderate, mode II toughness dependence on the interface angles was recorded.

1.7 Thesis Objectives and Lay-out

As introduced in Section 1.5 The main objective of the current thesis it to optimize the stacking sequence of composite parts for improved response under low velocity impact and compression after impact loading (to assess the damage resistance and the damage tolerance, respectively). However, previous experience [18], showed that the response is highly dependant upon the fracture toughness. For this reason, part of this thesis is directed towards the fracture toughness in multidirectional laminates.

This thesis consists of two parts. In Part I, the delamination in multidirectional laminates is addressed. The objective of this part is to design and test a Double Cantilever Beam (DCB) test specimen capable of avoiding crack jumping in mode I delamination when testing multidirectional laminates. This problem is documented by many authors in the literature[52–59]. In the case of delamination testing with crack jumping, the consumed energy is not only due to delamination. Instead, part of this energy is consumed in intralaminar damage. Avoiding these intralaminar damage mechanisms is important to validate a proper characterization of fracture toughness of multidirectional laminates.

In Chapter 2, a numerical study is conducted, using the Finite Element (FE) method, to design a DCB specimen with a stacking sequence capable of avoiding the crack jumping problems. The analysis adopts the cohesive zone model [68–70] to simulate the interlaminar damage (delamination). The LaRC04 failure criteria [71] is used to check the matrix cracking during crack propagation. The stacking sequence is rejected once the matrix cracking failure index exceeds 1. The effect of including a thermal step in the analysis is also studied. The matrix cracking failure index is found to be a function of the bending stiffness of the beam arm, i.e. the higher the bending stiffness, the lower the matrix cracking failure index.

To test the methodology introduced in Chapter 2, a test matrix is designed and tested and the results are reported in Chapter 3. Six stacking sequences are considered. The bending stiffness is designed to avoid matrix cracking (crack jumping) in five configurations whereas, the sixth is designed with the matrix cracking failure index higher than 1 in order to figure out the crack jumping mechanism. The specimens are tested according to the norm ISO 15024 [72]. The results of this chapter are in agreement with the ones obtained in Chapter 2 (the higher the bending stiffness, the lower the tendency to crack jumping). Moreover, the crack propagation path is monitored using an optical microscope and the results show that delamination is not pure interlaminar fracture mode. Instead, the observation showed light fiber tearing. The fracture toughness value is found to be a function of the interface angle.

The objective of Part II of this thesis is to optimize dispersed laminates with better damage resistance and tolerance compared to the conventional ones. It is assumed, based on the discussion in Section 1.5, that the full potential of advanced

composites can only be obtained by tailoring each laminate to each specific structural application. To achieve the objective of this part, the following tasks are proposed:

- Select and implement an optimization algorithm,

- Test the algorithm for a benchmark problem,

- Review and implement the available analytical formulations of laminated plate under low velocity impact,

- Optimize for better predictable response under transverse impact (based on the available information),

- Assess the damage resistance and damage tolerance of the dispersed laminates, experimentally.

Chapter 4 introduces a short review about the optimization algorithms and their use in composite materials. More detailed reviews can be found in [28, 73]. These reviews show that:

- Gradient direct optimization methods are not suitable for laminated composite applications,

- The enumeration technique can be used only for laminates with small number of layers and combinations of possible fiber orientations,

- Genetic Algorithms (GA) is the most commonly used technique in the optimization of laminated composites,

- The Ant Colony (AC) algorithm is designed for problems at which the design variables are discrete (which is the case of stacking sequence optimization),

- The AC algorithm shows superior response in terms of both the solution quality and the computational costs compared to GA, Simulated Annealing (SA) and Particle Particle Swarm (PS) algorithms.

As a conclusion of the review, the AC algorithm is selected to perform the optimization. Chapter 4 summarizes the algorithm and its implementation to solve the

stacking sequence optimization problem. The algorithm is used to optimize a laminated plate subjected to biaxial tension and compression loading. The dispersed laminates are compared to the conventional ones. A promising response is observed.

In Chapter 5, a review of the analytical formulations of a laminated plate subjected to low velocity impact is presented. These analytical formulations are implemented with the optimization algorithm, introduced in Chapter 4, to design dispersed laminates with improved damage resistance and tolerance, compared to the conventional ones. The problem is solved to minimize the expected damage area and to maximize the energy absorbed in elastic deformations. The results show that this problem is multi-optimum (at the same value of the objective function, there are many stacking sequences capable of satisfying the design constraints).

According to the analytical formulations, the most important characteristic of the laminate is the effective bending stiffness. The mismatch angle between the adjacent plies has no effect on the response. This contradicts the results obtained in Chapter 2 and the dependence of the fracture toughness on the mismatch angle as reported in [53, 66, 67]. To solve this conflict, three configurations are designed with the same equivalent bending stiffness and different mismatch angle and tested in Chapter 6. In the first configuration, the mismatch angle ranges from 5° to 30° whereas, in the second one, the mismatch angle ranges from 60° to 90°. The third configuration is a conventional laminate with mismatch angle of 45°. The three configurations are tested, in ambient conditions, under low velocity impact and compression after impact [74–76]. The results of this chapter show that most of the features of the damage resistance and damage tolerance are dependant on the mismatch angle between the adjacent layers.

Part I

Delamination in Multidirectional CFRP Laminates Under Mode I Loading

Chapter 2

Numerical Simulations

2.1 Overview

During the experimental characterization of the mode I interlaminar fracture toughness of multidirectional composite laminates, the crack tends to migrate from the propagation plane (crack jumping) or to grow asymmetrically, invalidating the tests. This phenomenon has been already explained in Section 1.6.

The main objective of the present chapter is to define, with the aid of numerical tools, a stacking sequence able to avoid migration of the interlaminar crack and to cause a symmetric crack front in multidirectional DCB test specimens. A set of stacking sequences, ranging from very flexible to very stiff is analyzed. This analysis is undertaken by means of the Finite Element Method (FEM), considering a cohesive interface to simulate delamination. The tendency to crack jumping is evaluated with the failure index associated to matrix cracking by considering physically-based failure criteria (LaRC04 failure criteria). The symmetry of the crack front and the effect of residual thermal stresses are also investigated.

2.2 Introduction

Laminated composites can fail under many modes, such as fiber failure, matrix cracking, fiber matrix debonding, fiber pull-out and delamination. Delamination is one of the most dangerous failure mechanisms for composite laminates. While a number of experimental studies indicate that the most conservative toughness values

are produced by testing unidirectionally reinforced composites by propagating the interlaminar crack in the fiber direction, the dependency of the mentioned material property on the interface lay-up and on the direction of the interlaminar crack propagation with respect to the reinforcement directions of the adjacent plies is not clearly defined [52, 53]. Some authors [53, 77] concluded that fracture toughness is highly dependent on the interface angles while others [63, 78] mentioned that there is no such dependency. All the experimental evidence suggests that the occurrence of crack jumping (crack plane migration) has an effect upon the load displacement curve, which leads to unrealistic fracture toughness values. The values extracted from such experiments cannot be considered as objective material properties [52]. de Morais et al. [54] suggested that the main factor influencing crack jumping is the bending stiffness of the crack beam.

Several trials were reported in the literature to overcome crack jumping. Robinson and Song [66] proposed a specimen with a pre-delaminated edge, Figure 2.1(a). Another specimen, with side grooving at the delamination front, Figure 2.1(b), was proposed by Hunston and Bascom [58]. Prombut et al. [79] proposed asymmetric crack arms. Such specimens succeeded to overcome the crack jumping for some cases, [52, 78]. However, the problem associated with these specimens is the difficulty of monitoring the crack front and/or length through its progression which leads to inaccurate propagation toughness values. By using asymmetric crack arms, Pereira and de Morais [80] studied the fracture between three different interfaces using the mixed-mode bending test. The results showed that, even at very low values of mixed mode ratio (almost pure mode I loading), intraply damage and the subsequent crack jumping could not be prevented.

Several authors [54, 57, 64, 81, 82] identified different failure mechanisms when testing multidirectional Double Cantilever Beam (DCB) specimens (DCB specimens with different ply orientations adjacent to the interface) for different material systems. Crack jumping [54, 81], double cracking [57] and stair-shape jumping [64, 82] are the most common failure modes recorded. From their results, it can be deduced that using specimens with different stacking sequences may lead to different failure modes or even inhibit these and keep the interlaminar crack propagating in the same plane.

Thermally induced stresses, resulting from the curing process, should be con-
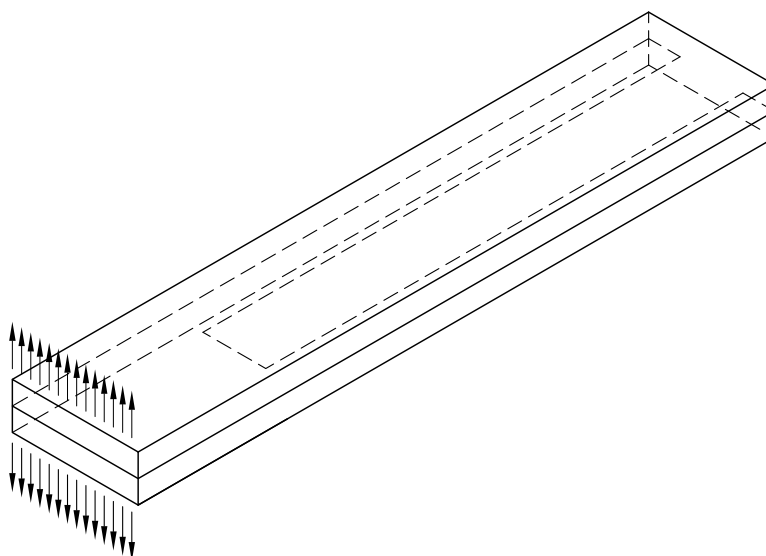
(a) Pre-delaminated edge specimen (after [66])
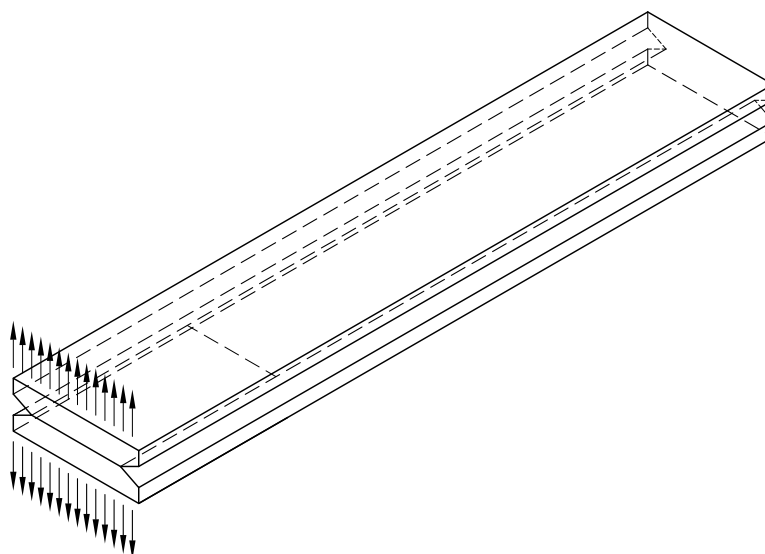
(b) Side-grooved specimen (after [58])

Figure 2.1: Special purpose DCB specimens to avoid crack jumping.

sidered in this analysis. They have been studied by different authors such as de Morais et al. [64, 78], who concluded that they can be neglected, with respect to the fracture toughness. Another study from Nairn [83] showed that the mode I

fracture toughness is highly dependent upon the thermal stresses, the angles of the crack face plies, and the crack beam lay-up.

Another issue in the analysis of the propagation of delamination in multidirectional DCB specimens is the symmetry of the crack front (caused by a non-uniform distribution of the energy release rate along the delamination front [52]). It has an influence on the representativeness of the crack length determined visually from one of the specimen edges, which is used for determining the fracture toughness, G_{Ic}. A schematic sketch of the symmetric and asymmetric crack front is illustrated in Figure
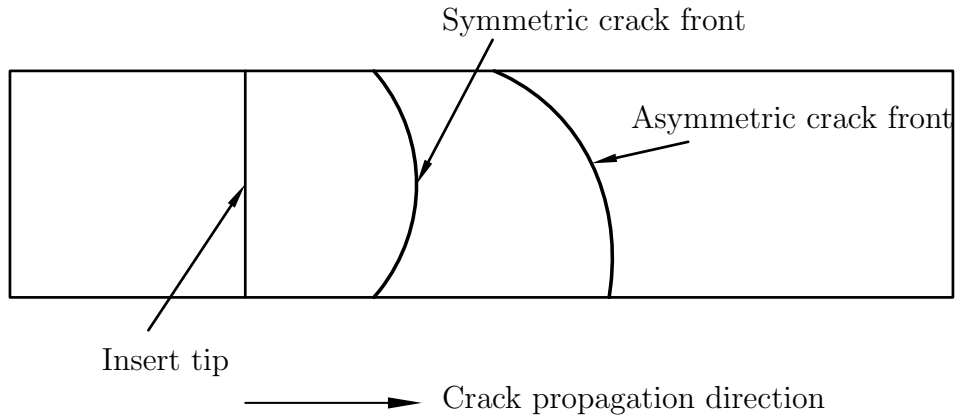
Figure 2.2: Schematic of the symmetric and asymmetric crack front shape.

According to previous works, the uniformity of the energy release rate is favoured by minimizing two elastic parameters, D_c and B_t. The parameter D_c, proposed by Davidson et al. [84], indicates the curvature due to longitudinal/transverse bending coupling. On the other hand, B_t, proposed by Sun and Zheng [85], indicates the skewness of the crack profile due to bending/twisting coupling. According to Prombut et al. [79], the value of D_c should be less than 0.25 and the value of B_t as low as possible. D_c and B_t depend on the bending stiffness matrix coefficients D_{ij} according to:

$$D_c = \frac{D_{12}^2}{D_{11}D_{22}} \tag{2.1}$$

$$B_t = \frac{|D_{16}|}{D_{11}} \tag{2.2}$$

2.3 Stacking Sequences

Five different stacking sequences of AS4/8552 carbon/epoxy composites are analyzed numerically in order to find out the effect of crack arm stiffness on the matrix cracking during interlaminar crack propagation. The material characteristics were measured according to the appropriate ASTM standards and are summarized in Table 2.1 [86].

Table 2.1: Hexcel AS4/8552 properties.

Elastic properties	$E_{11} = 129.0$ GPa; $E_{22} = 7.6$ GPa; $G_{12} = 5.03$ GPa; $\nu_{12} = 0.32$
Strength	$X^T = 2240$ MPa; $Y^T = 26$ MPa; $S^L = 83.78$ MPa
Fracture toughness	$G_{Ic} = 244$ J/m^2; $G_{IIc} = 780$ J/m^2
Nominal ply thickness	$t = 0.125$ mm

The stacking sequences considered during this study and the interface angles, examined using each stacking sequence, are summarized in Table 2.2. The laminates are coded as, for example, S0_8_θ_1_θ_2. The first part of the code is identification of the laminate type, the second represents the number of layers in each of the specimen bending arms and the third and the fourth, θ_1 and θ_2, are the ply orientations of the layers adjacent to the interface. In order to reduce the coupling effect, all the proposed stacking sequences are selected so that the laminates of each beam of the specimen are symmetric and balanced. The previously mentioned stacking sequences are selected to cover the range from very flexible (S0_8) to very stiff (S2_20) arms. The ply orientations θ_1 and θ_2 are varied to obtain different interface angles. The examined interface angles for each stacking sequence are listed in Table 2.3.

Although the main idea behind this investigation is to find out the dependency of the fracture toughness on the orientation of the layers adjacent to the interface, the fracture toughness values of unidirectional laminates, G_{Ic} and G_{IIc} reported in Table 2.1, are used in the simulations for all the interfaces due to the lack of experimental data. It is assumed that this simplification does not have an effect on the qualitative conclusions of this work.

Table 2.2: Selected stacking sequences for fracture examination.

Code	Stacking sequence
S0_8_θ_1_θ_2	$[(\theta_1/-\theta_1/\pm 45)_\mathrm{s}//(\theta_2/-\theta_2/\pm 45)_\mathrm{s}]$
S1_12_θ_1_θ_2	$[(\theta_1/-\theta_1/90/\pm 45/0)_\mathrm{s}//(\theta_2/-\theta_2/90/\pm 45/0)_\mathrm{s}]$
S2_20_θ_1_θ_2	$[(\theta_1/-\theta_1/0_8)_\mathrm{s}//(\theta_2/-\theta_2/0_8)_\mathrm{s}]$
S3_12_θ_1_θ_2	$[(\theta_1/-\theta_1/(0/90)_2)_\mathrm{s}//(\theta_2/-\theta_2/(0/90)_2)_\mathrm{s}]$
S4_12_θ_1_θ_2	$[(\theta_1/-\theta_1/0_4)_\mathrm{s}//(\theta_2/-\theta_2/0_4)_\mathrm{s}]$

Table 2.3: Orientations tested with different configuration.

θ_1°	45	0	15	30	0	0	90	30	15	60
θ_2°	-45	30	-75	60	90	45	30	-30	-45	-60
S0_8	X	X								
S1_12	X	X	X	X	X					
S2_20	X	X	X	X	X	X	X	X	X	X
S3_12	X									
S4_12	X									

2.4   FE Simulations

A numerical model to simulate a multidirectional DCB test should take into account the evolution of interlaminar damage (delamination) as well as that of the intraplay damage to capture the coupling between them. That was the aim of de Morais et al. [54] and Shokrieh and Attar [87] using the Visual Crack Closure Technique VCCT, or that of Wisnom [88] using cohesive zone models for both delamination and intraply damage. These approaches are computationally expensive and, therefore, usually restricted to the analysis of short series or to 2D problems. The procedure proposed in this work, however, does not aim to simulate the evolution of damage during the test. It tries to foresee if, during a delamination test, the crack is likely to jump to another interface or not. Therefore, the simulation consists on propagating the delamination while, at every moment of loading, a failure index for matrix cracking is evaluated (LaRC04 criteria [71]). This failure index is just an indication of damage onset. If the failure index is always below one, no matrix cracking (thus, no jumping) is expected for this ply configuration during the test.

However, if it is larger than 1, that specimen is considered as not suitable because crack jumping is likely to occur.

According to the ASTM D5528 standard [89], the DCB test specimen is 125 mm long, 25 mm wide and has a 50 mm long pre-crack . However, through the present numerical study only a section of the specimen, 70 mm in length, is simulated in order to reduce the computation time. As the omitted part of the model is far from the crack front and is not loaded, this strategy does not affect the local stresses on that area. The model is divided in two parts: precracked zone (50 mm), and uncracked zone, in which the cohesive elements are used. The mesh is refined in the crack tip zone, to correctly simulate the propagation of the interlaminar crack with the cohesive elements, and near the specimen edges, Figure 2.3
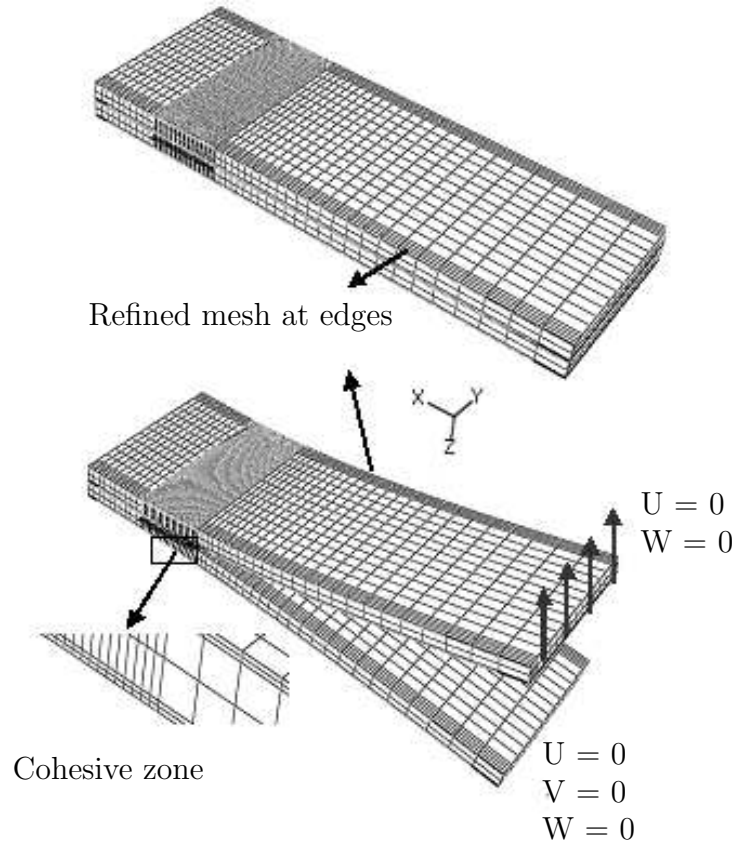
Figure 2.3: FE mesh of the DCB test specimens and boundary conditions.

The model contains 20400 ABAQUS C3D8I eight-node solid elements. The incompatible mode formulation was used to avoid shear locking problems. This el-

ement was chosen after comparing its performance with the one with the reduced integration element C3D8R. Through the thickness, each arm of the specimen has a stack of four surface layers and two groups of embedded layers, all of them symmetrically distributed. The surface layers are modeled using one element per layer. However, in order to reduce the computational time, the groups of embedded plies are modeled using only two plies of solid elements in the thickness direction with only one integration point per layer.

2.5   Cohesive Zone Model

The FE models used include the cohesive zone model developed by Turon et al. [69, 70] (implemented as a user defined element, UEL subroutine). Cohesive zone elements model the interface as a zero thickness layer and have the advantage of encompassing both crack initiation and crack propagation.

The constitutive law used is shown in Figure 2.4. This law is a bilinear relationship between relative displacements and tractions. The first line represents an elastic relationship, prior to damage onset. the onset of damage is related to the interface strength τ^0. When the area under the traction-displacement relation is equal to the fracture toughness, G_c, the interface traction revert to zero and new crack surface is created.
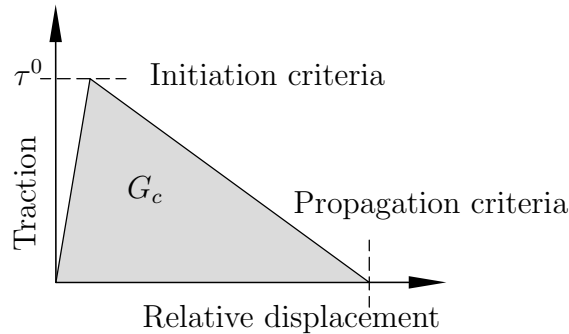
Figure 2.4: Bilinear cohesive law.

The propagation criterion for delamination growth under mixed-mode loading conditions is established in terms of the energy release rates and fracture tough-

nesses. The criterion is based on the work of Benzeggagh and Kenane [90], and was originally defined for a mix of modes I and II as:

$$G_c = G_{Ic} + (G_{IIc} - G_{Ic}) \left(\frac{G_{II}}{G_I + G_{II}} \right)^\eta \qquad (2.3)$$

where G_{Ic} and G_{IIc} are the fracture toughness values in mode I and II, respectively; G_I and G_{II} are the energy release rates in mode I and II, respectively. The η parameter is found by least-square fit of experimental data points of the fracture toughnesses under different mixed-mode ratios.

The propagation criterion can be rewritten as follows:

$$G_c = G_{Ic} + (G_{IIc} - G_{Ic}) \left(\frac{G_{shear}}{G_I + G_{shear}} \right)^\eta \qquad (2.4)$$

where G_{shear} is the shear energy release rate ($G_{shear} = G_{IIc} + G_{IIIc}$) and G_{IIIc} is the critical energy release rate under pure mode III loading. More details and the derivations of each term in Equation 2.4 can be found in [68, 86, 91].

The length of the cohesive zone can be calculated as [70]:

$$l_c = M E_{eq} \frac{G_{Ic}}{\tau^0} \qquad (2.5)$$

where E_{eq} is the equivalent Young's modulus of the material ($E_{eq} = E_3$ [70]), M is a parameter that depends on each cohesive zone model.

During simulations, the values of the transverse tensile and longitudinal shear strengths (Y^T and S^L) are used as the interface strengths in both tensile and shear modes, respectively. Also, the element length is selected in order to discretize the cohesive length with at least three elements [70].

2.6 Failure Criteria

Crack jumping from the initial plane to any other ply interface requires that the crack propagates as a matrix crack through the plies placed in between. The failure mode most likely to occur in this situation is tensile matrix cracking. Therefore, the LaRC04 in-plane tensile matrix cracking failure criterion [71] is considered as indication of crack jumping. The criterion is based on physical models and takes

into consideration non-linear shear behavior and includes the in-situ strength effects. The criterion for matrix cracking failure is [71]:

$$FI_{MT} = (1 - g)\left(\frac{\sigma_{22}}{Y_{is}^T}\right) + g\left(\frac{\sigma_{22}}{Y_{is}^T}\right)^2 + \frac{\frac{\sigma_{12}^2}{G_{12}} + \frac{3}{2}\beta\sigma_{12}^4}{\frac{S_{is}^{L\,2}}{G_{12}} + \frac{3}{2}\beta S_{is}^{L\,4}} \qquad (2.6)$$

where FI_{MT} is the matrix cracking failure index under tensile loading, β is the non-linearity of shear stress shear strain relation parameter, g is the fracture toughness ratio, $g = \dfrac{G_{Ic}}{G_{IIc}}$, and Y_{is}^T and S_{is}^L are the in situ tensile and shear strengths, respectively. The in situ strengths are calculated using the model presented by Camanho et al. [92]. The model was derived by considering a non-linear shear behavior and neglecting the adjoining plies. Taking into consideration that the crack jumping is mainly caused by edge effects [52], the in situ shear and tensile strengths for the thin outer plies are, respectively:

$$S_{is}^L = \sqrt{\frac{(1 + \beta\phi G_{12}^2)^{0.5} - 1}{3\beta G_{12}}} \qquad (2.7)$$

$$Y_{is}^T = 1.79\sqrt{\frac{G_{IIc}}{\pi t \Lambda_{22}^0}} \qquad (2.8)$$

where

$$\phi = \frac{24 G_{Ic}}{\pi t} \qquad (2.9)$$

and

$$\Lambda_{22}^0 = 2\left(\frac{1}{E_{22}} + \frac{\nu_{21}^2}{E_{11}}\right) \qquad (2.10)$$

The LaRC04 criterion is implemented in ABAQUS as a user defined output variable through the UVARM standard subroutine.

2.7   Crack Front symmetry

The shape of the crack front depends on the interface angles and on the laminate stacking sequence and can be directly obtained from the simulations by means of

the study of the distribution of the out-of-plane stress (Figure 2.5 shows some representative cases). The maximum out-of-plane stress follows the crack front geometry and it is just ahead of it. Although this method can give a complete view of the crack front during propagation, an "out of symmetry (OOS)" parameter has been defined to allow for quantitative comparison and discussion. It is defined according to the following procedure:

(i) The crack opening, just behind the crack front, is measured and normalized with respect to its maximum value, (CO) (Figure 2.6),

(ii) A symmetry line is drawn at the specimen mid-width,

(iii) The absolute value of the difference in the crack opening between each pair of equidistant nodes (at the same distance from the symmetry line) is addressed as the out of symmetry (OOS) coefficient.
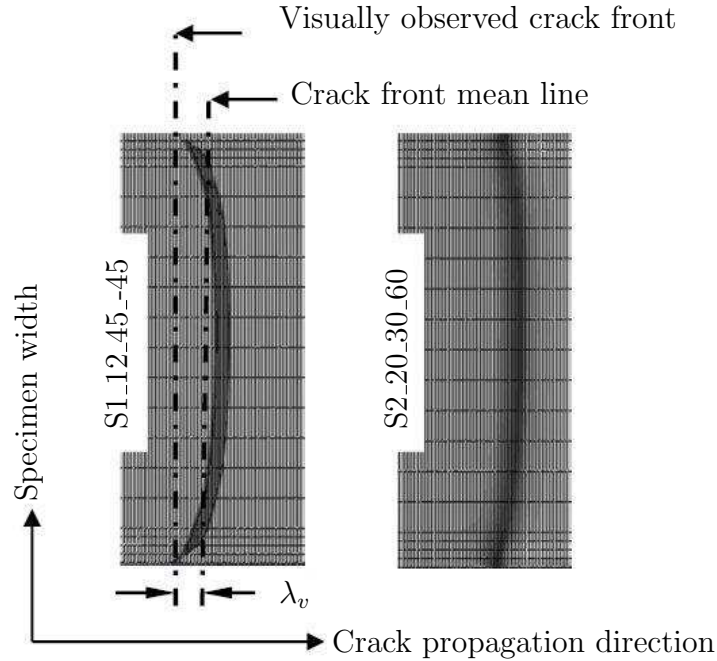
Figure 2.5: Samples of crack front shapes.

This process is repeated for all node pairs and the highest value is considered as the out of symmetry coefficient of the specimen:
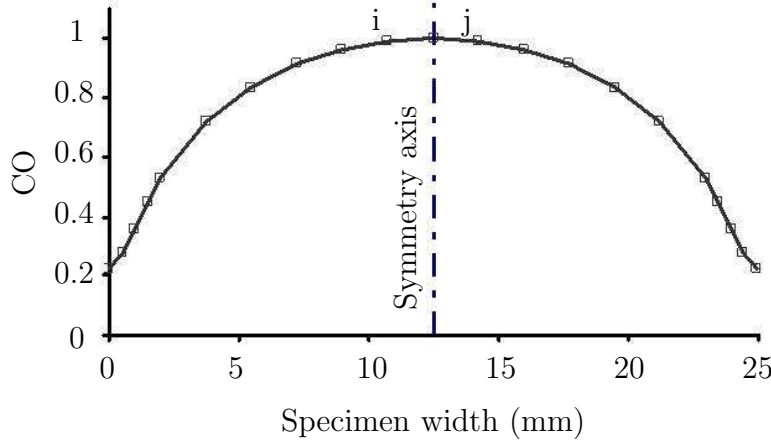
Figure 2.6: Example of normalized crack opening displacement through the specimen width (specimen S2_20_45_-45).

$$OOS = \max\left(CO_i - CO_j\right) \tag{2.11}$$

When measuring the fracture toughness, the crack length is measured at the specimen edge and the crack front is considered as a straight line. This assumption may not be true, especially for multidirectional specimens, because of the elastic bending-twisting and bending-bending couplings that may cause highly curved thumbnail shaped delamination fronts [78, 93]. A term describing the relative position of the crack using its position at the specimen edge and at the crack front mean line, Figure 2.5, is defined as the visual deviation (λ_v) and is compared for the different specimen configurations.

2.8   Results and Discussions

2.8.1   Effect of thermal stresses

In order to investigate the effect of the residual thermal stresses on the matrix cracking failure index, and thus crack jumping, four specimens (S1_12_0_90, S1_12_45_-45, S2_20_30_-30 and S2_20_15_-45) are simulated with and without including a thermal step in the simulation (Figure 2.7 shows the load-displacement curves for the specimen S2_20_30_-30). With the aim of having a conservative view

of the effect of residual stresses, a thermal step from the curing temperature (180°C) to room temperature has been considered (a more realistic step would be defined if the high temperature corresponded to the glass transition temperature of the matrix). The two load curves match within 1%, which agrees well with the conclusion drawn by de Morais et al. [64, 78] (considering the induce thermal stresses does not affect the load-displacement behavior).
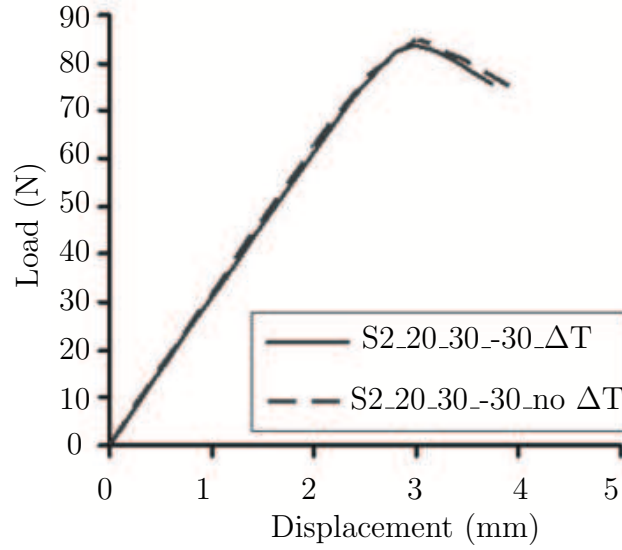
Figure 2.7: Load displacement curves for the S2_20_30_-30 specimen with and without the effect of the thermal residual stresses.

In spite of the fact that load-displacement curves (and the fracture toughness resulting from its data reduction) are not significantly sensitive to thermal stresses, the matrix cracking failure index (FI_{MT}), varies notably when the thermal step is taken into account. The failure index of the specimen S1_12_0_90 exceeds the unity, either with or without the thermal step, before crack propagation. Therefore, this specimen is excluded for any further analysis. For the other three stacking sequences, the simulations accounting for the thermal step result in about 50% higher failure index values, as shown in Table 2.4.

Consequently, the thermal stresses originated during manufacturing do have an effect on the probability of crack jumping and they cannot be neglected in the simulations. A thermal loading step prior to the application of the mechanical load is used in the simulations presented in the remaining of this work.

Table 2.4: Maximum predicted matrix tensile failure index at the three selected specimens, considering or not the residual thermal stresses.

	FI_{MT}	
Stacking sequence	With Δ T	Without Δ T
S1_12_45_-45	0.98	0.55
S2_20_30_-30	0.48	0.24
S2_20_15_-45	0.79	0.40

2.8.2   Matrix cracking

Figure 2.8 shows the matrix cracking failure index of the 45/-45 interface using different arm stacking sequences. The matrix failure index of the DCB specimens for 45/-45 interface can be reduced by about 50% by increasing the bending stiffness of the specimen, which agrees well with the idea proposed by de Morais et al. [54]. The value of the failure index for the S0_8 specimen is not included in the figure because it exceeds 1.0.
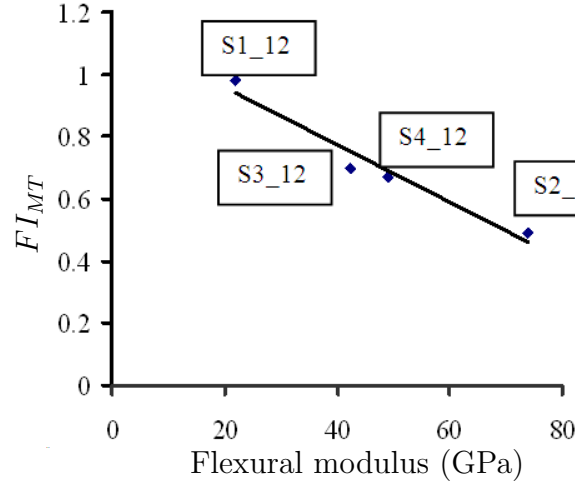
Figure 2.8: Failure index as a function of the bending stiffness of the specimen for 45/-45 interface.

In total, ten interface configurations are selected and their results compared, as summarized in Figure 2.9. In the figure, only two stacking sequences, S1 and S2, are included for simplicity.

It can be seen that the same response is found for these interface configurations,
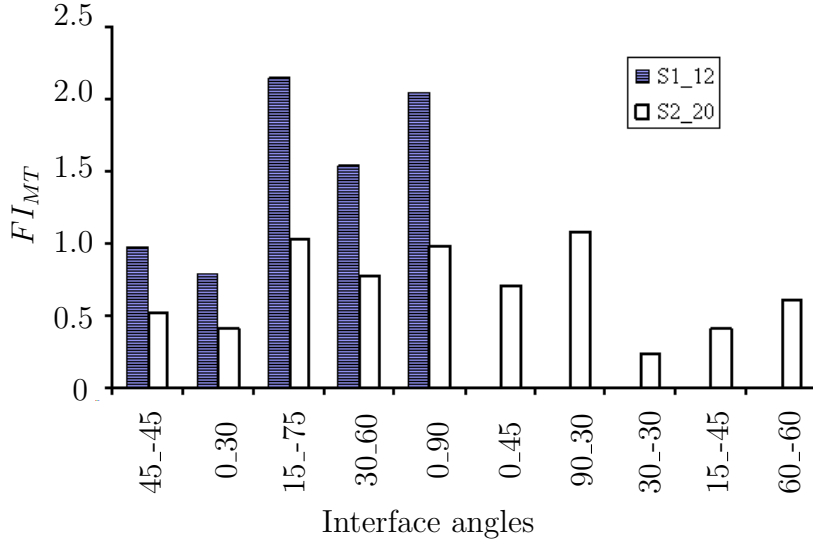
Figure 2.9: Failure index as a function of the interface angles and stacking sequence.

i.e. the higher the stiffness of the specimen (S2_20) the lower the value of the failure index. Therefore, it can be concluded that this stacking sequence is suitable to avoid crack jumping in multidirectional DCB tests.

A qualitative explanation for the reduction of the failure index by increasing the beam stiffness is that the radius of curvature of the arms increases with the stiffness. Therefore, the compliant off-axis plies, which correspond to the outer plies of the specimen arm, achieve a lower level of stress (thus lower failure index) in the case of a stiff specimen than in a more flexible one.

2.8.3   Crack front symmetry

According to different authors [78, 85], a symmetric crack front can be obtained by reducing the value of B_t as much as possible. As described by Prombut et al. [79], the DCB specimen can be divided into three parts; the base laminate (B), the upper arm (U) and the lower arm (L). All these fragments should follow the previous rule to achieve a symmetric crack front. Table 2.5 summarizes the values B_t for our test matrix. The crack front is assessed for only the specimens with failure index lower than one.

As a general trend, the out of symmetry coefficient, OOS, is lower for the base laminate (B) and the value of B_t for the B, U and L parts decrease with the laminate

Table 2.5: The out of symmetry (OOS) coefficient as a function of the ratio B_t.

Stacking sequence	B_t			OOS	λ_v
	B	U	L	%	mm
S1_12_45_-45	0.009	0.016	0.070	6.0	2.29
S2_20_45_-45	0.000	0.019	0.019	0.0	1.83
S3_12_45_-45	0.000	0.076	0.076	0.0	1.94
S4_12_45_-45	0.000	0.064	0.064	0.0	1.94
S1_12_0_30	0.010	0.017	0.120	24.0	2.1
S2_20_0_30	0.007	0.000	0.020	8.0	1.9
S2_20_30_60	0.003	0.020	0.010	14.0	1.37
S2_20_0_90	0.000	0.000	0.000	5.0	1.54
S2_20_0_45	0.002	0.000	0.019	4.0	1.39
S2_20_30_-30	0.000	0.020	0.020	20.0	2.46
S2_20_15_-45	0.000	0.012	0.019	2.0	1.47
S2_20_60_-60	0.000	0.010	0.010	0.0	1.18

stiffness (table 2.5). There is not a direct correlation between OOS and B_t, as illustrated by the specimen with 0/30 interface: the out of symmetry coefficient is maximum whereas the values of B_t are not the highest for the U part of the specimen. This result means that the symmetry of crack front is not affected by the B_t value only.

It is found that the lowest values of the OOS coefficient are obtained when measuring the fracture toughness between $\theta/-\theta$ and $0/\theta$ using the higher stiffness specimen configuration, S2_20.

With respect to the visual deviation (λ_v), the results show that there is no clear dependency on the bending stiffness, the mismatch angle or the incline angle, Table 2.5. The deviation ranges from 1.18 mm to 2.46 mm. Since this range is small, a common average value can be added to the measured crack length, during the propagation tests as a correction for the crack front shape.

2.9   Conclusions

A set of multidirectional specimens has been investigated by means of the Finite Element Method to evaluate the probability of crack jumping during DCB tests.

The simulations performed using a cohesive zone model to simulate the onset and growth of the delamination and included a thermal step previous to the mechanical loading to account for thermal residual stresses. The following conclusions can be drawn from the analysis:

- The induced thermal stresses during the manufacturing process do not affect the expected load versus displacement curves. However, these thermal effects modify the prediction of the tensile matrix cracking failure index and tend to promote migration of the interlaminar crack plane.

- The higher the bending stiffness of the specimen arms, the lower the failure index is and, as a consequence, the lower the tendency to crack jumping is. The stacking sequence S2_20_θ_1_θ_2 ($[(\pm\theta_1/0_8)_s//(\pm\theta_2/0_8)_s]$) can be used to avoid the crack jumping problem for all the examined interfaces.

Although these results are drawn from numerical analysis and the inherent variability due to manufacturing and testing is not taken into account, clear trends of the crack jumping phenomenon and crack front symmetry in delamination tests with different ply interfaces have been obtained. These clear trends are the main motivation to conduct experimental tests about delamination in multidirectional laminates, Chapter 3.

Chapter 3

Delamination Tests

3.1 Overview

In Chapter 2, a numerical study was performed on the crack jumping phenomenon in multidirectional laminates. The matrix cracking failure index, calculated based on the LaRC04 failure criteria [71], was considered as an indicator of crack jumping i.e. the higher the matrix cracking failure index the higher the tendency to crack jumping. Twenty configurations with different flexibilities and interface angles were checked. It was found that crack jumping could be avoided by increasing the bending stiffness of the crack beam arms. This conclusion matched well with the proposal of de Morais et al. [54].

The current chapter corresponds to the experimental validation of the specimen design presented in Chapter 2. Six multidirectional configurations were checked for crack jumping under mode I loading. The examined configurations cover the interface angles 0//30, 30//-30, 45//-45 and 15//-75. Mode I delamination tests were performed in the ambient conditions according to the ISO 15024 test standard [72]. The crack propagation process was monitored using a traveling microscope. To obtain the fracture toughness, the Modified Compliance Calibration (MCC) data reduction scheme was used only for those specimens where the crack propagation had been purely interlaminar (with no crack jumping). In some cases, due to the high amount of fiber bridging, it was impossible to recognize if there was crack jumping or not, based on the traveling microscope images. Consequently, parts of the specimen were cut within the propagation areas and the edges of these parts

were checked using an optical microscope.

3.2   Experiments

3.2.1   Material and specimen configurations

The material used in this work was carbon / epoxy (Hexcel AS4/8552). The properties of the unidirectional AS4/8552 are listed in Table 2.1.

Table 3.1 summarizes the tested stacking sequences and their specifications (NL refers to the number of layers, θ_1 and θ_2 are the orientations of the two layers at the delamination plane and FI_{MT} is the matrix cracking failure index predicted numerically). According to the numerical simulations, the first four configurations are not expected to show crack jumping while this phenomenon is expected to occur in the last one. The fifth configuration is in the transition region, according to the numerical analysis but, crack jumping is expected to occur during the test.

Table 3.1: Configuration of the tested specimens and their characteristics (// indicates the delamination interface).

Laminate	Stacking Sequence	NL	$\theta_1//\theta_2$	FI_{MT}
S2_20_30_-30	$[(30/-30/0_8)_{\mathrm{s}}//(-30/30/0_8)_{\mathrm{s}}]$	40	30//-30	0.2
S2_20_0_30	$[0_{20}//(30/-30/0_8)_{\mathrm{s}}]$	40	0//30	0.5
S2_20_45_-45	$[(45/-45/0_8)_{\mathrm{s}}//(-45/45/0_8)_{\mathrm{s}}]$	40	45//-45	0.5
S4_12_45_-45	$[(45/-45/0_4)_{\mathrm{s}}//(-45/45/0_4)_{\mathrm{s}}]$	24	45//-45	0.7
S1_12_45_-45	$[(45/-45/90/\pm45/0)_{\mathrm{s}}//$			
	$(-45/45/90/\pm45/0)_{\mathrm{s}}]$	24	45//-45	1.0
S1_12_15_-75	$[(15/-15/90/\pm45/0)_{\mathrm{s}}//$			
	$(-75/75/90/\pm45/0)_{\mathrm{s}}]$	24	15//-75	2.5

It is worth remarking that the configurations S2_20_30_-30, S2_20_45_-45, S4_12_45_-45 and S1_12_45_-45 are standard DCB specimens in which the two crack arms have the same stiffness. The other two configurations (S2_20_0_30 and S1_12_15_-75) present a small difference in the bending stiffness between the two arms resulting in Asymmetric Double Cantilever Beam (ADCB) specimens. Consequently, some mode II contribution might be expected during the propagation of the interlaminar crack due to the unsymmetrical displacement fields of both arms [94, 95]. However,

the contribution of the G_{II} was checked numerically using the Virtual Crack Closure Technique (VCCT) and the results showed that it is less than 4%.

3.2.2 Delamination tests

The specimens used were 175 mm long and 25 mm wide, compliant with the ISO 15024 standard [72]. The thickness of the specimens varied depending on the configuration (see Table 3.1). The Side Clamped Beam (SCB) hinge clamping system, developed by Renart et al. [96] (see Figure 3.1), was used to load the specimen. Five test specimens were tested per configuration.

(a) SCB hinge mounted on a specimen   (b) Components of the hinge set
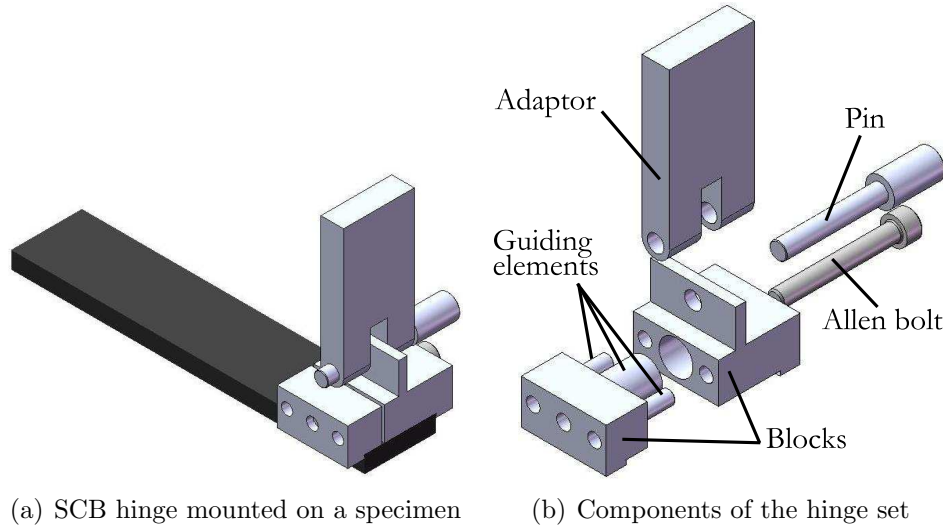
Figure 3.1: Schematic of the DCB test specimen and the SCB hinge clamp (after [96]).

During the propagation process, the crack front was observed and the propagation process was recorded using an optical system composed of a high-resolution video camera (*JVC TK-1270*) and a long distance microscope (*Questar QM 100 MK III*).

For a better understanding of the fracture process, a 25 x 10 mm part of the specimen was cut, for each configuration, and its edge was observed using an optical microscope to inspect the path followed by the crack during propagation. After being cut, with the precautions summarized by Greenhalgh [56] (slow cutting rate, dry cutting, etc.), the specimen was molded in a silicon mold and merged with an

epoxy resin of the same properties as the specimen itself to facilitate the polishing. The mold was left over-night and then polished. A fluorescence optical microscope (*Leica, DMR-XA*) was used to observe the specimen edge.

3.2.3   Data reduction procedure

The standard data reduction schemes, developed for unidirectional laminates, are usually used in multidirectional ones [79, 97, 98] as well. Gong et al. [99] presented a comparison between the different data reduction schemes. Their work showed that using any of the reduction schemes lead to almost the same result in multidirectional specimens except for the simple beam theory. For the current work the Modified Compliance Calibration (MCC) reduction scheme, [72, 96], was used to calculate the energy release rate, G_{Ic}, as:

$$G_{Ic} = \frac{3m}{4h} \left(\frac{P}{b} \right)^2 \left(\frac{bC}{N} \right)^{2/3} \tag{3.1}$$

where h is the thickness of one arm, b is the specimen width, P is the applied load, C is the load line compliance, m is the slope of $\left(\frac{bC}{N} \right)^{1/3}$ vs. the delamination length normalized by the specimen thickness $(a/2h)$ and N is the load block correction factor, [100]. It is worth remarking that the contribution of N is very limited [101].

With respect to the two ADCB specimens, the global and the local partitioning data reduction schemes [102] could be used. But, as mentioned before, the mode II contribution was below 4% and, consequently, this contribution was neglected and Eq. (3.1) was used.

3.3   Results and Discussion

3.3.1   Crack propagation

Figure 3.2 shows examples of the obtained crack propagation modes: smooth propagation, stair-shape propagation, crack jumping and double cracking. For some configurations only one type of propagation mode is found, while for others different propagation modes were observed for different specimens. The number of specimens corresponding to each propagation mode for each configuration is summarized in

Table 3.2. The modes included in Table 3.2 correspond to the first detected propagation mode. In most of the cases, where crack jumping is observed, it occurs when extending the initial crack from the insert (during the precracking).

(a) Smooth propagation

(b) Stair-shape propagation

(c) Crack jumping

(d) Double cracking
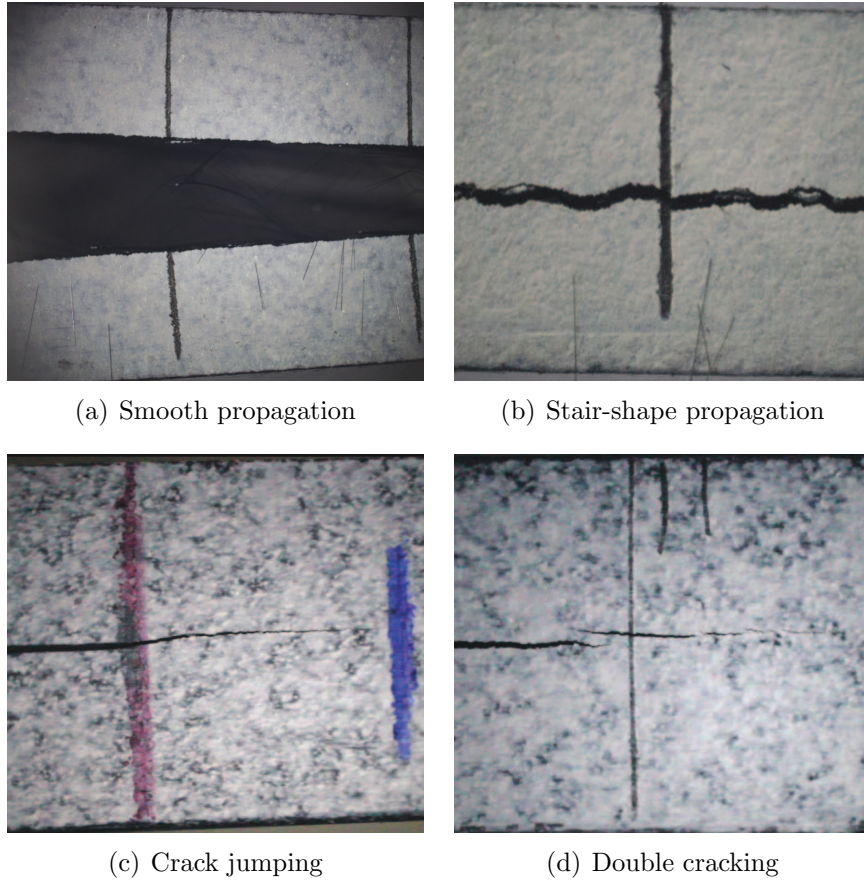
Figure 3.2: Different delamination propagation modes in multidirectional laminates under mode I loading.

As mentioned earlier, five test specimens are tested for each configuration. In general, the lower the value of the matrix cracking failure index, Table 3.1, the higher the number of valid specimens (specimens at which the crack advances in smooth propagation mode), Table 3.2. However the configuration S2_20_0_30 is an exception to this trend. For this configuration, the crack either jumps to the 30°/-30° interface in two specimens, or in one case a second crack initiates at this interface spontaneously creating the phenomenon of double cracking. It should be noted that, due to its high ply mismatch angle (60°), the 30°/-30° interface develops

Table 3.2: Number of specimens corresponding to each failure mode.

	Failure mode			
Configuration	Smooth propagation	Stair-shape	Jumping	Double cracking
S2_20_30_-30	5	—	—	—
S2_20_0_30	2	—	2	1
S2_20_45_-45	5	—	—	—
S4_12_45_-45	3	1	—	1
S1_12_45_-45	2	3	—	—
S1_12_15_-75	—	—	5	—

considerable interlaminar shear stresses as the arm bends, hence its propensity to delaminate even without a triggering intraply matrix crack. A reasonable way to avoid this double cracking is to optimize the beam stacking sequence to have the maximum mismatch angle at the desired delamination plane.

Some images of the crack propagation path on the edge of the specimen obtained by composing different specimen micrographs can be observed in Figure 3.3. As shown in the figure, the use of the optical microscope can reveal interesting details of the crack propagation in multidirectional laminates. The first and the second images, Figure 3.3(a) and Figure 3.3(b), show examples of the smooth crack propagation in the original interface surface. Figure 3.3(c) shows the resulting crack profile when crack jumping occurs. It can be observed how the crack has changed its propagation plane several times involving transverse matrix cracking. Figure 3.3(d) shows one specimen where the crack is branched into many cracks surrounding the resin rich area.

Figure 3.4 shows a more detailed view of one specimen where crack jumping is not observed. The three images are taken at different positions along the crack. The first image, Figure 3.4(a), corresponds to the well-known delamination phenomenon. The second, Figure 3.4(b), corresponds to the propagation of the crack near to the middle of one layer. The third image, Figure 3.4(c), shows crack propagation in one of the two plies surrounding the insert plane, but close to the interface. According to the ASTM D 5573 [103], this mechanism can be identified as light fiber tearing. As a general trend for all the configurations, the delamination starts by pure interlaminar fracture, Figure 3.4(a) and after that, either of the three mechanisms can appear.
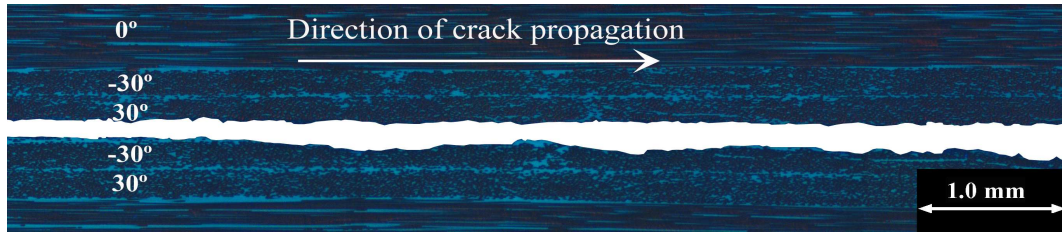
(a) Specimen S2_20_30_-30, 20 mm away from the inset tip
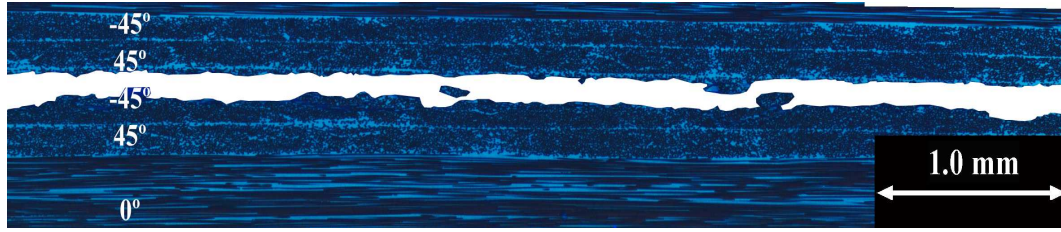
(b) S4_12_45_-45, 5 mm away from the insert tip
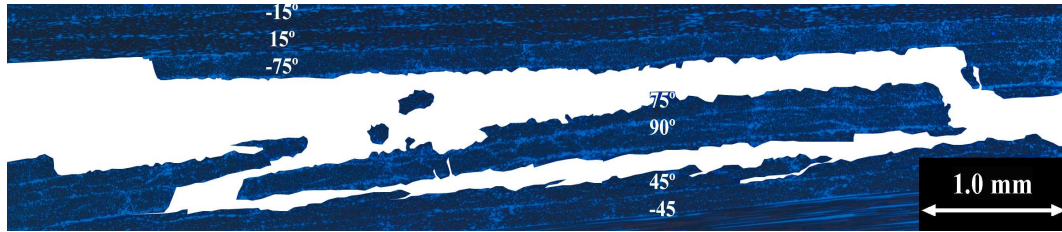
(c) S1_12_15_-75, at the insert tip
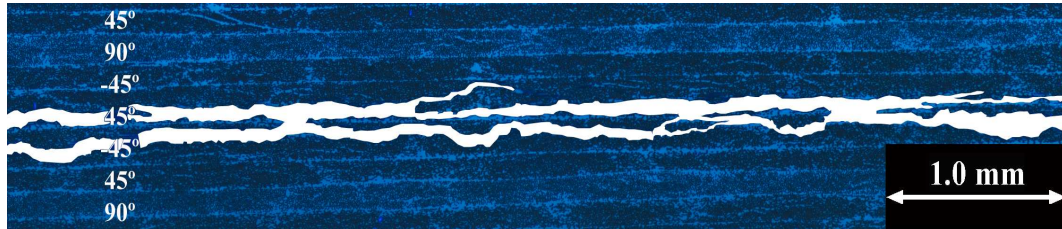
(d) S1_12_45_-45, 20 mm away from the insert tip

Figure 3.3: Propagation mode in multidirectional laminates.

The most common failure mechanism is the light fiber tearing.

3.3.2 Fracture toughness data

Figure 3.5 shows a comparison of the crack resistance curves (R-curves) obtained through the crack propagation of the unidirectional laminate and the multidirectional ones. The R-curve of the configuration S1_12_15_-75 is not included in the

(a) Interlaminar

(b) Intralaminar

(c) Light fiber tearing
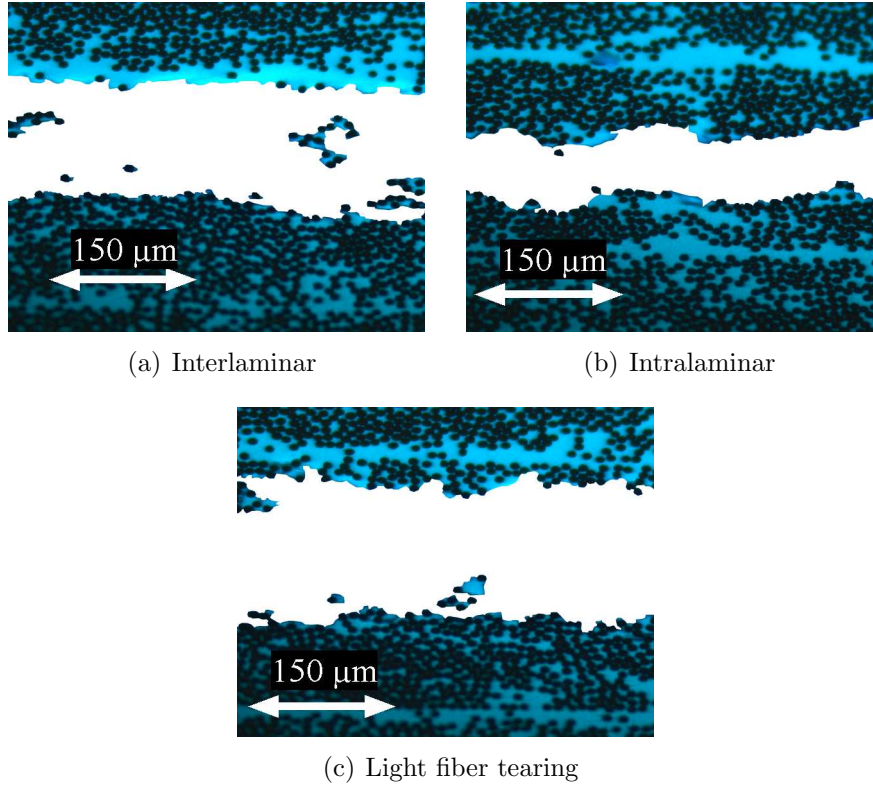
Figure 3.4: Delamination mechanisms for S4_12_45_-45.

comparison because crack jumping is observed at all the specimens of this configuration. None of the specimens shown in Figure 3.5 suffers from crack jumping or double cracking. The R-curve of the unidirectional specimen is almost constant whereas, for the multidirectional ones, due to fiber bridging, several peaks and valleys are recognized through propagation.

Table 3.3 summarizes the initiation and propagation fracture toughness values, and the corresponding Coefficient of Variation (CV), for each configuration. Only the specimens that did not show crack jumping or double cracking, Table 3.2, are considered in the calculations. For the configuration S1_12_15_-75, neither the onset nor the propagation fracture toughness values are calculated because crack jumping is observed for all the specimens of this configuration. Considering that the crack usually initiates near the specimen mid-width, the nonlinear (NL) point is the most meaningful when measuring the fracture toughness for the crack onset [99]. The nonlinear points for different configurations are listed in Table 3.3.
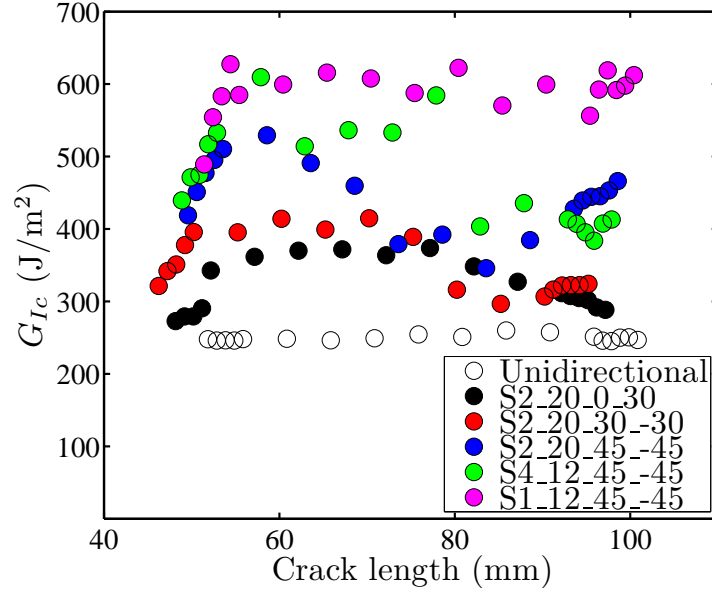
Figure 3.5: Delamination-resistance curve for the unidirectional and the multidirectional configurations.

Table 3.3: Experimentally measured onset and propagation values of fracture toughness.

| Configuration | G_{Ic} | | | |
| | Onset (NL point) | | Propagation | |
	Mean J/m^2	CV %	Mean J/m^2	CV %
S2_20_30_-30	195.7	10.1	341.4	3.45
S2_20_0_30	194.3	0.2	315.7	2.6
S2_20_45_-45	203.8	8.1	405.3	8.0
S4_12_45_-45	185.9	2.7	490.6	9.3
S1_12_45_-45	205.0	8.1	593.5	0.9
S1_12_15_-75	—		—	

The onset fracture toughness is similar for all the configurations and interface angles with a coefficient of variation of less than 5%. This result is reasonable because, at the insert tip, the effect of the interface angles is insignificant due to the existence of a resin rich area in front of the insert tip. Moreover, fiber bridging does not affect the onset process and, at the initiation point, the crack front is straight and perpendicular to the crack front advance direction (hence, the crack front shape

effect also vanishes).

With respect to the propagation fracture toughness data, it can be noticed that the toughness of the multidirectional interfaces is higher than that of the unidirectional ones (see Table 2.1 and Table 3.3). The same result was found by other researchers [104, 105]. The interface 0°//30° has the lower value of toughness while the interface 45°//-45° yields the maximum value of the fracture toughness when tested with high flexible beam arms.

For specimens with 45°//-45° interface, it is noticed that the toughness value is a function of thestacking sequence specimen. Shokrieh and Heidari-Rarani [106] recorded a similar deviation in the fracture toughness measured for 0°//0° interface using different stacking sequences in the beam arms. The higher the flexibility of the beam arms the higher is the apparent toughness of the interface.

The reason behind this response is the amount of fiber bridging. Different amounts of fiber bridging are recognized, for different configurations, during propagation. A qualitative comparison between the amount of fiber bridging for the interface 45°//-45° with different stacking sequence is made in Figure 3.6. It is clear that the higher the flexibility of the arms, the higher the amount of fiber bridging for the same ply interface. This fact justifies the difference in the measured fracture toughness for the three different specimen configurations with 45°//-45° interface reported in Table 3.3. This is in agreement with the results found in [107–109]. The reason behind the higher amount of fiber bridging in flexible specimen may be related to the higher bending that these specimens suffer from, compared to the stiffer ones. This bending causes some fiber matrix debonding, which can be observed as fiber bridging.

The comparison between the propagation toughness data of the configurations S2_20_45_-45, S4_12_45_-45 and S1_12_45_-45 shows that the effect of fiber bridging on the fracture toughness for the same interface angle is 47%. On the other hand, the comparison between the data of the configurations S2_20_30_-30, S2_20_0_30 and S2_20_45_-45 shows that the effect of the interface angle is 29%, at almost the same bending stiffness. This indicates that the fiber bridging effect is stronger than the mismatch angle effect.

In Section 3.3.1, it has been demonstrated that crack propagation occurs mostly between a composite layer and a resin rich area or inside one layer close to the

(a) S2_20_45_-45

(b) S4_12_45_-45

(c) S1_12_45_-45
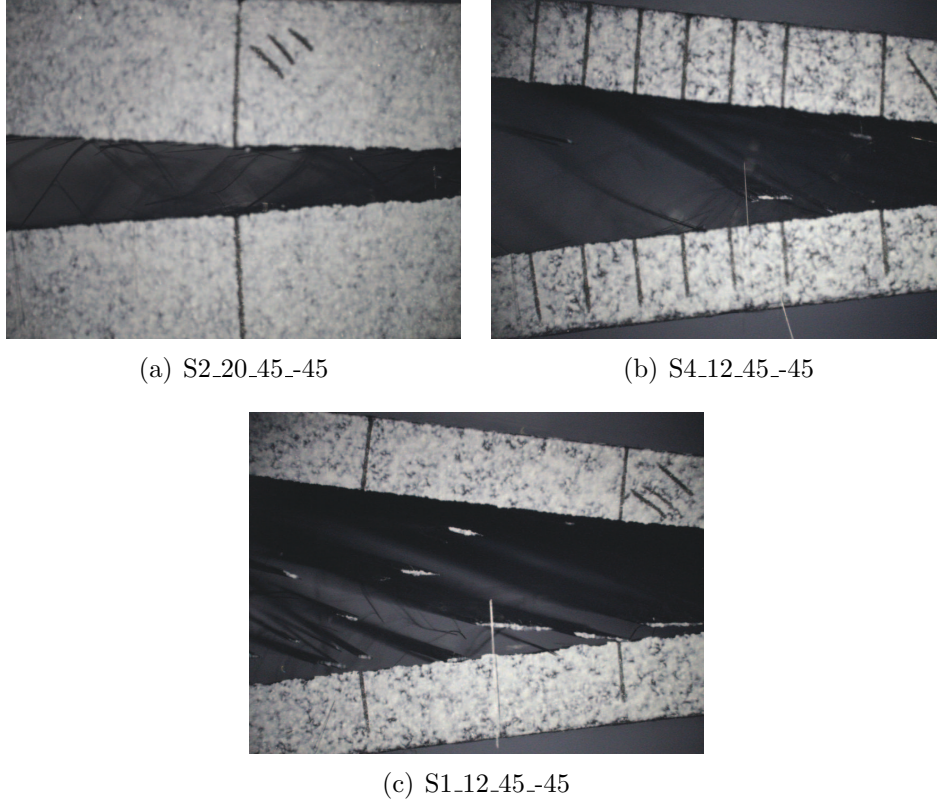
Figure 3.6: Fiber bridging for interface 45°//-45° observed using different stacking sequences.

interface (light fibre tearing mode). The fact that the crack propagates inside a layer and not at the interface between two layers might indicate that the measured fracture toughness depends more on the angle between the crack growth direction and the ply orientation in which the crack propagates, than on the mismatch angles of the plies adjacent to the interface. In fact, when comparing two cases in which the crack propagated inside the 30° layer (S2_20_30_-30 and S2_20_0_30) the measured difference in fracture toughness is only 9%. And these values differ up to 30% from that of the batch S2_20_45_-45, where the crack propagates inside the 45° layer. However, further investigation should be carried out to support this idea.

From a practical point of view, the presented data indicate that the current engineering practice of assuming that the fracture toughness at any interface of a composite structure corresponds to the results of tests in UD plies (0°//0° specimens), underestimates those values. Moreover, nowadays it is a common practice

in composites design to analyze the effect of delaminations by using cohesive finite elements based on $0°//0°$ interlaminar fracture toughness values resulting in safe design but inaccurate predictions. A truly optimized design requires taking into account the dependence of the fracture toughness on the interface angle and on the crack orientation with respect to the ply angles.

3.4 Conclusions

Delamination tests in mode I were conducted to validate the numerical study performed in Chapter 2. Six multidirectional configurations were defined by means of numerical design and tested experimentally to check the possibility of controlling the crack jumping phenomenon. After being tested, parts of the specimens were cut and observed using an optical microscope to determine the crack path.

The results indicated that by increasing the flexural stiffness of the crack arms the crack jumping under mode I crack propagation can be highly minimized. However, the results obtained for some cases showed that the effect of the interlaminar shear stresses due to the mismatch angle should be taken into consideration when designing the stacking sequence of the fracture specimens. The fracture toughness values were more affected by fiber bridging than by the mismatch angles between the layers interfacing the crack plane. The measured effect of fiber bridging is 47% whereas the effect of the mismatch angle is 29%. Optical microscope images show that delaminations are not pure interlaminar fractures. Instead, fiber tearing is more common along the crack propagation path. More investigations are required to understand the phenomenon of crack path and its driving factors in multidirectional laminates.

Part II

Optimization of Dispersed Laminates for Improved Damage Resistance and Damage Tolerance

Chapter 4

Stacking Sequence Optimization

4.1 Overview

The work described in the current chapter aims to implement and test an optimization algorithm to select the proper stacking sequence of laminated composite plates subjected to different loading conditions. Moreover, an investigation is conducted on the benefits of using non-conventional dispersed laminates (laminates in which the fibers are straight and orientation angles are not limited to the conventional $0°$, $\pm45°$ and $90°$ orientations) over conventional ones, in terms of stiffness, buckling resistance and strength.

The Ant Colony Optimization algorithm is used with strength constraints to find the best candidate to achieve this goal. The AC algorithm is selected for this purpose due to its capabilities and the results of the comparison studies presented in the literature [110–112]. A study is conducted to select the most suitable failure criterion among three common ones. The fiber orientations are modeled as a discrete variable ranging from -85° to 90° with a 5° jump. To achieve symmetry, only one half of the laminate is designed and the other half is defined by mirroring the stacking sequence. To achieve balance, each layer with a $\theta°$ orientation angle is followed by one of $-\theta°$.

The methodology is used for two loading cases: biaxial compression and biaxial tension. In the case of biaxial compression, the problem is formulated to maximize the critical buckling load whereas with the biaxial tension, the formulation has the objective of minimizing the failure indices.

4.2   Introduction

The ability to tailor stiffness and strength to meet a certain application requirement is directly related to stacking sequence optimization. Ghiasi et al. [28, 73] reviewed the optimization techniques used for laminated composites and the characteristics of each algorithm. In that work, it was concluded that gradient direct optimization methods are not suitable for the problem of optimizing the stacking sequence of composite laminates. The reasons are the discrete nature of the problem variables and the huge number of local optima where the gradient methods can converge without reaching the global optimal [113, 114]. On the other hand, the enumeration technique is suitable only for laminates with small numbers of layers and combinations of possible fiber orientations [112].

Metaheuristic search algorithms are the most suitable to solve the laminate stacking sequence problem in which the objective function can be discontinuous, nondifferentiable, stochastic, or highly nonlinear [115]. Among the metaheuristic methods, Genetic Algorithms (GA) represent the most commonly used technique in the optimization of laminated composites [116–120]. Other metaheuristic techniques were introduced in the literature during the last decade such as the Scatter Search algorithm (SS) [113], Simulated Annealing algorithm (SA) [121], Generalized Pattern algorithm (GP) [115], Fractal Branch and Bound algorithm (FB&B) [122, 123], Tabu Search algorithm (TS) [124] and Particle Swarm algorithm (PS) [125].

The Ant Colony (AC) algorithm is one of the metaheuristic algorithms that was introduced in the early 1990s by Dorigo et al. [126]. The first use of the AC in the optimization of composite laminates was in 2008 by Aymerich and Serra [110]. The comparison between the Ant Colony algorithm and other metaheuristic algorithms was introduced by several authors; Aymerich and Serra [110] compared AC with GA, Bloomfield et al. [112] compared the AC, the PS and the GA and Hudson et al. [111] compared AC, SA and PS algorithms. The results of these studies showed an improved response of the AC algorithm in terms of both the solution quality and the computational costs, as compared to the other algorithms.

The usage of dispersed laminates in stacking sequence optimization studies can be divided into two categories. The first category includes research that modeled the orientation angle as a continuous variable (for example Adali et al. [127]). This

approach may lead to a non-optimal or out of feasible region stacking sequence during the manufacturing. The second category includes studies that modeled the orientation angle as a discrete variable (for example Irisarri et al. [128] and Edral and Sonmez [121]). The current paper adopts the discrete modeling of the orientation angles.

From the aeronautical industry point of view, using dispersed laminates helps to improve the damage resistance but its effect on the damage tolerance is not clear [129]. The damage tolerance is characterized by the buckling capacity of the sublaminates which adds an extra-motivation to the current study.

4.3 In-Plane Biaxial Loading of Laminated Panels

4.3.1 Stiffness and buckling

A composite plate under two loading conditions, biaxial tension and compression (see Figure 4.1), is analyzed in the current chapter. Although failure mechanisms in the two cases are different (buckling or fiber kinking in the compression case; tensile matrix and fiber failure in the tensile case), the stress strain relations for both cases are similar. By considering only the in-plane deformations, the strains in the global coordinate system corresponding to the biaxial loading are calculated as:

$$
\begin{aligned}
\varepsilon_x &= a_{11}\lambda_c N_x + a_{12}\lambda_c N_y \\
\varepsilon_y &= a_{12}\lambda_c N_x + a_{22}\lambda_c N_y
\end{aligned}
\tag{4.1}
$$

where $\lambda_c N_x$ and $\lambda_c N_y$ are the loads in both x and y directions, λ_c is the load multiplier and a_{ij} are the compliance matrix components. At each lamina i with an orientation angle θ^i, the components of local strain vector $\{\varepsilon\}^i$ are:

$$
\begin{aligned}
\varepsilon_{11}^i &= \varepsilon_x \cos^2\theta^i + \varepsilon_y \sin^2\theta^i \\
\varepsilon_{22}^i &= \varepsilon_x \sin^2\theta^i + \varepsilon_y \cos^2\theta^i \\
\gamma_{12}^i &= (\varepsilon_y - \varepsilon_x)\sin^2\theta^i
\end{aligned}
\tag{4.2}
$$

(a) Biaxial compression   (b) Biaxial tensile
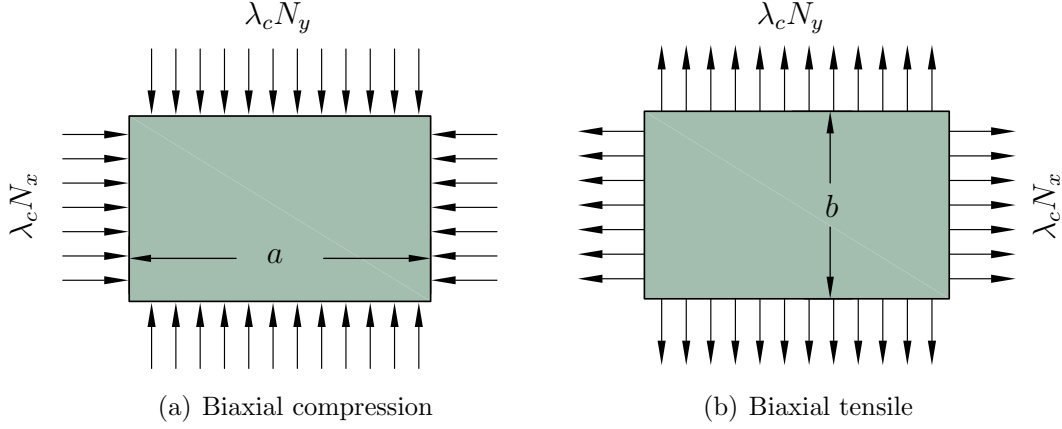
Figure 4.1: Biaxial compression and tensile loading and geometrical conditions.

At the lamina level, the local stress vector $\{\sigma\}^i$ is:

$$\{\sigma\}^i = [Q]\{\varepsilon\}^i \tag{4.3}$$

where $[Q]$ is the in-plane stiffness matrix of the lamina.

With respect to the biaxial compression case, the value of the critical buckling load multiplier λ_c for a laminated panel can be calculated as [114]:

$$\lambda_c(p,q) = \pi^2 \frac{D_{11}\left(\frac{p}{a}\right)^4 + D_{22}\left(\frac{q}{b}\right)^4 + 2\left(D_{12} + D_{66}\right)\left(\frac{p}{a}\right)^2\left(\frac{p}{a}\right)^2}{\left(\frac{p}{a}\right)^2 N_x + \left(\frac{q}{b}\right)^2 N_y} \tag{4.4}$$

where p and q are the number of half waves in both x and y direction, D_{ij} are the bending stiffness matrix coefficients and a and b are the specimen length and width, respectively.

The material used for the current investigation is the AS4/8552 carbon/epoxy. The unidirectional elastic, strength and fracture properties are listed in Table 2.1.

4.3.2 Failure criteria

Amongst more than 40 failure criteria developed for laminated composite materials, the maximum strain criterion is the most commonly used in the optimization of the stacking sequence, and the Tsai-Wu one is the most commonly used in the industry [130]. These two failure criteria are very simple in terms of formulation and

implementation which means a low computational effort. However, these criteria do not consider some of the influencing variables in the failure process of laminated composite i.e. they do not take into account the effect of shear non-linearity, lamina position and thickness (the in situ effect) on the predicted failure index.

During the last few decades, many physically-based failure criteria have been developed to be more suitable for laminated composites. Although this type of failure criteria is proven to achieve trustworthy results, the number of studies that adopt them is still small (for example Lopez et al. [131] and Kober and Kühhorn [132]) due to the required computational effort. The LaRC03 failure criteria [133] fall into this category of physically-based failure criteria and have been selected to conduct the current study. Moreover, the criteria adjust the strength of the ply depending on its relative position in the laminate (the in situ strength phenomenon) and take into account the non-linear in-plane shear deformation behavior.

As summarized in [134],the maximum strain criterion predicts the failure when:

$$FI = \frac{\varepsilon_{ij}}{\varepsilon_{ij}^{all}} \tag{4.5}$$

whereas the Tsai-Wu criterion predicts the failure when:

$$
\begin{aligned}
FI \quad = \quad & \left[\frac{1}{X^T} - \frac{1}{X^C}\right]\sigma_{11} + \left[\frac{1}{Y^T} - \frac{1}{Y^C}\right]\sigma_{22} + \left[\frac{1}{X^T X^C}\right]\sigma_{11}^2 \\
+ \quad & \left[\frac{1}{Y^T Y^C}\right]\sigma_{22}^2 + \left[\frac{1}{(S^L)^2}\right]\sigma_{12}^2 + 2\left[\frac{-1}{2X^T X^C}\right]\sigma_{11}\sigma_{22} \tag{4.6}
\end{aligned}
$$

The LaRC03 failure indices with respect to each failure mechanism [133] are :

(a) Matrix tensile failure ($\sigma_{22} \geq 0$):

$$FI_{MT} = (1-g)\left(\frac{\sigma_{22}}{Y_{is}^T}\right) + g\left(\frac{\sigma_{22}}{Y_{is}^T}\right)^2 + \left(\frac{\sigma_{12}}{S_{is}^L}\right)^2 \tag{4.7}$$

where g is the ratio between the fracture toughness under pure mode I ,G_{Ic}, and the fracture toughness under pure mode II ,G_{IIc}. The values of the in-situ strengths, Y_{is}^T and S_{is}^L can be calculated from Eq. (2.8) and (2.7), respectively.

(b) Matrix compression failure ($\sigma_{22} < 0$):

- If $\sigma_{11} < Y^C$

$$FI_{MC} = \left(\frac{\sigma_{eff}^{mT}}{S^T}\right) + \left(\frac{\sigma_{eff}^{mL}}{S_{is}^L}\right)^2 \tag{4.8}$$

where σ_{eff}^{mT} and σ_{eff}^{mL} are the effective shear stresses in the misalignment frame (the fiber plane when considering initial misalignment angle) and S^T is the transverse shear strength.

- If $\sigma_{11} \geq Y^C$

$$FI_{MC} = \left(\frac{\sigma_{eff}^{T}}{S^T}\right) + \left(\frac{\sigma_{eff}^{L}}{S_{is}^L}\right)^2 \tag{4.9}$$

where σ_{eff}^{L} and σ_{eff}^{T} are the effective shear stresses for matrix compression.

(c) Fiber tension ($\sigma_{11} \geq 0$)

$$FI_{FT} = \left(\frac{\sigma_{11}}{X^T}\right) \tag{4.10}$$

(d) Fiber compression ($\sigma_{11} < 0$)

- If $\sigma_{22}^m < 0$

$$FI_{FC} = \langle\frac{|\sigma_{12}^m| + \eta^L \sigma_{22}^m}{S_{is}^L}\rangle \tag{4.11}$$

- If $\sigma_{22}^m \geq 0$

$$FI_{FC} = (1 - g)\left(\frac{\sigma_{22}^m}{Y_{is}^T}\right) + g\left(\frac{\sigma_{22}^m}{Y_{is}^T}\right)^2 + \left(\frac{\sigma_{12}^m}{S_{is}^L}\right)^2 \tag{4.12}$$

where σ_{22}^m and σ_{12}^m are the stress components in the misalignment frame.

For the detailed definition of each term, reader is refereed to [133].

4.4   Ant Colony Optimization Algorithm

The AC algorithm is a simulation of the behavior of real ants when traveling between the nest and the food source. Assuming that one ant travels several times from home to the food source, it must select a certain path on each journey. The way in which the ant chooses a certain path instead of another is dependant on the relative amount of pheromone concentration on the paths. The shortest paths

to the food source have higher pheromone concentrations because more ants have successfully followed those paths in previous travels [135]. However, the selection in the first iteration is randomly decided.

In our laminate stacking sequence optimization equivalent, each path corresponds to a stacking sequence. In a given optimization iteration (trip) a higher bonus (pheromone concentration),τ_{ij}, is given to the orientations which are part of the best performing stacking sequences. In the following iteration, the probability, P_{ij}^k of ant k, of choosing the ply orientations with higher bonus is superior.

Consider the simple example shown in Figure 4.2. The objective is to design a laminate with $[\theta_1/\theta_2/\theta_3]_s$ with maximum in-plane Young's modulus E_x. Three ants are selected to perform the optimization process. The available orientation angles are 0°, 90°, °45 and -45°. The probability of each ant to select a certain orientation angle is the same in the first iteration (it is represented in the figure by the white color shading each orientation angle in the first iteration).

The first ant (A1) starts to select a certain stacking sequence based on the probability at each orientation angle, and evaluates the objective function. The second and the third ants do the same. Since we are optimizing for the maximum value, the stacking sequence with the higher in-plane modulus is selected as the best solution and the one with the lower in-plane modulus is considered as the worst solution. With respect to the best stacking sequence, the first layer (L1) is oriented at 0°. This 0° is selected by the three ants at this layer. This implies that a higher bonus should be given for this orientation at this layer. The second and the third layers, of the best configuration, are oriented at -45° and 0°.

At the end of the first iteration the pheromone matrix should be updated to be used in the next iteration. It can be seen in the figure that the orientation 0° at the first layer has the higher pheromone concentration followed by the -45° and 0° at the second layer and the third layer, respectively. The rest of the pheromone matrix components remain the same as in the first iteration. The process is iteratively repeated until the optimum is reached.

The detailed algorithm is described by Rao [136], and its adaptations to the present problem can be summarized in the following procedure:

Step 1:

- Define the number of ants (NA), the number of available orientation angles
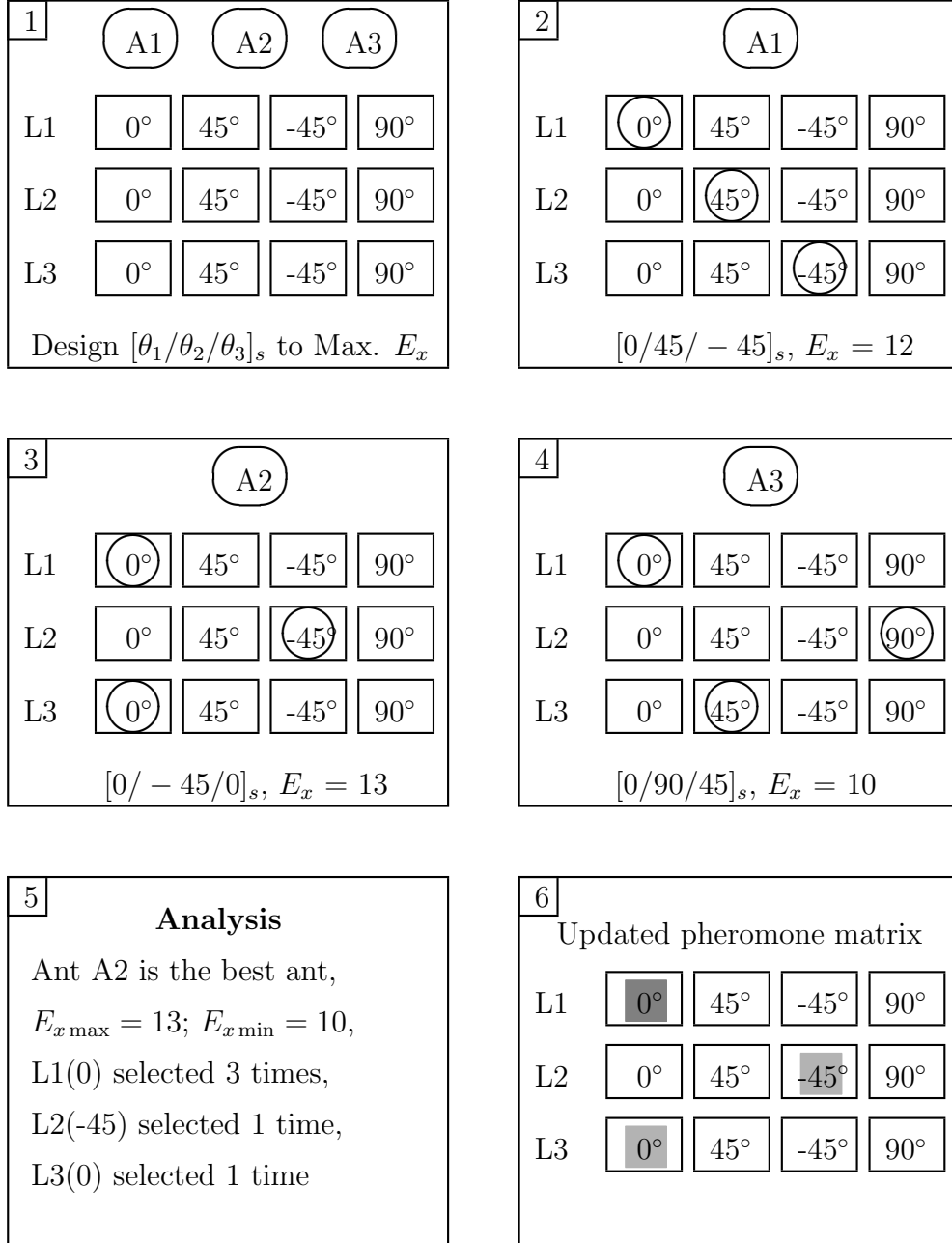
Figure 4.2: Simple example of the Ant Colony Optimization algorithm (white color for all orientations in the beginning means equal pheromone concentrations while at the end the color concentration follow the pheromone concentration).

(n), a vector C contains the possible orientation angles and the number of design variables (NV),

- Assume equal pheromone concentrations, τ_{ij}, through the pheromone matrix for the first iteration where $i = 1 : n$ and $j = 1 : NA$.

Step 2:

- Compute the probability P_{ij} of ant k to select a certain orientation as:

$$P_{ij}^k = \frac{\tau_{ij}^\alpha}{\displaystyle\sum_{i=1}^{n} \tau_{ij}^\alpha} \tag{4.13}$$

where α is a parameter used to denote the degree of importance of pheromone. In the first step all pheromone concentration values are the same, therefore the selection is made randomly.

Step 3:

- For each layer in the laminate, generate a random number. Based on this number and on the probability matrix values, select the orientation for the layer under consideration,

- Repeat the same for each layer until selecting the whole stacking sequence,

- Repeat the previous procedure for each ant until each ant is attributed a stacking sequence.

Step 4:

- Evaluate the objective function for each stacking sequence and check for failure,

- Reject stacking sequences with failure indices higher than one,

- From the accepted stacking sequences, select the one with the best objective function, f_{best}, and the one with the worst objective function, f_{worst}.

Step 5:

- If all the stacking sequences result in the same value of the objective function (i.e $f_{\text{best}} = f_{\text{worst}}$), this corresponds to all ants having chosen the same path, therefore the algorithm has converged.

- If not:

    - Calculate the amount of pheromone deposited on each path with the best value of the objective function as:

$$\Delta\tau = \frac{\zeta f_{\text{best}}}{f_{\text{worst}}} \tag{4.14}$$

      where ζ is a parameter used to control the additional pheromone amount. The criterion to calculate the amount of pheromone deposited on the best stacking sequence is the main difference between the present model and the AC algorithms used by different authors. Here, the criteria presented by Rao [136] is adopted. Aymerich and Serra [110] used the best value of the objective function divided by 10. Bloomfield et al. [112] used the inverse of the objective function as the amount of the pheromone deposited. Wang et al. [137] defined the pheromone deposited as a function of the global optimum, the local optimum, the path with the maximum length, and the pheromone evaporation rate.

    - Calculate the new pheromone matrix as:

$$\tau^{\text{new}} = (1 - \rho)\tau^{\text{old}} + NT\Delta\tau \tag{4.15}$$

      where NT is the number of ants that selected the orientation under consideration for the layer under consideration, and ρ is the pheromone evaporation rate. This parameter simulates the environmental effect on the behavior of the real ants. In the search algorithm, the parameter ρ is used to avoid premature convergence to local optimum.

    - Return to step 2.

4.5 Optimization for Buckling and Strength

For the plate under biaxial compression, the optimization problem is formulated with the objective of maximizing the load multiplier, λ_c, under failure constraints (the panel is considered to fail if it buckles or if any of the failure indices exceeds 1). With respect to the biaxial tensile loading conditions, two formulations are considered. The first formulation considers the matrix cracking (FI_{MT}) as the most important failure index. The second one considers equal importance of the matrix cracking and the fiber tensile (FI_{FT}) failure indices (multi-objective optimization). The differences between the three different formulations are shown in Table 4.1.

Table 4.1: Formulation of the optimization problems.

	Biaxial compression	Biaxial tension	
		Single objective	Multi-objective
Objective	Max. λ_c	Min. FI_{MT}	Min. $0.5(FI_{MT} + FI_{FT})$
Constraints	$FI_{\max} \leq 1.0$	$FI_{\max} \leq 1.0$	$FI_{\max} \leq 1.0$

Symmetry and balance constraints are taken into account in the formulation of the algorithm. The symmetry is achieved by designing only one half of the laminate and mirroring the second half. The balancing is achieved by assuming that each layer oriented at an angle of θ should be followed by another layer at an angle of $-\theta$, which reduces the number of the design variables to one quarter of the number of layers, when symmetry is also imposed. To minimize the matrix cracking failure indices, the number of possible clustered plies oriented at 0° or 90° is limited to four as suggested in [124].

4.6 Results and discussion

4.6.1 Algorithm parameters

The AC algorithm is dependant on four parameters: NA, ρ, ζ and α. All of these parameters affect the quality of the optimum solution and the computational time required to obtain this optimum [110, 112]. There is no clear trend to decrease the computational time and minimize the difference between predicted optimal solution

and the global optimal. For this reason, a parameter analysis has been performed
in this study to select the optimum parameters using the data published by Kogiso
et al. [114]. A biaxial compression loading is applied to a carbon/epoxy panel with
the specifications summarized in Table 4.2.

Table 4.2: Specifications of the test problem.

Geometrical	$a = 508$ mm, $b = 127$ mm, $NL = 48$ layers
Loading	$N_x = 175$ N, $N_y = 87.5$ N
Elastic properties	$E_1 = 127.59$ GPa, $E_2 = 13.03$ GPa, $G_{12} = 6.41$ GPa, $\nu_{12} = 0.3$
Allowable strains	$\varepsilon_1^{all} = 0.008$, $\varepsilon_2^{all} = 0.029$, $\gamma_{12}^{all} = 0.015$

The problem is solved using the conventional orientations and the maximum
strain failure criteria, as in [114], reaching the same predicted optimum solution
$([90_2/\pm45_2/(90_2/\pm45)_2/\pm45_5]_s)$. Different values are tried for each parameter and
the optimum parameters, in terms of the computational time and the quality of the
solutions, are found as: $NA = 50$ ants, $\rho = 0.05$, $\zeta = 1.2$ and $\alpha = 1.0$.

In this problem, there are many near optimal designs. For this reason, designs
that are within a tenth of a percent of the best predicted optimum are accepted
as optimal and are called practical optima here. To evaluate the efficiency of the
algorithm Kogiso et al. [114] define a normalized price, which is the average number
of evaluations (also called price) of the objective function divided by the probability
of reaching a practical optimum (called practical reliability).

The normalized prices are 661, 832 and 686 for the current study, the GA opti-
mization [114] and the AC optimization [110], respectively. This result shows that
the AC optimization is better than the GA's in terms of the computational time.
The comparison between the normalized prices of the current AC optimization with
the one published in [110] shows that the values are very close and the effect of the
criterion to calculate the amount of pheromone deposited can be ignored.

4.6.2   Selection of the failure criteria

As mentioned in Section 4.3.2, the idea behind this section is to check the accu-
racy of the results obtained using a simple failure criterion (like the maximum strain

and Tsai-Wu) with respect to more accurate, but more complicated failure criteria (such as LaRC03).

A rectangular panel with the same dimensions as in [114] ($a = 508$ mm and $b = 127$ mm) is loaded in biaxial compression, as in Section 4.6.1. The plate is optimized for maximum buckling load, as summarized in Table 4.1. The results obtained using the different failure criteria are summarized in Table 4.3. The stacking sequences shown are the best of 50 runs for each failure criterion.

Table 4.3: AC predicted stacking sequences using different failure criteria and the corresponding load multiplier λ_c.

Criteria	Stacking Sequence	λ_c
Maximum strain	$[(\pm 45/ \pm 50_2)_2/ \pm 50_2/ \pm 65/ \pm 85/ \pm 10_2]_s$	15021
Tsai-Wu	$[\pm 50_4/ \pm 45_3/(\pm 50/ \pm 45)_2/ \pm 40]_s$	15141
LaRC03	$[\pm 50_3/ \pm 45/ \pm 50_2/ \pm 45_4/ \pm 50_2]_s$	15142

From the table, it is clear that there are some differences between the predictions in terms of the load multiplier values and the stacking sequence for the three failure criteria. These differences can be understood when comparing the failure surfaces corresponding to each failure criteria at the critical stress level of the predicted optimum solution.

The critical stresses are σ_{11} = -1524 MPa, σ_{22} = -1 MPa and σ_{12} = 0 MPa for the maximum strain criterion, σ_{11} = -1125 MPa, σ_{22} = -31 MPa and σ_{12} = 81 MPa for the Tsai-Wu criterion and σ_{11} = -241 MPa, σ_{22} = -78 MPa and σ_{12} = 120 MPa for the LaRC03 failure criteria. With respect to the results obtained using the maximum strain criteria, they refer to a nearly uniaxial compression state of stress. At this stress level, the failure surfaces of the three failure criteria reach the same point (the longitudinal compressive strength, X^C). This means that the maximum strain predictions fall into the feasible region of both Tsai-Wu and LaRC03 failure criteria. On the other hand, the optimum solution obtained using the Tsai-Wu criterion is out-of-feasible region of the LaRC03 criteria. Ten practical optimal solutions were checked in the same way and the same response was found.

As a summary to the current study, the maximum strain failure predictions fall within the LaRC03 feasible region but its predicted load multiplier is relatively

smaller. On the other hand, the Tsai-Wu predictions fall out of the LaRC03 failure envelope. These results are similar to the ones found by Lopez et al. [131] when comparing the maximum strain, the Puck, and Tsai-Wu criteria using the GA. Based on these results, the LaRC03 failure criteria is selected for the remaining analyzes, in spite of the consequent higher computational time due to its physically nature and capability to identify different failure modes.

4.6.3   Biaxial compression

The same panel dimensions used in the previous sections are used here. Using the same material characteristics and panel dimensions as in the previous section, the calculated optimum stacking sequences and the corresponding load multiplier λ_c are presented in Table 4.4. The results are obtained at three different load ratios; $N_y / N_x = 0.125$, 0.25 and 0.5. Three practical optimum solutions are presented for each case.

Table 4.4: Conventional (Con.) vs. dispersed (Dis.) optimum stacking sequences for diffract loading ration.

N_y/N_x	Orientation	Stacking Sequence	λ_c
0.125	Con.	$[\pm45_{12}]_s$	14769
		$[\pm45_{11}/90_2]_s$	14768
		$[\pm45_{10}/90_2/\pm45]_s$	14763
	Dis.	$[\pm50_3/\pm45/\pm50_2/\pm45_4/\pm50_2]_s$	15142
		$[\pm50_3/\pm45_2/\pm50_3/\pm45/\pm50_3]_s$	15142
		$[\pm50_2/\pm45/\pm50_3/\pm45/\pm50/\pm45_3/\pm55]_s$	15142
0.25	Con.	$[\pm45_2/90_2/\pm45_9]_s$	12288
		$[\pm45_3/90_2/\pm45_4/90_4/\pm45_2]_s$	12287
		$[\pm45_4/90_2/\pm45_2/90_4/\pm45_2/90_2]_s$	12287
	Dis.	$[\pm55_9/\pm50/\pm55/\pm60]_s$	13062
		$[\pm55_9/\pm50_2/\pm60]_s$	13062
		$[\pm55_8/\pm50/\pm55_3]_s$	13061
0.5	Con.	$[(90_2/\pm45)_2/\pm45_4/(90_2/\pm45)_2]_s$	9138
		$[(90_2/\pm45)_2/\pm45/90_4/\pm45_3]_s$	9138
		$[(90_2/\pm45)_3/\pm45/90_2/\pm45]_s$	9138
	Dis.	$[(\pm60_2/\pm65)_2/\pm60_3/\pm65_3]_s$	9863
		$[\pm\pm60_2/\pm65/\pm60_3/\pm65_2/\pm60_2/\pm65/\pm55]_s$	9863
		$[(\pm60_2/65)_3/\pm60/\pm55/\pm50]_s$	9863

The comparison between the results, obtained using both conventional and dispersed ply orientations, shows that usually the optimum buckling load multiplier is higher when using dispersed orientations. The increase in the optimum load is 2.5%, 6.3% and 8% for the different load ratios. This increase was expected due to the higher freedom to select the ply orientations. It can be noticed that the improvement in the load capacity varies with the load case. The higher the N_y/N_x load ratio, the higher the relative increase in λ_c for the dispersed laminates.

It can also be noticed that, for the same load ratio, the predicted loads are very close and sometimes they are equal. This gives the designer the freedom to select the best one based on the manufacturing capabilities and also the application.

4.6.4 Biaxial tension

Single objective optimization

The effect of stacking sequence dispersion on the matrix cracking failure index is checked in the current loading conditions. The importance of the matrix cracking failure index arises from the fact that delamination can be triggered by matrix cracking [51].

A biaxial tensile loading is applied to a flat panel with the following geometric characteristics: $a = b = 500$ mm and 48 layers. The problem is studied at different loading ratios, N_y / N_x = 0.2, 0.4, 0.6, 0.8 and 1. Figure 4.3 shows the matrix cracking failure index according to LaRC03 corresponding to the obtained optimum stacking sequence at each loading ratio, and Table 4.5 summarizes the resulting optimum stacking sequences.

The results show that the failure index for matrix cracking can be decreased by using the dispersed orientation angles. The decrease ranges from almost 100% at loading ratio 0.2 to 20% at loading ratio 1. This is the result of the higher freedom given to the algorithm when selecting the ply orientations.

Multi-objective optimization

The previous set-up and loading conditions are considered here. The objective now is to minimize both failure indices (the tensile matrix cracking FI_{MT} and the tensile fiber FI_{FT} failure index). The importance of minimizing the matrix cracking
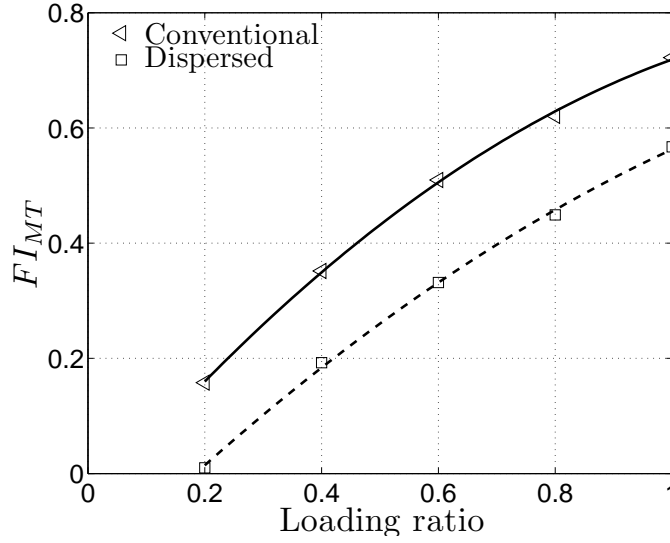
Figure 4.3: Matrix tensile failure index as a function of N_y/N_x (conventional vs. dispersed).

Table 4.5: Optimum stacking sequence at different loading ratio using both the conventional (Con.) and the dispersed (Dis.) orientations.

N_y/N_x	Orientation	Stacking Sequence
0.2	Con.	$[0_4/\pm 45_3/(\pm 45/0_2)_2/\pm 45_2/0_2]_s$
	Dis.	$[\pm 30_2/\pm 35/\pm 30/\pm 25_2/\pm 30_2/\pm 35/\pm 30/\pm 35_2]_s$
0.4	Con.	$[0_2/\pm 45_{10}/0_2]_s$
	Dis.	$[\pm 30/\pm 35/\pm 40_3/\pm 35_2/\pm 40_2/\pm 30/\pm 40/\pm 30]_s$
0.6	Con.	$[\pm 45/0_2/\pm 45_7/0_2/\pm 45_2]_s$
	Dis.	$[\pm 5/\pm 50_2/\pm 40/\pm 50/\pm 45_2/\pm 40/\pm 45/\pm 40/\pm 50/\pm 20]_s$
0.8	Con.	$[\pm 45_3/0_2/\pm 45_8]_s$
	Dis.	$[\pm 5/\pm 50_2/\pm 55_2/\pm 50/\pm 55_2/\pm 50_3/\pm 20]_s$
1	Con.	$[\pm 45/(0_2/90_2)_2/\pm 45_2/(90_2/0_2)_2/\pm 45]_s$
	Dis.	$[\pm 5/\pm 55/\pm 60_2/\pm 55_6/\pm 60/\pm 25]_s$

failure index, as mentioned before, is the initiation of delamination whereas the fiber fracture can cause the catastrophic failure of the structure. The weights of each failure index in the objective function are set equal. The graph in Figure 4.4 shows the matrix cracking and fiber failure indices corresponding to the optimum stacking sequence at each loading ratio, and Table 4.6 depicts the optimum stacking sequences at different loading ratios.
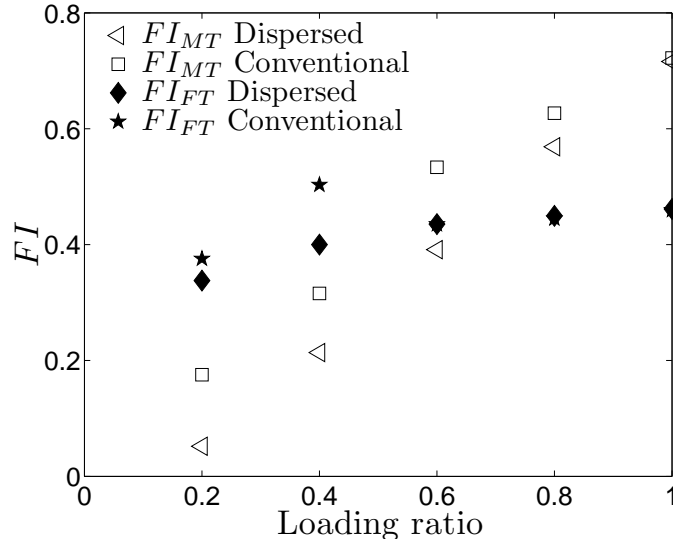
Figure 4.4: Matrix tensile and fiber tensile failure indices as a function of N_y/N_x (conventional vs. dispersed).

Table 4.6: Optimum stacking sequences at different loading ratio using both the conventional (Con.) and the dispersed (Dis.) orientations.

N_y/N_x	Orientation	Stacking Sequence
0.2	Con.	$[0_2/\pm 45/(\pm 45/0_2)_3/0_2/\pm 45_2/0_2]_s$
	Dis.	$[\pm 25/\pm 30_3/\pm 25_3/\pm 30_2/\pm 25/\pm 20/\pm 25]_s$
0.4	Con.	$[(0_2/\pm 45_2)_2/\pm 45_5/0_2]_s$
	Dis.	$[\pm 25_2/\pm 40/\pm 30/(\pm 40/\pm 35)_2/\pm 45/\pm 35/\pm 40/\pm 25]_s$
0.6	Con.	$[\pm 45_2/(0_2/90_2/0_2/\pm 45)_2/0_2/\pm 45]_s$
	Dis.	$[\pm 30/\pm 40/\pm 45/\pm 40_2/\pm 35/\pm 40_2/\pm 45/\pm 50/\pm 40/\pm 30]_s$
0.8	Con.	$[(\pm 45/0_2)_2/(90_2/\pm 45)_2/0_2/90_2/0_2/\pm 45]_s$
	Dis.	$[\pm 35/\pm 50/(\pm 40/\pm 45_3)_2/\pm 40_2]_s$
1	Con.	$[\pm 45_2/0_2/\pm 45_7/90_2/\pm 45]_s$
	Dis.	$[\pm 10/\pm 45_2/\pm 55/\pm 65_3/\pm 35/\pm 20/\pm 50_2/\pm 30]_s$

The results show that, at low values of the loading ratio, the usage of the dispersed laminates improves both failure indices. This improvement is a consequence of the improvement in the global panel properties allowed by the optimization process. The maximum improvements are 70% for the matrix cracking failure index (FI_{MT}) and 20% for the fiber tension failure index (FI_{FT}). At higher values of the loading ratio the two optimum solutions are coincident. This is due to the fact that

the optimum solution, at higher loading ratios, is $[\pm 45]_{12\mathrm{s}}$ but, due to the strength constraints, the algorithm replaces some of the 45° layers with other orientations.

4.7   Conclusions

The Ant Colony Optimization algorithm was used to optimize laminated panels subjected to biaxial loading (compression and tensile). The algorithm was implemented and validated using data available in the literature [114].

A study was conducted to check the validity of using a simple failure criteria (for example the maximum strain criterion or the Tsai-Wu criterion) instead of the physically-based failure criteria that usually require higher computational time. The results showed that the use of the maximum strain criterion usually leads to local optima while the Tsai-Wu leads to out-of-feasible region solutions as compared to the physically-base LaRC03 failure criteria. Thus, it was decided to use the LaRC03 failure criteria in spite of its associated computational time given to the reliability of the results.

With respect to the biaxial compression loading condition, the problem was formulated to maximize the critical buckling load under strength constraints (LaRC03 failure criteria). For the biaxial tensile loading case, the problem was modeled in two ways: as a single-objective optimization to minimize the matrix cracking failure index, and as a multi-objective optimization to minimize both the matrix cracking and the fiber tensile failure indices. The results showed that, by using the dispersed laminates, the improvement in the buckling load ranged from 2.5% to 8% with respect to the loading ratio. For the tension case, the failure index for matrix cracking could be reduced by up to 100% due to the capabilities of the dispersed laminates to transfer the loading from the transverse weak direction to the longitudinal strong one. These improvements are obtained due to the higher freedom given to the algorithm when selecting the stacking sequences.

Chapter 5

Optimization for Low Velocity Impact

5.1   Overview

In Chapter 4, the AC algorithm was summarized, implemented, tested and used to compare the response of conventional and non-conventional laminates under in-plane biaxial loading. In this chapter, the same optimization strategy is used for laminated plates under low velocity and large mass impact event. A review of the analytical developments found in the literature to model the quasi-isotropic behavior of laminated composite plates under low velocity large mass events is presented in Section 5.3. The plate is subjected to variable impact energy (E_i = 10, 15, 20, 25, 30, 40 and 50 J). The layer orientation angle is modeled as a discrete variable with values ranging from -85° to 90°, with 5° jumps. Two case studies are optimized. In the first case, the projected delamination area is minimized because the projected damage area is used to infer the damage resistance of aeronautical composites. In the second case study, the threshold delamination load (the load at which unstable delaminations grow) and the maximum impact load are optimized in order to increase the absorbed elastic strain energy. The problem is constrained by the mass criteria, the quasi-static condition, the perforation threshold load and the plate stiffness properties.

5.2   Introduction

Low velocity impact on laminated composites is considered potentially danger-
ous, mainly because the resulting damage might be undetected, specially at lower
impact energies. Low velocity impacts in CFRP laminates can create damage which
may involve indentation, matrix cracking, fiber matrix debonding, delamination and,
eventually, fiber breakage for higher impact energies. Even when no visible impact
damage is observed at the surface (energies below Barely Visible Impact Damage,
BVID), matrix cracking and interlaminar failure can occur, and the carrying load
capacity of composite laminates is considerably reduced [33].

Among the analytical and experimental studies found in the literature, relatively
few optimization studies were conducted on impact response of laminated compos-
ites. Rahul et al. [20, 21] conducted a FE-based optimization with GA to minimize
both the laminate thickness and the manufacturing costs under low velocity impact.
Their results showed that the optimum solution was completely dispersed in terms
of stacking sequence, i.e. the optimum stacking sequences were not restricted to
plies with 0°, 45°, 90° orientations, and without clustering (plies of the same orien-
tation blocked together). Using a similar approach, Nguyen et al. [138] performed a
FE-based optimization with genetic algorithms to minimize the back-face displace-
ment for a laminate under high velocity impacts. Ferreira et al. [139] performed an
analytically-based optimization using the simulated annealing algorithm to minimize
the plate thickness, for small mass impact event. They validated the analytically
obtained stacking sequences by means of numerical simulations and good agreement
was obtained.

5.3   Low Velocity Impact on Laminated Plate

5.3.1   Impact event classification

The proper classification of an impact event defines the way by which this event
can be modeled. As an example, in the case of impact with a low velocity and a
large mass, the problem can be simulated by quasi-static formulations (treating the
problem as an equivalent static problem with a static load applied to the impact
site) [140, 141]. Impacts are often categorized in the literature as low velocity, high

velocity or hyper velocity. According to different authors, low velocity impacts are bounded by impact velocities under 5 m/s [142] or 15 m/s [76]. High velocity impact events are assumed to involve velocities up to 2500 m/s, while higher velocities characterize hyper velocity events [143].

The problem of that classification is that there is not a clear transition between categories and authors disagree on its definition [144]. Consequently, another criteria was developed by Olsson [49, 145] to categorize the impact event based on the impactor/plate mass ratio. The theory classifies the impact event as small mass (Figure 5.1 (a)), large mass (Figure 5.1 (c)) or intermediate mass (Figure 5.1 (b)) impactor. For a semi-spherical impactor and a rectangular composite plate of length a and width b, the criterion used to define a small mass impact is [145]:

$$M_i \leq \frac{M_p}{\sqrt{2}\pi} \min\left[\frac{a}{b}\left(\frac{D_{22}}{D_{11}}\right)^{0.25}, \frac{b}{a}\left(\frac{D_{11}}{D_{22}}\right)^{0.25} \right] \tag{5.1}$$

whereas, a large mass impact is considered if:

$$M_i \geq 2M_p \tag{5.2}$$

Intermediate mass impact is then defined by:

$$2M_p \geq M_i \geq \frac{M_p}{\sqrt{2}\pi} \min\left[\frac{a}{b}\left(\frac{D_{22}}{D_{11}}\right)^{0.25}, \frac{b}{a}\left(\frac{D_{11}}{D_{22}}\right)^{0.25} \right] \tag{5.3}$$

where M_i is the impactor mass, M_p is the plate mass and D_{ij} are the components of the bending stiffness matrix.

(a) Small mass   (b) Intermediate mass   (c) Large mass
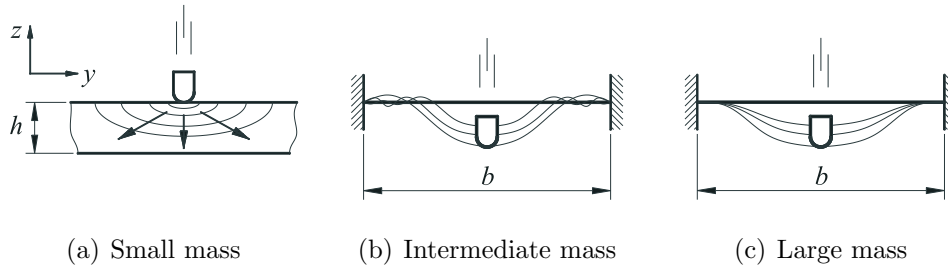
Figure 5.1: Description of the mass criteria.

5.3.2   Impact characterization diagram

The impact characterization diagram proposed by Christoforou and Yigit [146–151] predicts the behavior type, as well as the elastic peak impact force for a wide range of impact cases. The construction of the diagram is based on simplified analytical models of the infinite plate (at which the boundary conditions do not affect the response [151]) and the quasi-static impact behaviors. Ballistic impact, a low mass high velocity impact, is beyond the scope of the characterization diagram.
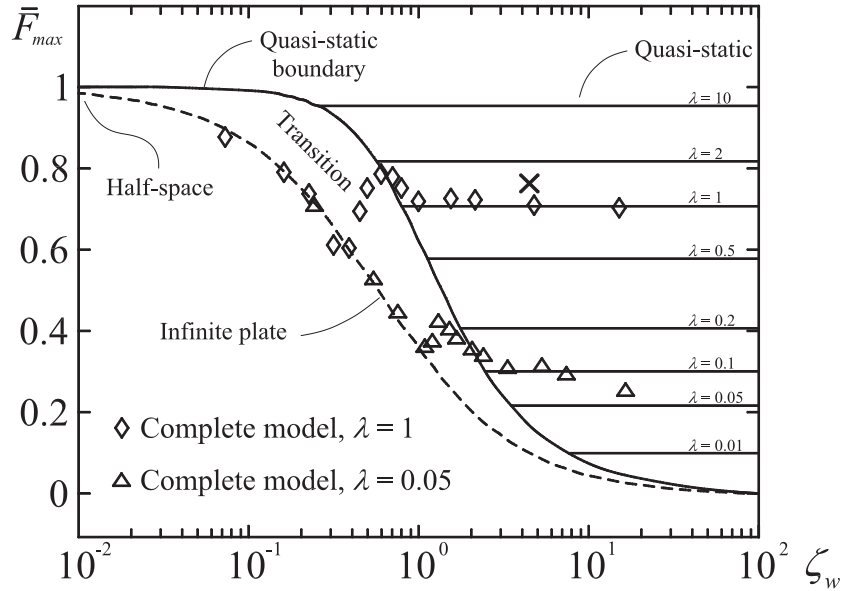
Figure 5.2: The impact characterization diagram (after [146–151]).

Four different regions can be identified in the diagram, Figure 5.2. Impact configurations which define points in the right part of the diagram behave as quasi-static. Points that fall on or close to the dashed curve behave as infinite plate. Between the quasi-static and the infinite plate behaviors there is a transition zone where the resulting response is a combination of both. Finally, the points that fall close to the maximum dimensionless force result in the half-space behavior. The numerical validation of the characterization diagram is found in [149], whereas the experimental one is found in [151].

The curve that represents the boundary of the quasi-static response was obtained by [149, 152]:

$$\bar{F}_{\text{max}} = \sqrt{\frac{0.68}{0.68 + \zeta_w}} \tag{5.4}$$

where ζ_w is a dimensionless parameter defined as the loss factor [146], relative plate mobility [145], or inelastic parameter [147, 153]. The value of ζ_w can be defined as:

$$\zeta_w = \frac{1}{16} \sqrt{\frac{K_\alpha M_i}{I_1 D^*}} \tag{5.5}$$

where K_α is the contact stiffness ($K_\alpha = 5.2 R_i Y^C$ [146] or $K_\alpha = 10.4 R_i S^L$ [150]), R_i is the impactor radius, Y^C is the transverse compression strength, S^L is the in-plane shear strength, I_1 is an inertia term ($I_1 = M_p/ab$ [51]) and D^* is the plate effective bending stiffness which is defined by expressions involving elliptic functions [51]. A sufficient approximation for D^* is [145, 154]:

$$D^* = \sqrt{\frac{A+1}{2} D_{11} D_{22}}, \text{ where } A = \frac{D_{12} + 2D_{66}}{\sqrt{D_{11} D_{22}}} \tag{5.6}$$

It is worth remarking that the predictions of Eq. (5.6) become inaccurate when A is not close to unity [155]. Another approximation for D^* is found in [149, 150] as:

$$D^* = \frac{1}{2} \left(D_{12} + 2D_{66} + \sqrt{D_{11} D_{22}} \right) \tag{5.7}$$

The second dimensionless parameter in Figure 5.2 is λ which is termed as the relative stiffness. It can be defined as the ratio between the plate bending-shear stiffness K_{bs} and the contact stiffness K_α ($\lambda = K_{bs}/K_\alpha$). The value of the bending-shear stiffness K_{bs} can be calculated as [149]:

$$K_{bs} = \frac{D^*}{0.0116 a^2} \tag{5.8}$$

where a is the plate length.

In the case of a low velocity impact with a large mass impactor, the impact response is adequately reproduced by a simplified quasi-static impact model [146, 149, 156]. In such cases, the normalized impact response is governed by the single non-dimensional parameter, λ. It follows that the normalized impact force depends only on λ, and is given as [149]:

$$\bar{F}(\bar{t}) = \sqrt{\frac{1+\lambda}{\lambda}} \sin\left(\sqrt{\frac{1+\lambda}{\lambda}}\bar{t}\right) \qquad (5.9)$$

where $\bar{F}(\bar{t})$ is the impact force normalized by the maximum impact force for a half-space behavior, given by [149, 157]:

$$\bar{F}(\bar{t}) = \frac{F(\bar{t})}{V_0\sqrt{M_i K_\alpha}} \qquad (5.10)$$

where $\bar{t}$ is the normalized contact time ($\bar{t} = \omega t$), ω is the contact frequency ($\omega = \sqrt{K_\alpha/M_i}$) and V_0 is the initial impactor velocity.

From Eq. (5.9), the maximum normalized impact force can be obtained at $d\bar{F}/d\bar{t} = 0$ and $\bar{t} \neq 0$. The corresponding normalized time is given by:

$$\bar{t} = \frac{\pi}{2}\sqrt{\frac{1+\lambda}{\lambda}} \qquad (5.11)$$

whereas the value of the maximum normalized force is given by:

$$\bar{F}_{\max} = \sqrt{\frac{\lambda}{1+\lambda}} \qquad (5.12)$$

From Eq. (5.4) and (5.9), the limit of the quasi-static response, in terms of the two nondimensional parameters ζ_w and λ, is given as:

$$\zeta_w \geq \sqrt{\frac{0.68}{\lambda}} \qquad (5.13)$$

5.3.3   Projected delamination area

The shape of a delamination is generally that of an oblong peanut, where its major axis follows the orientation of the ply at the interface which is more distant from the impact point [143, 158]. This shape is a result of the shear stress distribution around the surrounding area of the impactor, of the low interlaminar shear strength along or close to the direction of the fibers, and of the matrix cracks created by the flexural in-plane stresses [84, 159].

Assuming a two-layer plate and based on the bending stiffness mismatch between the two layers, Liu [160] proposed a mismatch parameter M_L to assess the delamination area. The larger the mismatch parameter the larger the impact damage area is.

This parameter is not applicable for laminated plates with more than one interface. To solve this limitation, Morita et al. [161] proposed a new parameter M_M which is calculated as:

$$M_M = \frac{1}{2\pi} \int_0^{2\pi} \frac{[\Delta C_{11}(\theta) z_i]_{max}}{D_{11}(\theta)} d\theta \qquad (5.14)$$

where $\Delta C_{11}(\theta)$ is the difference of the in-plane stiffness between the adjacent plies in the direction θ, z_i is the through-the-thickness distance from the midplane to the considered interface, and $D_{11}(\theta)$ is the bending stiffness of the entire laminate in the direction θ.

A more simplified approach to calculate the projected damage area was adopted by Jackson and Poe [162]. They semi-empirically correlated the projected delamination area A_d to the dimensional impact force F and the interlaminar shear strength S^L as:

$$A_d = \frac{1}{4\pi h^2} \left(\frac{F}{S^L}\right)^2 \qquad (5.15)$$

Following a similar approach, Davies and Zhang [163] proposed the following formula to the maximum impact damage area A_d under quasi-static conditions:

$$A_d = \frac{9}{16\pi h^2} \left(\frac{F}{S^L}\right)^2 \qquad (5.16)$$

It should be noted that the delamination size predicted with Eq. (5.16) is 2.25 times the one predicted by Eq. (5.15). From Eq. (5.10), (5.12) and (5.16), the maximum delamination area for a rectangular plate of thickness h impacted with a semi-spherical impactor of mass M_i under quasi-static conditions can be calculated as:

$$A_d = \frac{9\lambda M_i K_\alpha}{16\pi(1+\lambda)} \left(\frac{V_0}{hS^L}\right)^2 \qquad (5.17)$$

It is worth remarking that Eq. (5.15), (5.16) and (5.17) were obtained assuming a circular delamination shape and the maximum delamination is assumed to occur at the plate mid-thickness. The first assumption is true, in some cases, when considering the projected delamination area, [164], but wrong when considering only

one delamination [129]. The second assumption can be considered true for thick laminates but for thin ones it is not [165]. For these reasons the delamination area, predicted by Eq. (5.17), is expected to be smaller than the real one (as can be realized from [163]). Through out this work, the value of A_d is used as a qualitative indicator of the induced damage i.e. it is not to be compared with experimental values. The higher the value of A_d, the larger the expected damage area.

5.3.4   Delamination threshold force

The delamination threshold can be defined as the load level at which the first unstable delamination appears. On the load-displacement curve, this load can be considered as the first sharp decrease in the stiffness, Figure 5.3.
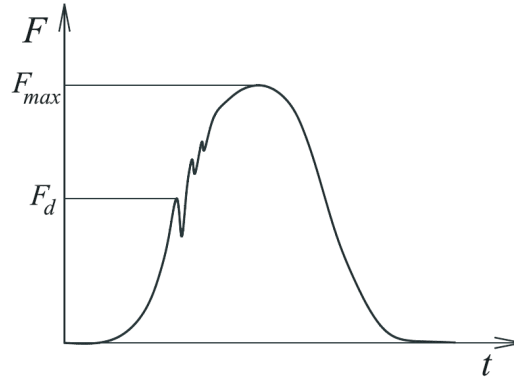
Figure 5.3: Representative impact force versus time history.

Using the Linear Elastic Fracture Mechanics (LEFM) for a simply supported isotropic plate under static out-of-plane loading and assuming that only one circular mid-plane delamination occurs, Davies et al. [50] proposed an equation to predict the threshold load for delamination as:

$$F_{d1}^{\text{stat}} = \frac{\pi}{3} \sqrt{\frac{8EG_{IIc}}{1 - \nu^2}} h^{1.5} \tag{5.18}$$

where G_{IIc} is the fracture toughness in mode II loading and h is the plate thickness. The term $E/(1 - \nu^2)$ in isotropic plates is equivalent to $12D^*/h^3$ in orthotropic plates [49]. Hence, Eq. (5.18) can be rewritten as:

$$F_{d1}^{\text{stat}} = \pi \sqrt{\frac{32D^*G_{IIc}}{3}} \tag{5.19}$$

A more rigorous solution for an arbitrary number of delaminations nd located at equal intervals through-the-thickness of the plate was derived by Suemasu and Majima [166]. This criterion was also developed later by Olsson et al. [167]. The threshold, in this case, is defined as:

$$F_{dn}^{\text{stat}} = \pi\sqrt{\frac{32D^*G_{IIc}}{nd+2}} \tag{5.20}$$

To take into account the dynamic effects in low velocity impact events, Olsson et al. [167] added a correction factor to Eq. (5.20). The resulting delamination threshold load was given by:

$$F_{dn}^{\text{dyn}} = 1.213\pi\sqrt{\frac{32D^*G_{IIc}}{nd+2}} \tag{5.21}$$

for an arbitrary number of delaminations nd. For a single mid-plane delamination ($nd = 1$), Eq. (5.21) becomes:

$$F_{d1}^{\text{dyn}} = 1.213\pi\sqrt{\frac{32D^*G_{IIc}}{3}} \tag{5.22}$$

Although Eq. (5.22) was derived assuming small mass impactor and single mid-plane delamination, its predictions were in agreement with the experimental results obtained by González et al. [86] for large mass impact events, especially in cases of almost circular projected delamination areas.

The normalized value of the delamination threshold can be obtained from Eq. (5.22) and (5.10) as:

$$\bar{F}_{d1}^{\text{dyn}} = \frac{F_{d1}^{dyn}}{V_0\sqrt{M_iK_\alpha}} = \frac{F_{d1}^{dyn}}{\sqrt{2E_iK_\alpha}} \tag{5.23}$$

where E_i is the impact energy ($E_i = M_igH_i = 0.5M_iV_0^2$, where H_i is the impactor drop height and g is the gravity).

5.3.5 Fiber perforation threshold

Perforation occurs when the fibers reach their critical strain, enabling the impactor to completely penetrate the material. The perforation energy depends on the total fiber volume of the plate and on the impactor tip shape, whereas the archi-

tecture of the fibers, the stacking sequence of the laminate and the type of matrix have no effect [168, 169].

By considering the Hertz contact law, a uniform distribution of the through-the-thickness shear stress and the quasi-static loading conditions, a perforation threshold load due to laminate shear failure can be obtained as [140, 170]:

$$F_{per}^{sh} = \sqrt{6} \left(\pi S^L h \right)^{3/2} \sqrt{\frac{R_i}{Q_\alpha}} \tag{5.24}$$

where S^L is the shear strength, h is the plate thickness, R_i is the impactor tip radius, and Q_α is the effective contact modulus which can be approached, in orthotropic materials, by $Q_\alpha \approx E_{22}$.

5.4   Optimization Problem Formulation

The AC algorithm, described in Chapter 4, is used here to optimize a plate under low velocity impact loading to improve the damage resistance and/or the damage tolerance. Two optimization case studies are analyzed. In the first case, the projected delamination area is minimized. In the second, the peak load is minimized and the delamination threshold load is maximized in a multi-objective optimization approach with equal weight functions. The objective function for the first case study is:

$$\text{Minimize}: \quad A_d \tag{5.25}$$

whereas for the second one is:

$$\text{Minimize}: \quad \bar{F}_{\max} - \bar{F}_{d1}^{\text{dyn}} \tag{5.26}$$

where A_d is an indicator of the projected damage area predicted by Eq. (5.17), $\bar{F}_{\max}$ is the normalized maximum impact load given by Eq. (5.12), and $\bar{F}_{d1}^{\text{dyn}}$ is the normalized delamination threshold predicted by Eq. (5.23). By minimizing both

the damage area (A_d) and the difference between the dimensionless loads ($\bar{F}_{\max} - \bar{F}_{d1}^{\mathrm{dyn}}$), both the damage resistance and tolerance of the laminate are expected to be improved.

In both cases, the constraints are defined as:

$$0.9E_y \leq E_x \leq 1.1E_y \tag{5.27}$$

$$A_{16}, A_{26} \leq 0.01A_{11} \tag{5.28}$$

$$0.9E_x^{Con} \leq E_x \leq 1.1E_x^{Con} \tag{5.29}$$

$$\zeta_w \geq \sqrt{\frac{0.68}{\lambda}} \tag{5.30}$$

$$F_{\max} < F_{per}^{sh} \tag{5.31}$$

where E_x and E_y are the in-plane stiffness coefficients of the specimen, A_{ij} are the components of the in-plane stiffness matrix and the superscript Con refers to baseline conventional laminate ($[45/0/-45/90]_{3s}$), recommended by the ASTM D7136, low velocity impact test standard [74].

The first constraint, Eq. (5.27), is used to design a laminate with equal in-plane stiffness in both specimen major directions. The second constraint, Eq. (5.28), controls the selection to balanced laminates. In Eq. (5.29), the selection process is forced to those laminates with nearly the same in-plane stiffness as the conventional base line laminate. The quasi-static response is governed by the fourth constraint, Eq. (5.30) (satisfying this condition means that the laminate properties fall into the right part of the characterization diagram, Figure 5.2). The fiber perforation is eliminated by the last constraint, Eq. (5.31). Although it does not appear in the constraints, the mass criterion is considered in the formulation by selecting the number of layers to be 24 to ensure that the mass of the impactor is greater than two times of that of the plate, i.e. large mass impact events (see Eq. (5.2)).

Each of the two case studies is solved twice. In the first time, the problem is solved with the constraints summarized in Eq. (5.27 - 5.31). In the second time, two constraints are added to control the bending stiffness as:

$$0.9E_{fx}^{Con} \leq E_{fx} \leq 1.1E_{fx}^{Con}$$
$$0.9E_{fy}^{Con} \leq E_{fy} \leq 1.1E_{fy}^{Con} \qquad (5.32)$$

where E_{fx} and E_{fy} are the out-of-plane elastic moduli ($E_{fx} = 12/(h^3 D_{11}^{-1})$ and $E_{fy} = 12/(h^3 D_{22}^{-1})$), h is the plate thickness and D_{ij}^{-1} are the components of the inverse of the bending stiffness matrix.

5.5   Specimens and Impact Parameters

The material considered in this study is the AS4/8552 carbon/epoxy composite which properties properties are summarized in Table 2.1. The dimensions of the impact specimen are 150 mm x 100 mm, as proposed in the ASTM D7136 [74] and the Airbus AITM-0010 [76] standards. The effective specimen dimensions (after clamping the edges) are $a = 125$ mm and $b = 75$ mm.

The impact is performed at different impact energies, as recommended by the AITM-0010 standard [76]. The selected values of the impact energies (E_i), mass (M_i), velocities ($V_0 = \sqrt{2E_i/M_i}$) and impact heights ($H_i = E_i/(M_i g)$) are summarized in Table 5.1. The impactor mass is designed to be constant to keep the relative mobility constant at different impact energies (see Eq. (5.5)).

Table 5.1: Impact energies, mass, velocities and drop weight heights.

E_i (J)	10	15	20	25	30	40	50
M_i (kg)	3	3	3	3	3	3	3
V_0 (m/s)	2.6	3.2	3.7	4.1	4.5	5.2	5.8
H_i (cm)	34.0	51.0	68.0	85.0	101.9	135.9	169.9

The in-plane and out-of-plane stiffness and impact dimensionless parameters of the conventional baseline laminate are summarized in Table 5.2. As can be checked, the values of ζ_w and λ are constant at different impact energies due to the constant mass.

Table 5.2: Mechanical properties of the $[45/0/-45/90]_{3s}$ AS4/8552 carbon/epoxy laminate.

E_x GPa	E_y GPa	E_{fx} GPa	E_{fy} GPa	D^* Nm	ζ_w	λ
49.7	49.7	52.35	39.95	377.02	6.10	0.25

5.6 Results and Discussions

In this section, Disp_1 refers to the results obtained without constraining the bending stiffness components (E_{fx} and E_{fy}), while Disp_2 refers to the results obtained by constraining E_{fx} and E_{fy} to the conventional baseline laminate as imposed by Eq. (5.32).

5.6.1 Case study I: damage area optimization

The objective of this case study is to design stacking sequences with an improved impact damage resistance compared to the conventional ones. The objective function is the one presented in Eq. (5.25). Minimizing the damage area is not only helpful for damage resistance but also for damage tolerance.

Figure 5.4 shows the predicted damage area for the three cases (Disp_1, Disp_2 and Con). As mentioned before, the values of the damage area are only qualitative. The optimum solutions for each case are summarized in Table 5.3. It is worth remarking that the problem is multi-optimum, i.e. at each impact energy, many stacking sequences, with the same value of the damage area, are obtained. Only one of them is presented in Table 5.3, for each impact energy.

The results show that the damage area can be decreased by using the non-conventional dispersed orientations compared to the one with conventional orientations, with the same in-plane and out-of-plane stiffness. For the cases at which the out-of-plane stiffness is not constrained, the damage area can be decreased by up to 21%, whereas at the same out-of-plane stiffness the damage area can be decreased by 5% compared to the conventional one. These results agree well with the ones obtained in Chapter 4.

It can be noted from Table 5.3 that the optimum stacking sequence is different
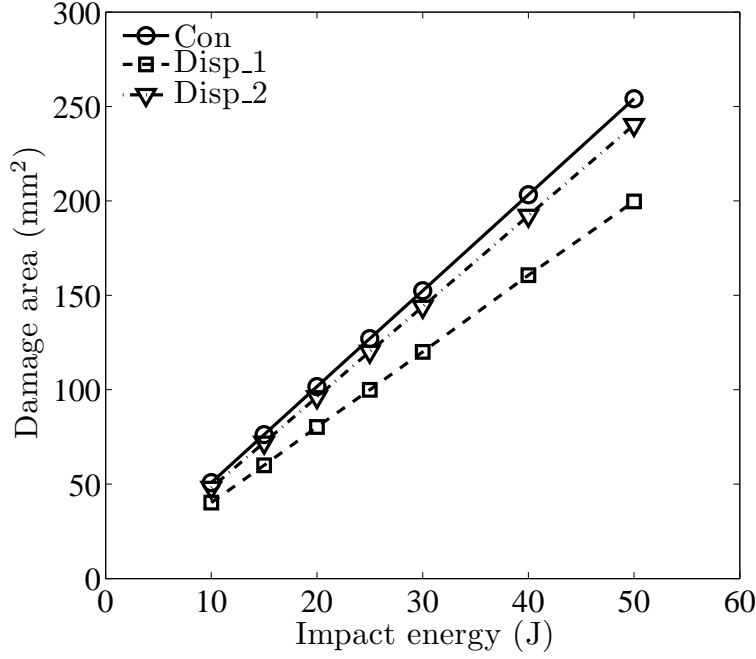
Figure 5.4: Predicted damage area as a function of the impact energy.

Table 5.3: Selected optimum configurations for minimized damage area at different impact energies.

Case	Energy (J)	Stacking sequence
Disp_1	10	$[-85/80/90/80/65/-60/-35/40/10/0/-10/-5]_s$
	15	$[90/-85/80/-75/70/-55/-45/35/5/-10/0/5]_s$
	20	$[85/90/-85/80/-70/55/-30/40/-20/10/0/5]_s$
	25	$[90/85/90/-80/\pm60/-45/30/-15/10/\mp5]_s$
	30	$[\mp85/-85/-80/-75/50/-40/35/-15/\pm5/10]_s$
	40	$[90/-80/85/\pm70/-60/45/-30/\mp10/5/10]_s$
	50	$[90/-85/90/-80/70/-50/\pm40/\pm10/5/0]_s$
Disp_2	10	$[-15/-10/-15/-20/85/80/-60/-85/45/30/35/-55]_s$
	15	$[10/20/15/10/-85/55/90/-85/70/-40/-25/-50]_s$
	20	$[10/20/15/10/-80/-85/55/-85/60/-30/-35/-50]_s$
	25	$[-15/-20/-10/-20/90/\pm80/15/45/-70/45/-80]_s$
	30	$[15/10/15/20/85/-75/-85/45/-30/75/-45/-40]_s$
	40	$[10/20/15/10/-80/-85/55/-85/60/-30/-35/-50]_s$
	50	$[10/20/15/10/-85/55/90/-85/70/-40/-25/-50]_s$

for every applied impact energy. On the other hand, the theoretical response of a composite plate is a function of D^*, ζ_w and λ, and none of these parameters depends on the applied energy if the same impactor mass is used. To clarify this contradiction, each optimal configuration of the case Disp_1 is checked against the other impact energies. The results are summarized in Table 5.4, where the corresponding optimum stacking sequence is noted as Opt_xx, being xx the impact energy. It is shown that the dependency of the optimum configuration upon the impact energy is meaningless. The multi-optimum nature of the problem is what allows obtaining a different optimum configuration for different impact energies. The results show also the capability of the algorithm to find practical optimal solutions within a very small coefficient of variation (CV = 0.26 %).

Table 5.4: Damage area (mm^2) at different impact energies for the optimum configurations of the case Disp_1 summarized in Table 5.3.

	Impact Energy (J)						
Configuration	10	15	20	25	30	40	50
Opt_10	40.19	60.29	80.39	100.49	120.58	160.78	200.97
Opt_15	39.95	59.93	79.9	99.88	119.86	159.81	199.76
Opt_20	40.13	60.19	80.25	100.31	120.38	160.5	200.63
Opt_25	39.97	59.96	79.94	99.93	119.91	159.88	199.86
Opt_30	40.00	60.01	80.01	100.01	120.01	160.02	200.02
Opt_40	40.15	60.23	80.31	100.39	120.46	160.62	200.77
Opt_50	39.94	59.91	79.88	99.85	119.82	159.76	199.7
Average (mm^2)	40.05	60.07	80.10	100.12	120.15	160.20	200.24
SD (mm^2)	0.11	0.16	0.21	0.27	0.32	0.42	0.53
CV (%)	0.26	0.26	0.27	0.27	0.26	0.27	0.26

5.6.2 Case study II: peak and delamination threshold loads optimization

The objective of optimizing the peak and threshold loads is to increase the ratio of the elastically absorbed energy versus the total impact energy. The objective function is the one presented in Eq. (5.26). A comparison between the three cases Disp_1, Disp_2 and Con is shown in Figure 5.5. In the three cases, and at a 10 J impact energy, the value of the peak load is lower than the delamination threshold

which means that no major damage is predicted. Hence, there is no physical meaning for the objective function.
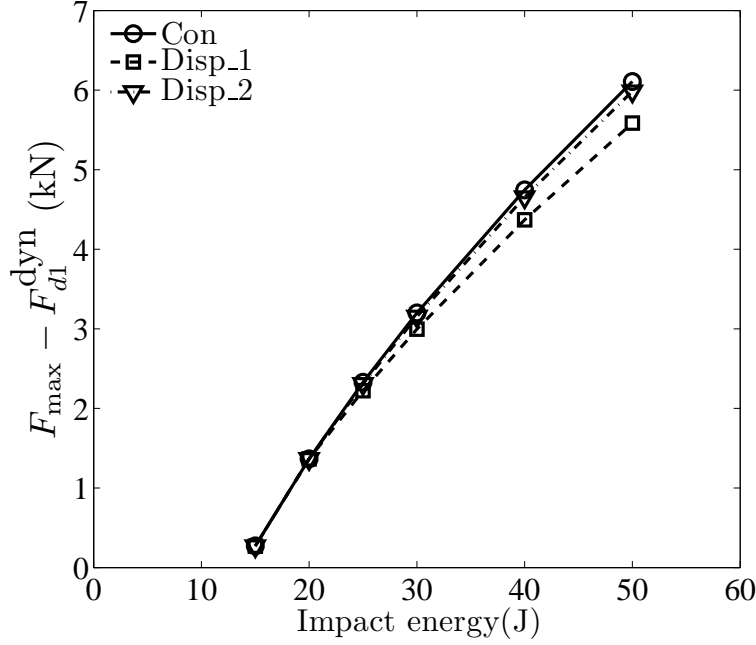
Figure 5.5: The dimensional objective function $(F_{\max} - F_{d1}^{\mathrm{dyn}})$ versus the impact energy.

The results show that the improvement of the objective function, due to using the dispersed laminates, is a function of the impact energy. The improvement ranges vary from 1.5 % at 15 J to 8.5 % at 50 J. The optimum stacking sequence for each impact energy is summarized in Table 5.5.

From Eq. (5.21), it is clear that the delamination threshold is a function of the fracture toughness in mode II (G_{IIc}). As reported by Kim and Mayer [53], this property is a function of the orientation angles of the two plies adjacent to the crack plane. In the conventional laminates, the ply orientation angles are limited to $0°$, $90°$ and $\pm45°$. This means that the interface angles between any two adjacent plies are limited to $45°$ and $90°$ whereas, by using the dispersed orientations, the interface angles can range from $5°$ to $90°$. This means that more possible improvements can still obtained because G_{IIc} at each interface depends on the interface angles. However, the experimental determination of this dependance fact needs more investigation on the fracture toughness test type and on the specimen configuration for multidirectional laminates.

Table 5.5: Optimum configurations for minimized $\bar{F}_{\max} - \bar{F}_{d1}^{\mathrm{dyn}}$ at different impact energies.

Case	Energy (J)	Stacking sequence
Disp_1	15	$[-45/65/20/5/\mp 80/-15/-35/55/-80/-50/10]_s$
	20	$[30/-85/65/35/0/20/-45/-55/90/-10/-35/80]_s$
	25	$[85/90/80/-85/75/-50/40/-30/20/-5/\mp 10]_s$
	30	$[(90/80)_2/-65/\mp 50/35/\mp 5/-10/-5]_s$
	40	$[\mp 85/90/-75/-80/50/-40/30/-20/-10/5/10]_s$
	50	$[\mp 85/90/85/-70/-50/45/20/15/-20/-15/5]_s$
Disp_2	15	$[45/70/-5/85/40/10/-25/-55/20/-70/-40/90]_s$
	20	$[60/0/45/50/80/-10/-75/-5/-65/-85/20/-35]_s$
	25	$[15/20/15/10/-80/90/-80/-20/(65/-45)_2]_s$
	30	$[20/15/10/15/\mp 85/-70/-15/70/-50/65/-45]_s$
	40	$[-10/-15/-20/-10/85/80/-45/-75/-85/40/45/35]_s$
	50	$[15/10/15/20/-80/85/65/90/-15/-45/90/-50]_s$

Another key issue is related to the bending stiffness. Theoretically, the response of a laminated plate under low velocity impact loading depends on the effective bending stiffness (D^*), the relative stiffness (λ) and the relative mobility (ζ_w). It is noted that, for the same values of the three parameters, it is possible to obtain a stacking sequence with high or low values of the bending stiffness coefficients (E_{fx} and E_{fy}). As an example, Table 5.6 shows the detailed characteristics of two nonconventional dispersed configurations, $[35/30/-65/(40/-55)_2/85/-30/-10/-15/80]_s$ (DC_1) and $[0/75/10/-85/-75/60/-20/-50/55/-75/30/-15]_s$ (DC_2), for the same impact energy ($E_i = 30$ J).

Table 5.6: Detailed characteristics of two different stacking sequences.

Configuration	D^* Nm	λ	ζ_w	E_{fx} GPa	E_{fy} GPa	A_d mm^2	$F_{\max}$ kN	F_{d1}^{dyn} kN
DC_1	375.12	0.25	6.12	**25.18**	**28.85**	151.82	9.97	6.77
DC_2	375.96	0.25	6.11	**59.87**	**60.98**	152.10	9.98	6.78

As shown in Table 5.6, the two configurations have almost the same impact

characteristics (D^*, λ and ζ_w) and the same response (A_d, $F_{\max}$ and F_{d1}^{dyn}) although their bending stiffness coefficients are totaly different ($E_{fx}^{\text{DC\_1}} = 0.42 E_{fx}^{\text{DC\_2}}$ and $E_{fy}^{\text{DC\_1}} = 0.47 E_{fy}^{\text{DC\_2}}$). Consequently, the results reported in Table 5.5 do not allow to determine the influence, if any, of the bending stiffness in the global axes on the behavior of the composite plates under low velocity impact. Theoretically, as in Table 5.6, the later have no effect. This topic still needs more experimental investigations to validate the analytical formulations in Section 5.3.

5.7   Conclusions

The effect of dispersing the ply orientations on the response of composite laminated plates under low velocity impact was studied. The ply orientation angle was considered as a discrete variable with possible values ranging from -85° to 90° with 5° jumps. The ant colony algorithm was used to select dispersed stacking sequences able to satisfy all the constraints, and showing improved response, in terms of the damage resistance and the damage tolerance, as compared to conventional laminates.

The results indicate that dispersed laminates can be used to improve the impact performance of advanced composites used in aeronautical industry. Two case studies were considered. In the first case study, the predicted damage area of the dispersed laminate was 21% smaller than for the conventional one. In the second case, the objective function value (the difference between the maximum load and the delamination threshold load) could be improved by 8%. These improvements are due to the high freedom allowed to the algorithm when selecting the stacking sequences. These results support dispersed laminates as a promising concept for more damage resistant and damage tolerant aircraft composite structures.

Chapter 6

Mismatch Angle Effect

6.1 Overview

In Chapter 5, it was analytically demonstrated that, the use of laminates with dispersed fiber orientations can improve the response of laminated plates under large mass and low velocity impact loadings. However, the analytical formulations did not take into account the possible effect of the interface mismatch angle on the fracture toughness (see the results obtained in Chapter 3 and the results reported in [52, 53]). Based on these studies, the interface mismatch angle is expected to influence the delaminations resulting from low velocity impact.

The aim of the current chapter is to compare the experimental response of the dispersed laminates, with different mismatch angles, and the conventional ones (mismatch angle $= 45°$) under low velocity impact and compression after impact loadings. The stacking sequence recommended by the ASTM standard [74] is considered as the baseline conventional configuration. Two dispersed laminates are defined using the ant colony optimization with the same number of layers/interfaces and in-plane and out-of-plane stiffness as the baseline. In the first dispersed laminate, NC_01, the mismatch angle ranges from $10°$ to $30°$, whereas for the second one, NC_02, the mismatch angle ranges from $55°$ to $80°$. No ply clustering is introduced in this study. The three configurations, BL, NC_01 and NC_02, are tested using a drop-weight impact tower at different values of the impact energy, as recommended by the AITM1-0010 standard [76]. After being impacted, the specimens are inspected using ultrasonic non-destructive technology then compressed up to failure to assess

the damage tolerance.

6.2   Introduction

During the life of an aircraft composite part, impacts by foreign objects are expected to occur during the manufacturing, service and maintenance operation. For example; a tool can drop on the structure or impact of a bird or hailstone on the aircraft body. In some impact events, the impact velocity is small but the impactor mass is large. These impacts create an internal damage, consisting of delaminations and back surface tensile failures, that often cannot be detected by visual inspection. This internal damage can cause severe reductions in compressive and shear strength. For this reason, the problem of low velocity and large mass impact received a considerable attention in the literature [153, 158, 171, 172].

Even when no visible damage is observed at the surface (energies below Barely Visible Impact Damage, BVID), low-velocity impact of CFRP laminates creates damage which may involve indentation, matrix cracking, fiber matrix debonding, delamination and, eventually, fiber breakage [33]. Internal matrix cracking and fiber breakage at the contact point appear prior to delaminations [38, 47]. The effects of matrix cracking and/or the localized fiber breakage on the residual strength are limited. However, the matrix cracks trigger delaminations which are the major damage mechanism causing degradation of the composite structural properties [48]. Delaminations propagate, in general, along an axis which orientation is close or equal to the fiber orientation of the under-laying ply [173]. However, for the dispersed laminates tested by Lopes et al. [19], this trend was not observed for all the delaminations. The shape and through-the-thickness distribution of the delaminations is highly affected by the laminate thickness; reverse pine tree shape is usually developed in thin laminates whereas pine tree shape is observed in thick ones [165].

The issue of the effect of the stacking sequence and/or the mismatch angle on the impact response of laminated composites was addressed in several investigations [19, 36–44]. Some authors [38, 42, 43] concluded that the stacking sequence has insignificant effect on the damage resistance of CFRP composites whereas, others [19, 37, 44] concluded the opposite. Regarding the damage tolerance, the stacking sequence effect is not clear [19]. One of the guidelines obtained from these studies

is to use ± 45 layers on the surface of the laminate to improve the compression after impact resistance [37, 46]. The effect of the mismatch between the orientation of the adjacent layers on the response of laminated composites under low velocity impact and compression after impact is still under debate. Fuoss et al. [39, 40] recommended to avoid small mismatch angles, whereas Clark [45] and Cantwell et al. [46] concluded that small mismatch angles are desirable to improve the damage tolerance.

Most of these studies compared specimens with different interface angles, number of layers/interfaces and in-plane and out-of-plane stiffness. In such cases, the comparison is unfair and inaccurate conclusions can be drawn. An exception of this trend is the study conducted by Lopes et al. [19, 36], where specimens with the same number of layers/interfaces and in-plane and out-of-plane stiffness, were compared. It is worth remarking that without using dispersed laminates, it is impossible to obtain different stacking sequences with the same in-plane and/or out of plane stiffness.

6.3   Material and Specimens

Unlike the former chapters of this thesis, the material used in this study is the AS4D/TC350 carbon/epoxy. The reason for changing the material from AS4/8552 to the current one was the material availability for manufacturing. The manufacturing process was conducted at the Dutch National Aerospace Laboratory-NLR (The Netherlands) using fiber placement technology. The unidirectional material properties were measured according to the corresponding standard procedures. The unidirectional properties are summarized in Table. 6.1.

The baseline (BL) conventional configuration was selected according to the recommendation of the ASTM D7136 [74]. The recommended stacking sequence is $[45/0/-45/90]_{3s}$ resulting of a total thickness of 4.46 mm using the selected material. in this configuration, the mismatch angle between the different plies is 45°.

The dispersed configurations were selected to match within a 15 % of the in-plane and the bending stiffness characteristics of the baseline configuration. To do this, the Ant Colony Optimization (ACO) algorithm, introduced in Chapter 4, was used together with the analytical formulation presented in Chapter 5. The values of the

Table 6.1: AS4D/TC350 unidirectional properties.

Elastic properties	E_{11} = 135.4 GPa; E_{22} = 9.3 GPa; G_{12} = 5.3 GPa; ν_{12} = 0.32
Strength	X^T = 2253.2 MPa; Y^T = 70.4 MPa; Y^C = 307.2 MPa; S^L = 93.0 MPa
Fracture toughness	G_{Ic} = 315.3 J/m^2; G_{IIc} = 1174.3 J/m^2
Thermal expansion	α_1 = 1.16 $\mu\varepsilon$/°C; α_2 = 40.75 $\mu\varepsilon$/°C
Other properties	ρ = 1.6 g/cm^3; t_{Ply} = 0.182 mm; V_f = 60%

mismatch angle between the individual plies were used to formulate the objective function. A similar strategy was used by Lopes et al. [19] using Genetic Algorithms (GAs).

As reported by Christoforou and Yigit [150], the response of FRP under low velocity impact is a function of the equivalent bending stiffness D^*. The value of D^* can be calculated using Eq. (5.6), as a function of the bending stiffness matrix coefficients D_{ij} [145]. The dispersed configurations were designed to have the same value of D^* as the baseline laminate. All the selected configurations were designed to be symmetric and balanced.

Two dispersed stacking sequences were tested. In the first one (NC_01) the mismatch angle was chosen to be in range between 10° and 30° whereas, in the second one (NC_02) the mismatch angle ranged between 55° and 80°. Ply clustering was not allowed to avoid the effect of different number of interfaces [51]. The selected lamination schemes were:

$$\text{NC\_01}: \quad [10/35/65/85/65/35/5/-25/-35/-45/-55/-80]_s$$
$$\text{NC\_02}: \quad [-65/15/90/30/-45/30/-25/55/-10/70/-10/-80]_s$$

The in-plane and out-of-plane stiffness coefficients of the baseline and the two non-conventional dispersed orientations are summarized in Table 6.2.

Table 6.2: Stiffness coefficients of the baseline and the dispersed laminates.

Laminate	E_x GPa	E_y GPa	E_{fx} GPa	E_{fy} GPa	D^* Nm
BL	52.6	52.6	55.2	42.4	400.5
NC_01	50.2	49.8	52.2	39.6	401.4
NC_02	57.7	50.3	48.6	48.3	403.2

6.4 Test Procedure

As recommended by the AITM1-0010 test standard [76], the test specimens were 150 mm in length and 100 mm in width. The specimens were placed over a flat support fixture base with a 125 mm x 75 mm rectangular cut-out which allowed the impactor to contact through the specimen without interferences (see Figure 6.1(a)). Guiding pins were used such that the specimen could be centrally positioned over the cut-out. The support fixture base had four rubber-tipped clamps which restrained the specimen during impact and provided a minimum holding capacity of 1100 N. These rubber-tipped points clamped the specimen at 12.5 mm and 6 mm from each edge of the open window of the fixture base (see Figure 6.1(b)).
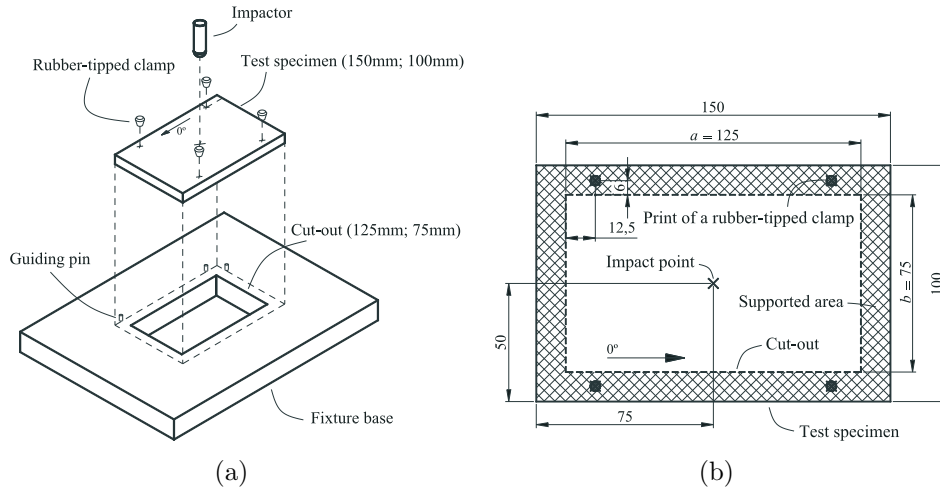

Figure 6.1: Drop-weight impact test configuration and dimensions.

The impacts were performed at different impact energies, as recommended by the AITM-0010 standard [76]. The selected values of the impact energies (E_i), masses (M_i), velocities ($V_0 = \sqrt{2E_i/M_i}$), impact heights ($H_i = E_i/(M_i g)$) and number

of examined specimens are summarized in Table 6.3. The number of specimens tested at 30 J is three as recommended by the test standard [76]. However, for the other impact energies, two specimens were tested instead of one for a better statistical representation. After impact, one specimen per impact energy of each stacking sequence was inspected by means of C-scan to determine the projected delamination area.

Table 6.3: Impact energies, mass, velocities and drop weight heights.

	Impact energy (J)						
	7.5	10	15	20	25	30	40
Impactor mass (kg)	2	2	4	4	4	4	4
Initial velocity (m/s)	2.7	3.2	2.7	3.2	3.5	3.9	4.5
Impact height (cm)	38.2	50.9	38.2	51.0	63.7	76.5	102.0
Number of specimens	2	2	2	2	2	3	2

The Compression After Impact (CAI) tests were performed with the guidelines introduced in the AITM1-0010 [76] and the ASTM D7137-07 [75]. The test setup is shown in Figure 6.2. Two linear displacement sensors were introduced in the setup (one on the impacted face at the impact point and the other on the non-impacted face) to check the out-of-plane displacement at both faces of the plate at the impact point.
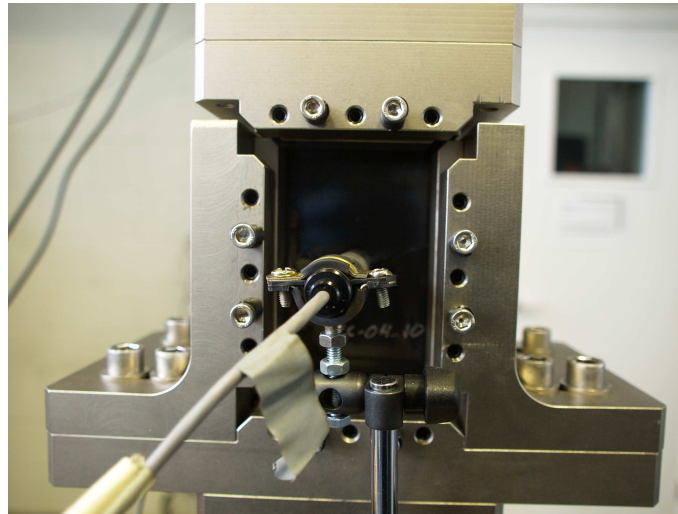

Figure 6.2: Compression after impact test setup and specimen

The compression after impact strength (σ^{CAI}) was calculated based on the ultimate load ($P_{\max}$) and the specimen cross-section dimensions ($\sigma^{CAI} = P_{\max}/b \cdot h$, where b and h were the specimen width and thickness, respectively). In addition to the specimens summarized in Table 6.3, two non-impacted specimens of each stacking sequence were compressed up to failure to determine the non-impacted strength (σ^0). The residual strength can be calculated as the ratio between the CAI strength and the non-impacted specimen strength.

6.5 Results and Discussion

6.5.1 Low velocity impact results

Figure 6.3 shows a comparison between the response of the three stacking sequences at a low value of the impact energy ($E_i = 15$ J) and at a relatively high one ($E_i = 40$ J). The corresponding load-displacement diagrams are shown in Figure 6.4. The peak load and the delamination threshold load (the load level at which a certain number of unstable delaminations appears [51]) are marked by horizonal dashed and solid lines, respectively, in Figure 6.3.
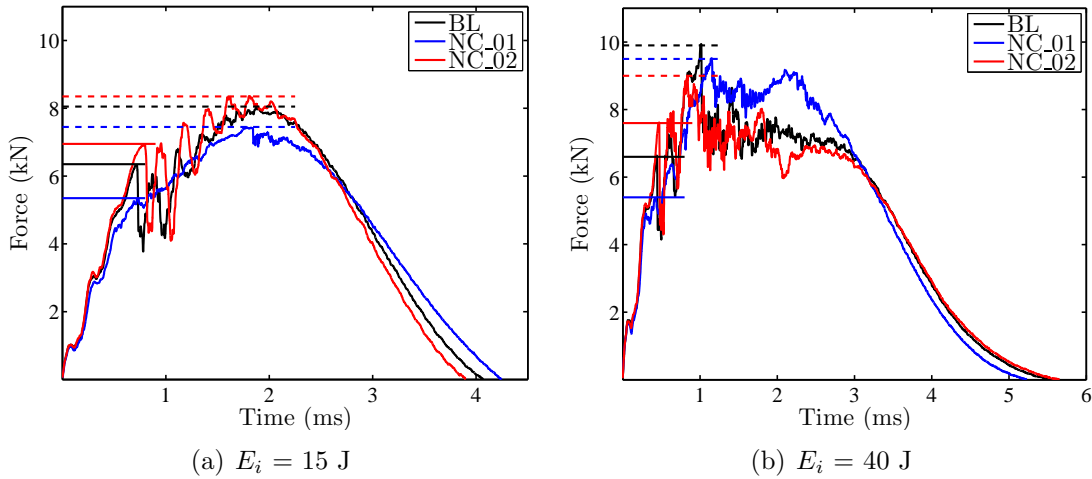

(a) $E_i = 15$ J

(b) $E_i = 40$ J

Figure 6.3: Load-time diagrams for the three configurations (solid horizontal lines represent the delamination threshold and dashed ones represent the peak loads).

The delamination threshold load is one of the features of laminated composites under low velocity loading condition. It is very common to have a large drop in the
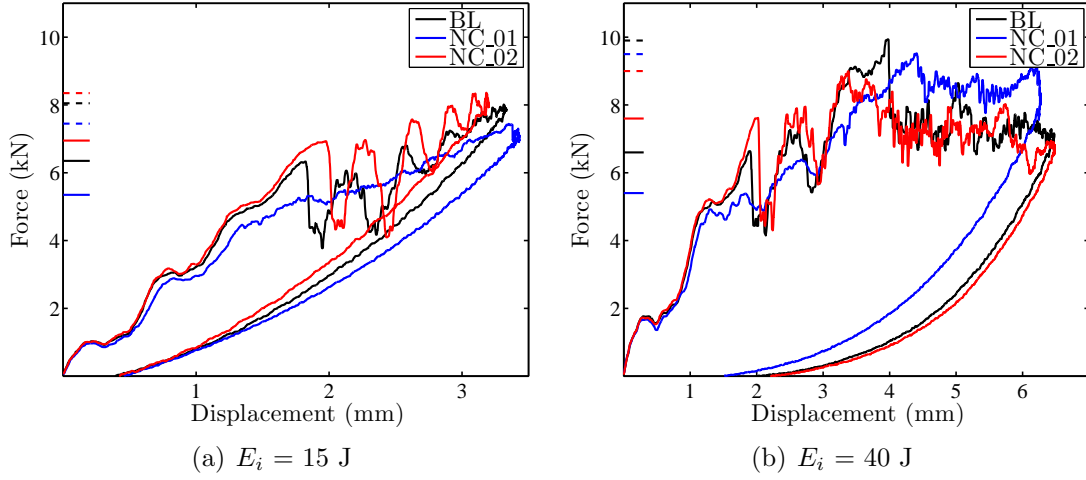
(a) $E_i = 15$ J

(b) $E_i = 40$ J

Figure 6.4: Load-displacement diagrams of the BL, NC_01 and NC_02 configurations (solid horizontal lines represent the delamination threshold and dashed ones represent the peak loads).

contact load at this load level (see for example the results of Petit et al. [17]). In the current experiments, the baseline configuration (BL) and the dispersed configuration with high mismatch angle (NC_02) follow the same trend, with a clear load drop, whereas the dispersed configuration with smaller mismatch angle (NC_01) does not (see Figure 6.3 and 6.4). This phenomenon was observed by González et al. [51] for laminates with a few number of interfaces, i.e. reduced number of expected delaminations. This may be an indication of smaller number of delaminations induced for the NC_01 stacking sequence. Even if the same number of delaminations are obtained, the lake of stiffness-drop, at the threshold load for NC_01, indicates that these delaminations are not initiated at the same time.

As it can be observed in Figure 6.3 and 6.4, the value of the delamination threshold load is independent of the impact energy, as indicated in [51]. From the practical point of view, the most important is to know the energy level at which this phenomenon occurs. The average values of the delamination threshold loads and the corresponding energy levels are summarized in Table 6.4. The effect of the mismatch angle on the threshold is not taken into account in the analytical formulations. According to the analytical formulations (see Chapter 5), this threshold must be the same for the three configurations because the equivalent bending stiffness (D^*) is constant. However, the experimental observations, Table 6.4, shows that

the the delamination thresholds for the NC_01 and NC_02 differ from that for the BL configuration by 19% and 14%, respectively. This is not a small deviation to be analytically ignored.

Table 6.4: The measured delamination threshold and the corresponding impact energies.

Configuration	Delamination threshold kN	Coefficient of variation %	Energy J
BL	6.4	2.4	5.9
NC_01	5.2	1.8	4.8
NC_02	7.3	2.3	7.1

The peak load shows a dependence on both the stacking sequence and the impact energy (see Figure 6.5). At lower impact energies, the dispersed laminate with a high mismatch angle (NC_02) has the highest peak loads whereas, at higher energies, the baseline laminate has the highest. Compared to the variation in the delamination threshold, the effect of the mismatch angle on the peak load is weak.
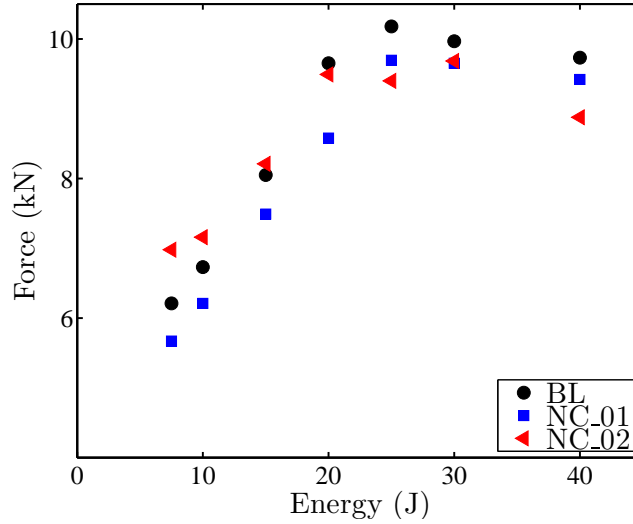

Figure 6.5: Peak load as a function of the impact energy for the BL, NC_01 and NC_02 configurations.

Unlike the peak load, the effect of stacking sequence on the contact time, Figure 6.6, and the total displacement at the contact point, Figure 6.7, is not relevant.

The contact time depends on the in-plane and out-of-plane stiffness, the impactor mass, the impact energy and the damage state. For the same impactor mass, the contact time is linearly dependent on the impact energy, Figure 6.6. Although the displacement is expected to be a function of the total induced damage, and the damage is expected to be a function of the stacking sequence, there is no dependence of the displacement on the mismatch angle. This result is in agreement with the one obtained by Lopes et al. [19]. The total displacement is more dependent on the in-plane and out-of plane stiffness, and impact energy than on stacking sequence.
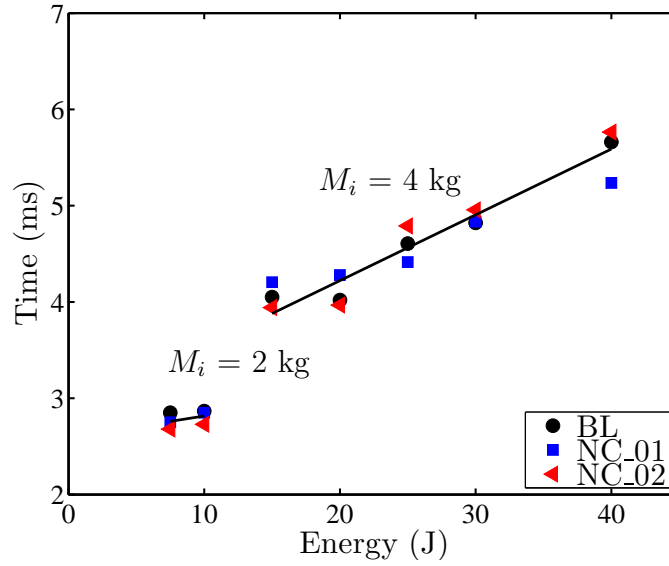

Figure 6.6: Contact time as a function of the impact energy.

The impactor kinetic energy is transferred to the specimen during the event. Part of this energy is transformed into elastic deformation and the other part is absorbed by different failure mechanisms, mainly in the form of delamination [174]. The energy versus time curves are shown in Figure 6.8 for 40 J impact on the three configurations. A slight advantage is given to the dispersed laminate with small mismatch angle (NC_01) because less energy is absorbed in failure and, consequently, more energy is dissipated in elastic deformations. The absorbed energy as a function of the impact energy is shown in Figure 6.9. For energy values up to 20 J there is no dependency of the absorbed energy on the mismatch angle. At higher impact energies, the higher the mismatch angle the higher the absorbed energy. This result indicates that more damage is expected as the mismatch angle increases as found in
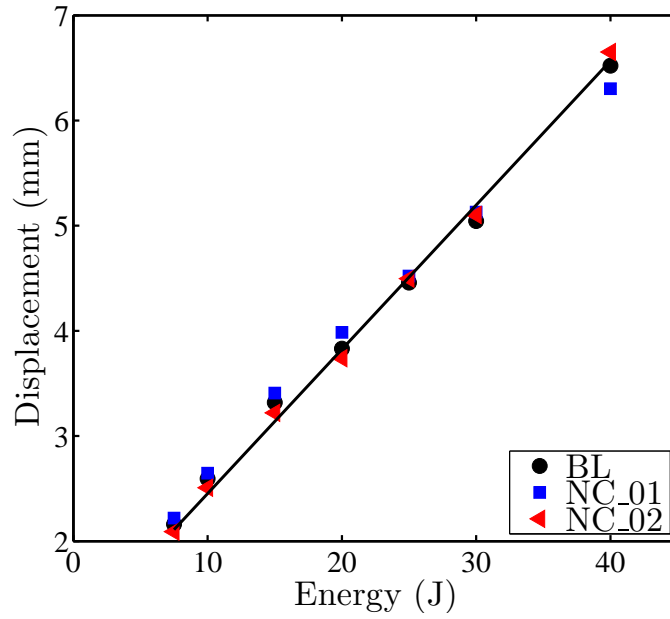
Figure 6.7: Displacement as a function of the impact energy.

[165].
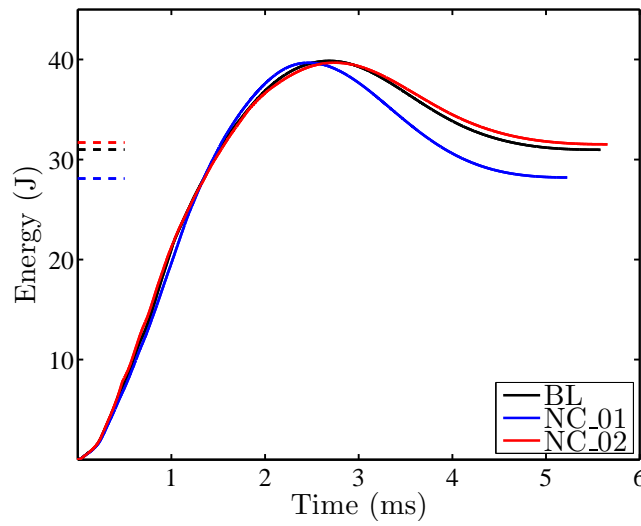
Figure 6.8: The absorbed energy at 40 J impact energy (horizontal lines represent the absorbed energy for each configuration).

The indentation on the impacted specimens, measured immediately after the tests, is plotted against the impact energy in Figure 6.10. For impact energies up to 20 J, the effect of mismatch angle on the indentation is small. At higher energy
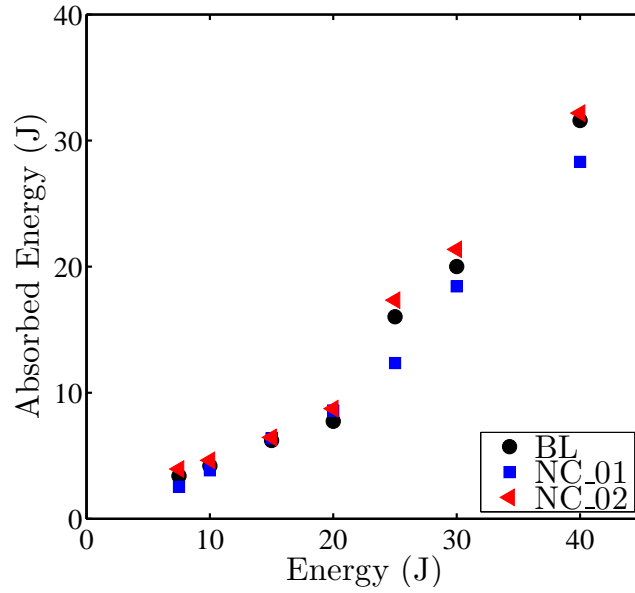
Figure 6.9: Absorbed energy as a function of the impact energy for the three configurations.

values, the higher the mismatch angle, the higher the indentation which indicates a concentration of damage in the material [175, 176], as the mismatch angle increased. This is in agreement with the relatively higher value of the absorbed energy at higher mismatch angles (see Figure 6.9).

Figure 6.10: Indentation as a function of the impact energy.

The ply splitting on the back face (the non-impacted face) reflects the indentation values. Figure 6.11 shows a comparison between the three configurations at 30 J impact energy. The splitting of the back face of the dispersed laminate with small mismatch angle (NC_01) is narrow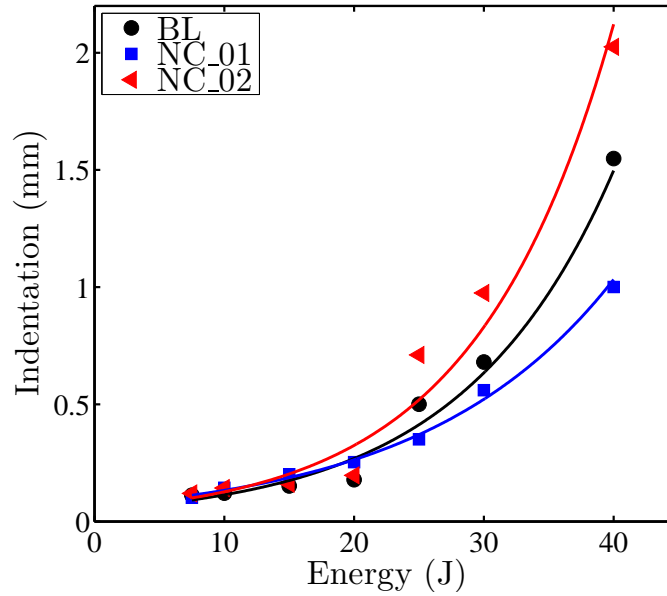 compared to the other stacking sequences. Moreover, some fiber breakage is visually detected in the baseline laminate and also the dispersed laminate with higher mismatch angles. The splitting towards the bottom is mainly because of bending stresses [177].

(a) BL   (b) NC_01   (c) NC_02
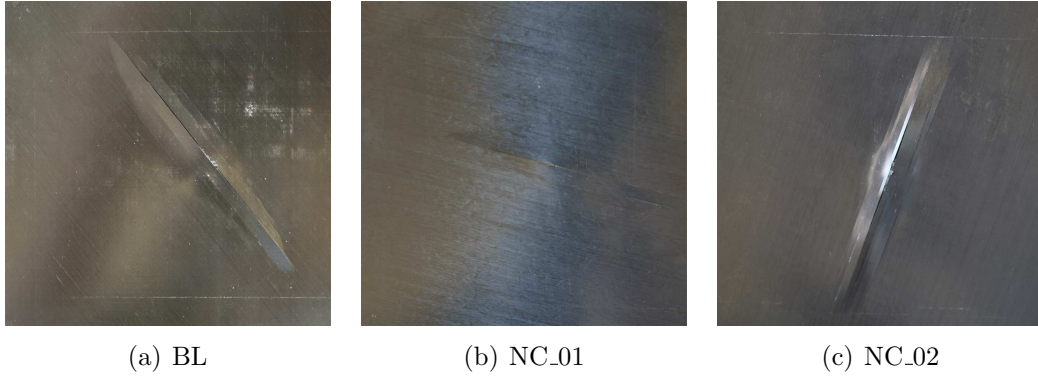
Figure 6.11: Visual inspection of the non-impacted face of the three stacking sequences at 30 J impact energy.

6.5.2   Non-destructive testing

The shapes of the projected delamination areas, resulting from the C-scan ultrasonic technique, are shown in Figure 6.12. These results are summarized in Figure 6.13 by plotting the projected delamination area as a function of the impact energy for the three stacking sequences. As the impact energy increases, delaminations grow in different forms depending on the ply orientations. For the baseline configuration, the projected delamination area is almost circular with a wide delamination at the last interface (the interface between the 0° and 45° layers at the non-impacted face). For the NC_02 case, the same trend is observed with the largest delamination at the bottom surface with a propagation angle of -65° (the same orientation as the back face fiber orientation). For the NC_01 configuration, two wide delaminations are observed: one grows with 35° and the other one is oriented at -55°. In addition to these two wide delaminations, a relatively narrow one is oriented on 10° at the

back face interface. This delamination is triggered by splitting (matrix cracking due to specimen bending) at the back surface.

Figure 6.12: The projected damage shape resulting from C-scans for the three configurations.
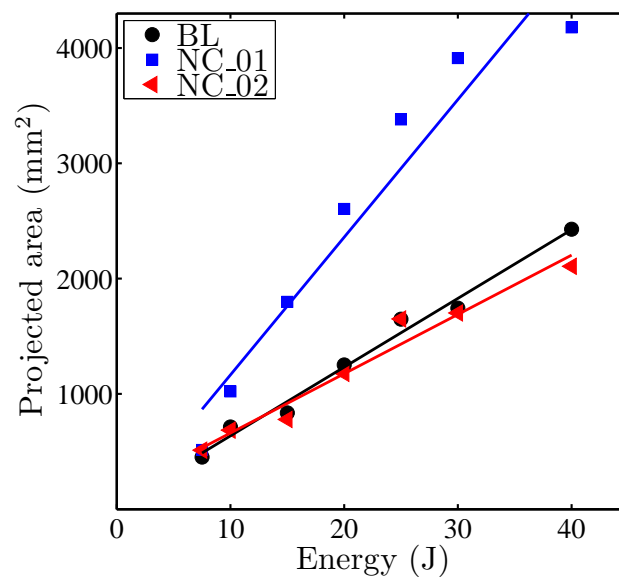
Figure 6.13: Projected damage area as a function of the impact energy.

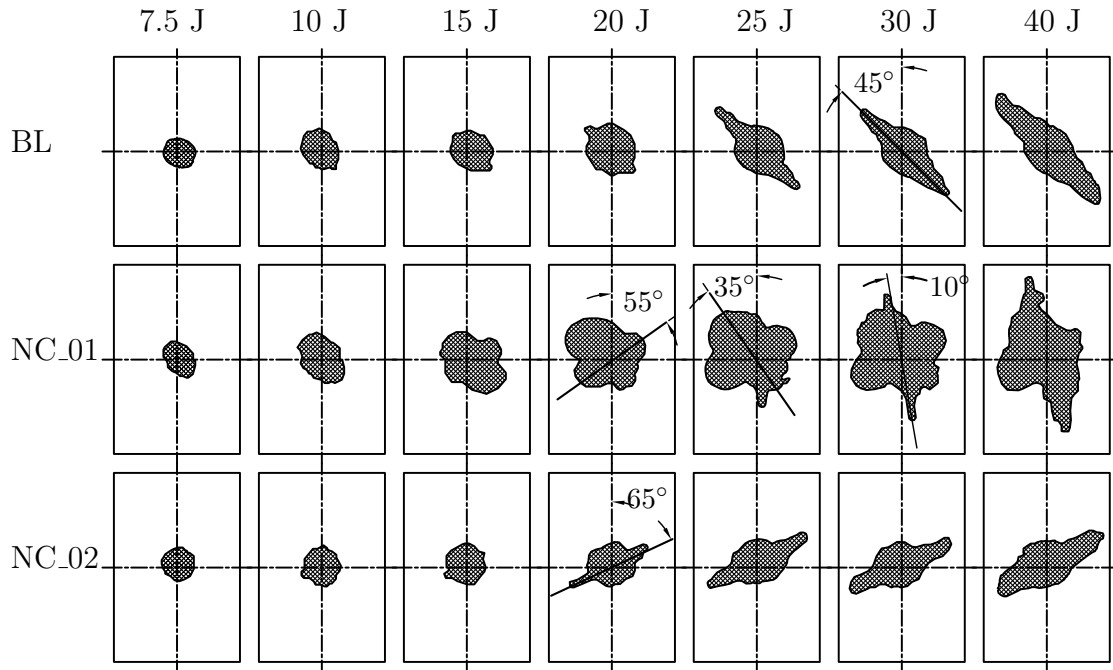The indentation as a function of the projected damage area, Figure 6.14, shows that, at the same value of the projected area, the configuration with higher mismatch angle has greater indentation. For the NC_01 configuration, smaller values of the indentation and larger delamination areas are recognized, compared to the other configurations, at the same energy level. This result indicates that the absorbed energy (which according to Figure 6.9 is relatively lower) is consumed in interlaminar damage rather than in localized matrix cracking and fiber failure around the impact region.
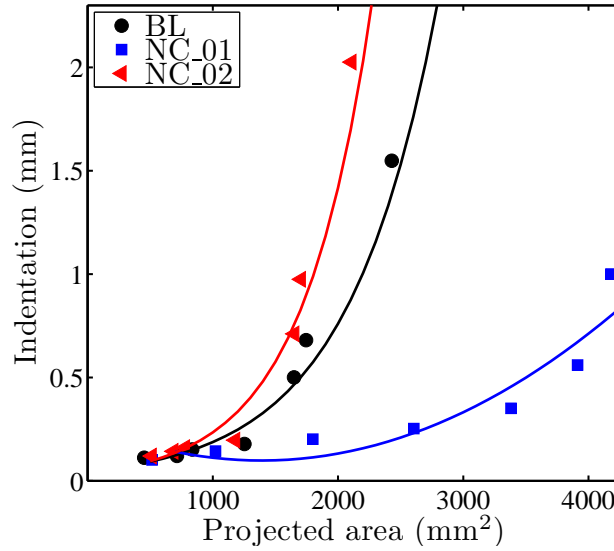
Figure 6.14: Indentation as a function of the projected damage area

The through-the-thickness position of individual delaminations can be seen in Figure 6.15 for the configurations BL and NC_01 at 20 J impact energy. For the baseline configuration (see Figure 6.15(a)), delaminations are observed in all the interfaces starting from interface number 5 to the interface number 11 (the interface just before the midplane). Below the midplane, some delaminations can be observed whereas in others not, due to the relative position and size of different delaminations. Ply splitting, due to bending, is also observed at the last interface. Except for the back face splitting, delaminations at different interfaces have almost the same peanut shape and size. This is the reason for the circular projected area in Figure 6.12. It is worth remarking that the through-the-thickness shape of individual delaminations of the configuration NC_02 is more similar to the the BL more than the NC_01.
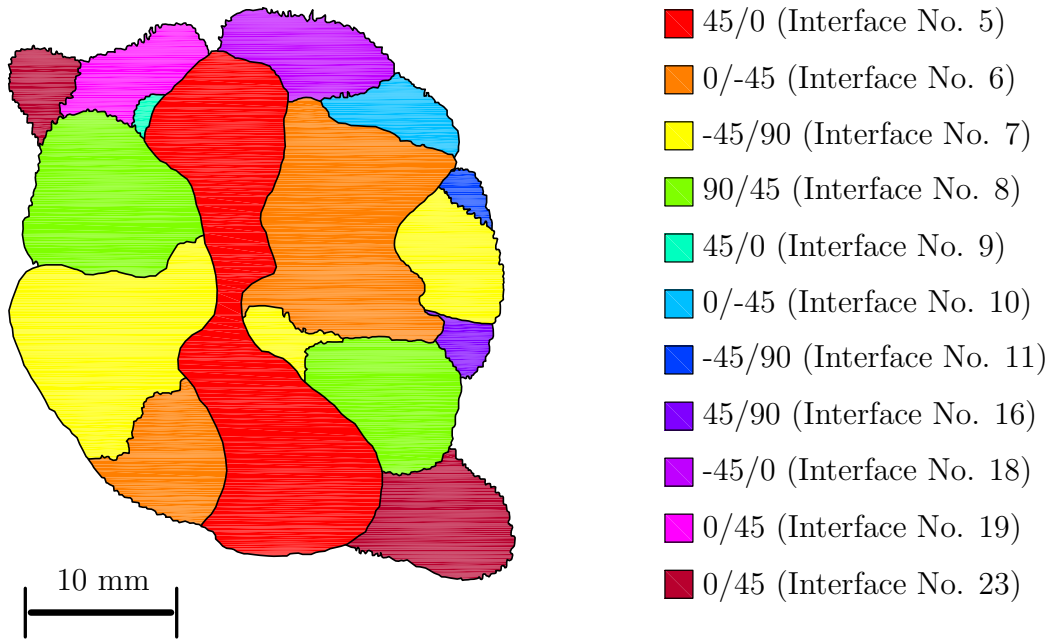
(a) BL ($\Delta\theta = 45°$)
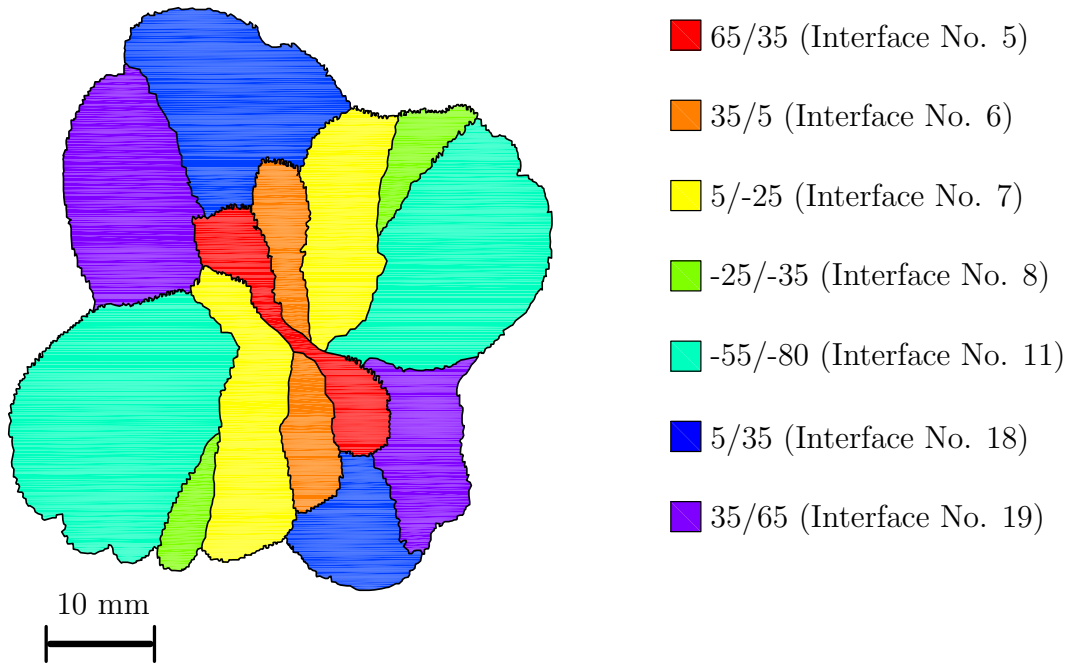
(b) NC_01 ($5° \leq \Delta\theta \leq 30°$)

Figure 6.15: Through-the-thickness position of individual delaminations.

The response is completely different in the case of the NC_01 stacking sequence, Figure 6.15(b). Relatively smaller delaminations are identified at the interfaces 5, 6, 7 and 8, whereas at the interfaces 9 and 10 no delaminations are observed. Interfaces 9 and 10 have a mismatch angle of 10°. Delaminations in these interfaces can not be detected either because they are covered by the other delaminations (at interface 5, 6, 7 and 8) or simply because they do not exist. Even by assuming that these delaminations exists, the fact that they are covered means that they are very small compared to the other ones. In either cases these layers with small mismatch angle act as cluster of plies.

The comparison between the three stacking sequences, based on the projected damage area (see Figure 6.13), shows the advantage of the dispersed configuration with higher mismatch angle (NC_02). This conclusion seems to contradict the results obtained from the absorbed energy (Figure 6.9), the indentation (Figure 6.10) and the through-the-thickness position of the individual delamination (Figure 6.15). A possible explanation for this is that in the configuration NC_01 a smaller number of delaminations exist. Thus, a smaller amount of energy is absorbed in fewer but wider delaminations. For the BL and the NC_02 configurations, a higher number of delaminations are propagated, require more absorbed energy and produce relatively narrow delaminations.

Following this discussion, the advantage of one stacking sequence over the other can not be judged based on the projected delamination area alone because in one configuration (NC_01) there is a few number of wide delaminations, whereas in the others (BL and NC_02) there are many and relatively narrow ones.

6.5.3 Compression after impact results

The results obtained from the linear displacement sensors show that the buckling mode for the three configurations is the same, independently of the mismatch angle or the impact energy. As an example, Figure 6.16 shows the result obtained for the configuration NC_02 impacted at 30 J. Throughout the loading history, two buckling modes are recognized at the impact point. Up to the maximum compression load, the displacement of the surfaces (both the impacted and the non-impacted faces) are in the direction of the impact displacement. This is an expected behavior due to the permanent indentation observed after impact [33]. Suddenly after the maximum

load, the delamination buckling occurs for both sides of the lateral surfaces.
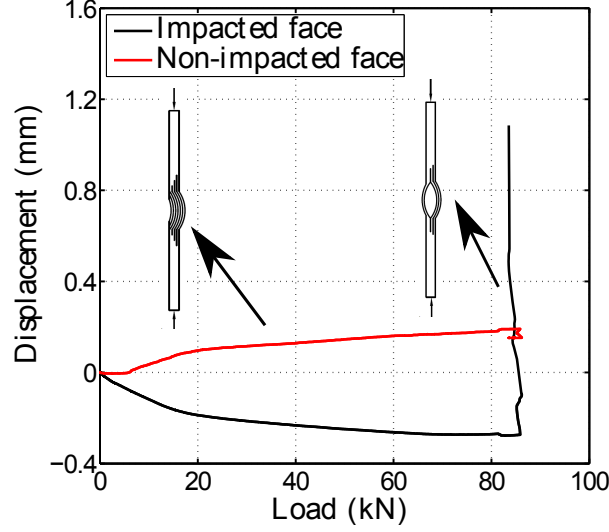
Figure 6.16: Example of the buckling mode obtained using the linear displacement center.

The compression after impact strength σ^{CAI} can be shown in Figure 6.17, whereas the the normalized values is shown in Figure 6.18 for the three configurations. The values of σ^0 are 431.6 MPa, 352.6 MPa and 428.5 MPa for the configurations BL, NC_01 and NC_02, respectively. It is worth remarking that the maximum value of the coefficient of variation is 10 %. The results show the advantage of the non-conventional dispersed laminates over the conventional ones with respect to the dimensional CAI strength. Compared to the baseline, using the dispersed laminates with small mismatch angle improves the CAI strength for all the impact energies under consideration. The improvement ranges from 4.7 % (at the 7.5 J impact energy) to 30.7 % (at 20 J impact energy). Up to 10 J impact energy, the CAI strength of the NC_02 is lower than its value of the BL configuration. For higher impact energies, the CAI strength of NC_02 is higher than the baseline.

A more religious conclusion can be obtained from the normalized strength versus energy plots. As can be shown in Figure 6.18, the residual strength of the dispersed laminates with small mismatch angle (NC_01) is higher than it for the other two configurations. With a 7.5 J impact, the configuration NC_01 does not lose any of its initial strength, whereas the reductions are 21 % and 30 % respectively for the BL and NC_02 configurations. At 20 J impact energy, the configurations BL and NC_02

Figure 6.17: Residual strength as a function of the impact energy for the three configurations.

Figure 6.18: Percentage of residual strength as a function of the impact energy.

lose about 50 % of their initial strength whereas the configuration NC_01 loses only 25 %. This result highly supports the laminate with small mismatch angle over the

ones with high mismatch angles or conventional stacking sequence.

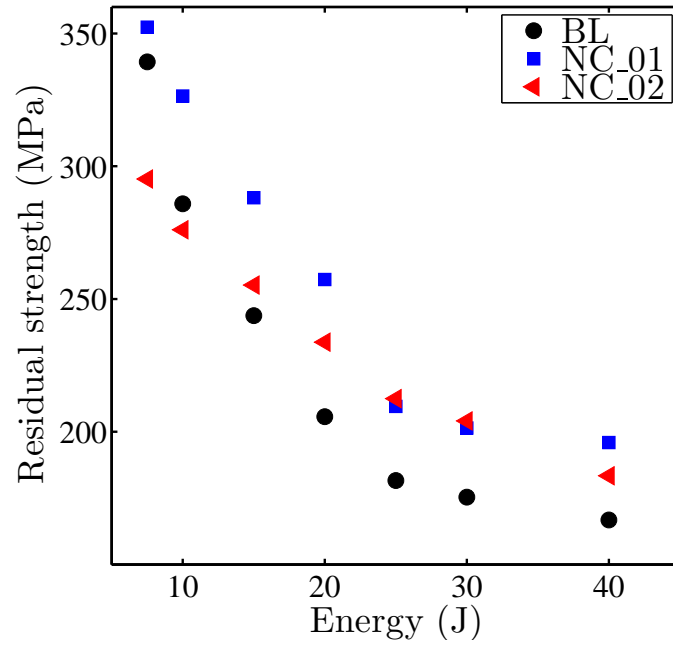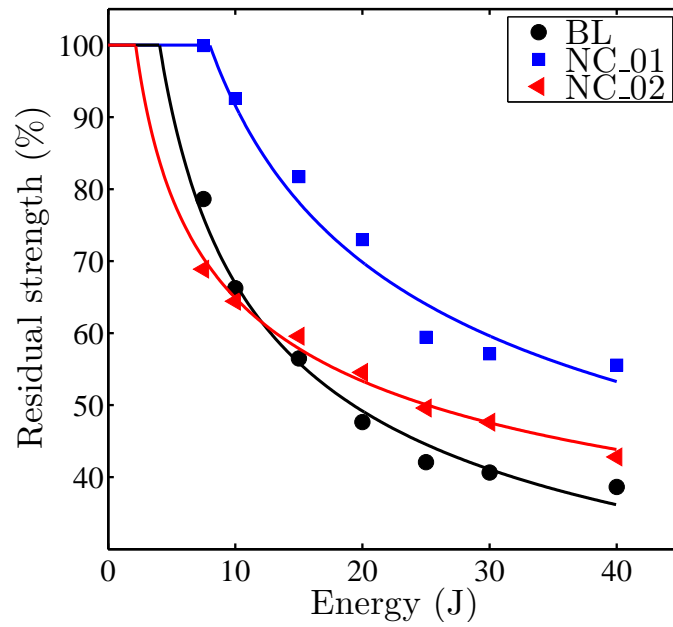It is well known that composites containing one or more delaminations can buckle at a lower level of compressive load and this level depends on the number, size, the through-the-thickness position and shape of the delaminations in the laminated composite materials [178, 179]. The reason behind the improvement obtained for the NC_01 laminate in the compression after impact strength is the smaller number of delaminations. Unlike the other configurations, the NC_01 laminate is divided into smaller number of thick sublaminates during the impact event. The greater thickness of the sublaminates, in the case of small mismatch angle configuration, increase its buckling load and consequently increase its residual strength.

6.6   Conclusions

In this chapter, the effect of the mismatch angle between the adjacent plies was studied. Low velocity impact and compression after impact tests were conducted on one conventional laminate and compared with two dispersed ones. The mismatch angle of the first dispersed laminate ranged from 10° to 30°, whereas for the second one it ranged from 55° to 80°. The ACO algorithm, summarized in Chapter 4, was used with the low velocity impact analytical formulations, introduced in Chapter 5, to define the two dispersed configurations. The mismatch angle of the conventional laminate was 45°.

The results showed the usefulness of the dispersed laminates. By reducing the mismatch angle between the adjacent layers while keeping constant the in-plane and the out-of-plane stiffness characteristics, the response of CFRP composites to low velocity impact and compression after impact events could be improved. The improvement resulted in smaller permanent indentation, less energy absorbed by the different damage mechanisms, smaller number of delaminations (although they are wider at some interfaces) and higher residual compressive strength.

It can be concluded that adjacent plies with small mismatch angle behave as a sublaminate after low velocity impact. This phenomenon could be observed for the mismatch angles of 10°. This was the main reason for the improvement in the residual strength of the dispersed laminate with a small mismatch angle.

Conclusions and Future Work

Chapter 7

General Conclusions and Future Work

7.1 Main Conclusions

The thesis considerers two main subjects: delamination in multidirectional laminates and optimization of laminated composites for improved damage resistance and damage tolerance. The main objective of this work was to optimize and compare the response of non-conventional dispersed laminates with that of the conventional ones. This objective is clear in the second part of the thesis. It is well known in the field of laminated composites that the failure response of any composite part highly depends on the onset and propagation of different failure mechanisms. Delamination, as one of the most important failure mechanisms, is addressed in the first part of this thesis. The results obtained in Part I can be considered as a step forward to enable the full characterization of fracture toughness in multidirectional laminates. This characterization, when performed, can help to understand how the dispersed laminates behave under different loading conditions.

7.1.1 Delamination in multidirectional laminates

In the first part of this thesis, the delamination phenomenon in multidirectional laminates was studied by numerical and experimental means to allow the design of a stacking sequence able to avoid crack jumping when being loaded under mode

I. The simulations adopted the cohesive law to simulate both interlaminar damage however, the intralaminar one are checked using the LaRC04 failure criteria during crack propagation. The delamination tests were conducted at ambient conditions according to the ISO 15024 [72] standard. From this study, the following conclusion can be drawn:

- The effect of including a thermal step, to simulate the curing process, on the load-displacement curve and the predicted failure index of DCB specimens, was investigated. The results showed that including thermal step did not affect the expected load versus displacement curves. However, these thermal effects modify the prediction of the tensile matrix cracking failure index and tend to promote migration of the interlaminar crack plane.

- A set of stacking sequences, ranging from very flexible to very stiff was numerically analyzed to check the possible effect of the crack beam bending stiffness on the possibility of matrix cracking. The results showed that the higher the bending stiffness of the specimen arms, the lower the failure index is and, as a consequence, the lower is the tendency to crack jumping. The stacking sequence $[(\pm\theta_1/0_8)_s//(\pm\theta_2/0_8)_s]$ may be used to avoid the crack jumping problem for the examined interfaces.

- Regarding the crack front shape, a new parameter (λ_v) was used to define the relative position of the crack using its position at the specimen edge and at the crack front mean line. The results show that there is no clear dependency of λ_v upon the bending stiffness, the mismatch angle or the incline angle. The deviation ranges from 1.18 mm to 2.46 mm. Since this range is small, a common average value can be added to the measured crack length, during the propagation tests as a correction for the crack front shape.

- The experimental results were in agreement with the numerical ones, i.e. the higher the value of the bending stiffness of the crack beam arm, the lower the tendency to crack jumping. The fracture toughness values were more affected by the fiber bridging than by the mismatch angles between the layers interfacing the crack plane.

- The crack path, obtained by optical microscope images, showed that in most of the cases the delaminations do not exactly develop at interfaces. Instead, fiber tearing is the more common damage mode along the crack propagation path. Consequently, the measured fracture toughness depends more on the angle between the crack growth direction and the ply orientation in which the crack propagates than on the mismatch angles of the plies adjacent to the interface. However, further investigation should be carried out to support this idea.

7.1.2 Damage resistance and damage tolerance of dispersed laminates

The second part of this thesis started by selecting the Ant Colony algorithm to optimize the stacking sequence of laminated composite parts subjected to different loading conditions. The loading conditions considered were biaxial tension and compression, and low velocity impact. The results of the analytically-based optimizations showed that the effect of the mismatch angle was not included in the formulations. To investigate the mismatch angle effect, three stacking sequences were defined with nearly the same stiffness response but with different mismatch angles. They were then subjected to low velocity impact and compression after impact with the procedure summarized in [76]. The following conclusions can be drawn from this work:

- The Ant Colony algorithm was tested and compared with the Genetic Algorithms through the data published in [114]. The comparison showed that both algorithms converge to the same optimum solutions however, the normalized price data gave more advantage to the Ant Colony algorithm.

- An optimization study was conducted to check the validity of using a simple failure criteria (for example the maximum strain criterion or the Tsai-Wu criterion) instead of the physically-based failure criteria that usually require higher computational time. The results showed that the use of the maximum strain criterion usually leads to local optima while the Tsai-Wu leads to out-of-feasible region solutions as compared to the physically-base LaRC03 failure

criteria. The conclusion of that study was the decision to use the LaRC03 failure criteria in spite of its associated computational time given the reliability of the results.

- Under several loading conditions, the dispersed laminates showed superior characteristics, compared to the conventional laminates. For a plates under compression, the improvement in the critical buckling load ranged from 2.5% to 8% for the different load ratios. In the case of low velocity and large mass impact loading, the predicted damage area of the dispersed laminate was 21% smaller than for the conventional one. These improvements are obtained due to the higher freedom given to the algorithm when selecting the stacking sequences. These improvements showed the capability of the dispersed laminates to transfer loadings from the weak transverse direction to the strong longitudinal one.

- The behavior of three laminates, with different mismatch angle, under low velocity and large mass impact loading was experimentally investigated. The results showed that, by reducing the mismatch angle between the adjacent layers while keeping constant the in-plane and the out-of-plane stiffness characteristics, the response of CFRP composites to low velocity impact and compression after impact could be improved. The improvement resulted in less indentations, less energy absorbed by the different damage mechanisms, smaller number of delaminations (although wider at some interfaces) and higher residual compressive strength. This improvement was obtained because the plies with small mismatch angle ($\Delta\theta = 10°$) behave as a cluster, i.e. no delaminations appeared between plies with a mismatch angle up to $10°$.

7.2   Future Work

The following topics are suggested for possible developements:

- The full characterization of the fracture toughness in mode I and II, as a function of the mismatch angle and crack propagation direction, can help to understand more about the fracture behavior of the dispersed laminates. Moreover, the effect of test speed is also a key issue because in low velocity

impact the delamination propagation speed is very high compared to the one used in the standard testing. This change in the speed can completely change the behavior.

- Although it is not considered in the thesis, analyzing the mismatch angle effect on the in-situ tensile, compression and shear strength can help to understand the delamination onset. According to an available physically-based model [92], the mismatch angle has no effect. However, some experimental studies [180, 181] showed that the mismatch angle highly affects the in-situ strength.

- With the same procedure adopted in the Chapter 6, a test matrix can be defined to check the effect of ply clustering at the same in-plane and out-of-plane stiffness. Optimizing a dispersed laminate with stiffness constraints and one or more cluster, oriented along the CAI loading direction, can highly increase the residual strength. Moreover, the position of the individual cluster can be of interest.

- Numerically, optimizing the buckling load of sublaminates with respect to its through-the-thickness position with different size can help to define the best position to introduce plies with small mismatch angles or even plies with the same orientation to increase the residual compression strength.

Bibliography

[1] S. K. Garg, V. Svalbonas, and G. A. Gurtman. *Analysis of structural composite materials*. Marcel Dekker, Inc., New York, USA, 1973.

[2] R. M. Jones. *Mechanics of composite materials*. Tailor & Francis, Philadelphia, PA, USA, second edition, 1999.

[3] J. R. Vinson and T. Chou. *Composite materials and their use in structures*. Applied Science Publishers, London, UK, 1975.

[4] S. T. Peters. *Handbook of composites*. Chapman & Hall, London, UK, second edition, 1998.

[5] J. N. Reddy. *Mechanics of laminated composite plates and shells, theory and analysis*. Chapman & Hall, London, UK, second edition, 1998.

[6] S. K. Mazumdar. *Composites manufacturing, materials, product and process engineering*. CRC Press LLC, Florida, USA, 2002.

[7] J. Bold. Airbus composite training. In *Proceedings of Visual Product Development (VPD) Conference, Frankfurt, Germany*, October 2007.

[8] J. Hale. Boeing 787 from the ground up. *AERO magazine*, 24:17–23, 2006.

[9] A. Baker, S. Dutton, and D. Kelly. *Composite materials for aircraft structures*. American Institute of Aeronautics and Astronautics AIAA Inc., Roston, VA, USA, 2nd edition, 2004.

[10] S. W. Beckwith. Filament winding vs. fiber placement manufacturing technologies. *SAMPE Journal*, 44:54–55, 2008.

[11] R. D. Hale and V. M. Vasey-Glandon. Fiber placement and fiber steering systems and corresponding software for composite structures. Technical Report US006799081B1, United States Patent, 2004.

[12] J. R. Barth. Fabrication of complex composite structures using advanced fiber placement technology. In *35th International SAMPE Symposium*, pages 710–720, Anaheim, CA, USA, 1990.

[13] F. Bullock, S. Kowalski, and R. Young. Automated prepreg tow-placement for composite structures. In *35th International SAMPE Symposium*, pages 734–743, Anaheim, CA, USA, 1990.

[14] Verlag moderne industrie GmbH. CFRP: What's holding up automation?, 2012. URL `http://www.aerotec-online.com/en/cfrp-whats-holding-up-automation`.

[15] Coriolis Composites. The use of robots for fiber placement, 2008. URL `http://www.coriolis-composites.com/technologie.php`.

[16] M. J. Pasanen, J. P. Martin, R. J. Langone, and J. A. Mondo. Advanced composite fiber placement: Process to application. Technical report, Automated Dynamics Corporation, 1997.

[17] S. Petit, C. Bouvet, A. Bergerot, and J. J. Barrau. Impact and compression after impact experimental study of a composite laminate with a cork thermal shield. *Composite Science and Technology*, 67:3286–3299, 2007.

[18] C. S. Lopes. *Damage and failure of non-conventional composite laminates.* PhD thesis, Delft University of Technology, 2009.

[19] C. S. Lopes, O. Seresta, Y. Coquet, Z. Gürdal, P. P. Camanho, and B. Thuis. Low-velocity impact damage on dispersed stacking sequence laminates. Part I: Experiments. *Composites Science and Technology*, 69:926–936, 2009.

[20] Rahul, D. Chakraborty, and A. Dutta. Optimization of FRP composites against impact induced failure using island model parallel genetic algorithm. *Composites Science and Technology*, 65:2003–2013, 2005.

[21] Rahul, G. Sandeep, D. Chakraborty, and A. Dutta. Multi-objective optimization of hybrid laminates subjected to transverse impact. *Composite Structures*, 73:360–369, 2006.

[22] M. W. Hyer and R. F. Charette. Use of curvilinear fiber format in composite structure design. In *30th structures, structural dynamics, and material conference*, pages 1011–1015, Mobile, AL, USA, 1989.

[23] Z. Gürdal and R. Olmedo. In-plane response of laminates with spatially varying fibre orientations: Variable stiffness concept. *AIAA Journal*, 31:751–758, 1993.

[24] M. M. Abdalla, S. Setoodeh, and Z. Gürdal. Design of variable stiffness composite panels for maximum fundamental frequency using lamination parameters. *Composite Structures*, 81:283–291, 2007.

[25] C. S. Lopes, Z. Gürdal, and P. P. Camanho. Variable-stiffness composite panels: Buckling and first-ply failure improvements over straight-fibre laminates. *Computers and Structures*, 86:897–907, 2008.

[26] S. Setoodeh, M. M. Abdalla, S. T. IJsselmuiden, and Z. Gürdal. Design of variable-stiffness composite panels for maximum buckling load. *Composite Structures*, 87:109–117, 2009.

[27] Advanced Design and Inc. Optimization Technologies. Consulting services, 2002. URL `http://www.adoptech.com/Consulting_Services/consulting_services.htm`.

[28] H. Ghiasi, K. Fayazbakhsh, D. Pasini, and L. Lessard. Optimum stacking sequence design of composite materials Part II: Variable stiffness design. *Composite Structures*, 93:1–13, 2010.

[29] G. Goranson. Damage tolerance facts and fiction. In *Proceedings of the International Conference on Damage Tolerance of Aircraft Structures*, TU Delft, Netherlands, September 2007.

[30] M. R. Woodward and R. Stover. Damage tolerance. In D. B. Miracle and S. L. Donaldson, editors, *Composites*, volume 21 of *ASM Handbook*. ASM International, Materials Park, OH, USA, 2001.

[31] E. A. Abdallah, C. Bouvet, S. Rivallant, B. Broll, and J. J. Barrau. Experimental analysis of damage creation and permanent indentation on highly oriented plates. *Composites Science and Technology*, 69:1238–1245, 2009.

[32] D. Roach. Damage tolerance assessment of bonded composite doubler repairs for commercial aircraft applications. In A. A. Baker, L. R. F. Rose, and R. Jones, editors, *Advances in the bonded composite repairs of metallic aircraft structure*, volume 1, chapter 17, pages 485–516. Elsevier Science Ltd, Houston, TX, 2002.

[33] L. Reis and M. de Freitas. Damage growth analysis of low velocity impacted composite panels. *Composite Structures*, 38:509–515, 1997.

[34] H. Razi and S. Ward. Principles for achieving damage tolerant primary composite aircraft structures. In *11th DoD/FAA/NASA Conference On Fibrous Composites in Structural Design*, Fort Worth, TX, USA, December 1996.

[35] M. Thomas. How damage tolerance issues on spacecraft composite structures can take advantage of experience gained through aircraft programmes. In *European Conference on Spacecrafts Structures, Materials and Mechanical Testing*, Toulouse, France, December 2002.

[36] C. S. Lopes, P. P. Camanho, Z. Gürdal, P. Maimí, and E. V. González. Low-velocity impact damage on dispersed stacking sequence laminates. Part II: Numerical simulations. *Composites Science and Technology*, 69:937–947, 2009.

[37] S. A. Hitchen and R. M. J. Kemp. The effect of stacking sequence on impact damage in a carbon fibre/epoxy composite. *Composites*, 26:207–214, 1995.

[38] C. Soutis and P. T. Curtis. Prediction of the post-impact compressive strength of CFRP laminated composites. *Composites Science and Technology*, 56:677–684, 1996.

[39] E. Fuoss, P. V. Straznicky, and C. Poon. Effects of stacking sequence on the impact resistance laminates - Part 1: parametric study. *Composite Structures*, 41:67–77, 1998.

[40] E. Fuoss, P. V. Straznicky, and C. Poon. Effects of stacking sequence on the impact resistance laminates - Part 2: prediction method. *Composite Structures*, 41:177–186, 1998.

[41] H. P. Cui, W. D. Wen, and H. T. Cui. An integrated method for predicting damage and residual tensile strength of composite laminates under low velocity impact. *Computer & Structures*, 87:456–466, 2009.

[42] J. Morton and E. W. Godwin. Impact response of tough carbon fibre composites. *Composite Structures*, 13:1–19, 1989.

[43] C. K. L. Davies, S. Turner, and K. H. Williamson. Flexed plate impact testing of carbon fibre-reinforced polymer composites. *Composites*, 16:279–285, 1985.

[44] M. V. Hosur, C. R. L. Murthy, T. S. Ramamurthy, and A. Shet. Estimation of impact-induced damage in cfrp laminates through ultrasonic imaging. *NDT&E International*, 31:359–374, 1998.

[45] G. Clark. Modeling of impact damage in composite laminates. *Composites*, 20:209–214, 1989.

[46] W. J. Cantwell and J. Morton. The impact resistance of composite materials - a review. *Composites*, 22:347–362, 1991.

[47] T. W. Shyr and Y. H. Pan. Impact resistance and damage characteristics of composite laminates. *Composite Structures*, 62:193–203, 2003.

[48] S. V. Potti and C. T. Sun. Prediction of impact induced penetration and delamination in thick composite laminates. *International Journal of Impact Engineering*, 19:31–48, 1997.

[49] R. Olsson. Analytical prediction of large mass impact damage in composite laminates. *Composites: Part A*, 32:1207–1215, 2001.

[50] G. A. O. Davies, X. Zhang, G. Zhou, and S. Watson. Numerical modeling of impact damage. *Composites*, 25:342–350, 1994.

[51] E. V. González, P. Maimí, P. P. Camanho, C. S. Lopes, and N. Blanco. Effect of ply clustering in laminated composite plates under low-velocity impact loading. *Composites Science and Technology*, 71:805–817, 2011.

[52] J. Andersons and M. König. Dependence of fracture toughness of composite laminates on interface ply orientations and delamination growth direction. *Composites Science and Technology*, 64:2139–2152, 2004.

[53] B. W. Kim and A. H. Mayer. Influence of fiber direction and mixed-mode ratio on delamination fracture toughness of carbon/epoxy laminates. *Composites Science and Technology*, 63:695–713, 2003.

[54] A. B. de Morais, M. F. de Moura, A. T. Marques, and P. T. de Castro. Mode-I interlaminar fracture of carbon/epoxy cross-ply composites. *Composites Science and Technology*, 62:679–686, 2002.

[55] A. J. Brunner, B. R. K. Blackman, and P. Davies. A status report on delamination resistance testing of polymer matrix composites. *Engineering Fracture Mechanics*, 75:2779–2794, 2008.

[56] E. S. Greenhalgh. *Failure analysis and fractography of polymer composites.* Woodhead Publishing Limited, Cambridge, UK, 2009.

[57] N. S. Choi, A. J. Kinloch, and J. G. Williams. Delamination fracture of multidirectional carbon-fiber/epoxy composites under mode I, mode II and mode I/II loading. *Journal of Composite Materials*, 33:73–100, 1999.

[58] D. L. Hunston and W. D. Bascom. Effects of lay-up, temperature and loading rate in double cantilever beam tests of interlaminar crack growth. *Composites Technology Review*, 5:118–119, 1982.

[59] P. Naghipour, M. Bartsch, L. Chernova, J. Hausmann, and H. Voggenreiter. Effect of fiber angle orientation and stacking sequence on mixed mode fracture toughness of carbon fiber reinforced plastics: Numerical and experimental investigations. *Materials Science and Engineering A*, 527:509–517, 2010.

[60] A. A. Benyahia, A. Laksimi, N. Ouali, and Z. Azari. Mechanical behavior and optimization of multidirectional laminate specimens under delamination by bending. *Strength of Materials*, 38:613–623, 2006.

[61] A. Laksimi, M. L. Benzeggagh, G. Jing, M. Hecini, and J. M. Roelandt. Mode I interlaminar fracture of symmetrical cross-ply composites. *Composites Science and Technology*, 41:147–164, 1991.

[62] I. Chou, I. Kimpara, K. Kageyama, and I. Ohsawa. Effect of fiber orientation on the mode I interlaminar fracture behavior of CF/ epoxy laminates. *Journal of the Society of Materials Science*, 41:1292–1298, 1992.

[63] A. Laksimi, A. A. Benyahia, M. L. Benzeggagh, and X. L. Gong. Initiation and bifurcation mechanisms of cracks in multi-directional laminates. *Composites Science and Technology*, 60:597–604, 2000.

[64] A. B. Pereira and A. B. de Morais. Mode I interlaminar fracture of carbon/epoxy multidirectional laminates. *Composites Science and Technology*, 64:2261–2270, 2004.

[65] K. Trakas and M. T. Kortschot. The relationship between critical strain energy release rate and fracture mode in multidirectional carbon fiber/epoxy laminates. *ASTM STP*, 1285:283–304, 1997.

[66] P. Robinson and D. Q. Song. A modified DCB specimen for mode I testing of multidirectional laminates. *Journal of Composite Materials*, 26:1554–1577, 1992.

[67] J. J. Polaha, B. D. Davidson, R. C. Hudson, and A. Pieracci. Effects of mode ratio, ply orientation and precracking on the delamination toughness of a laminated composite. *Journal of Reinforced Plastics and Composites*, 15: 141–173, 1996.

[68] A. Turon, P. P. Camanho, J. Cost, and C. G. Dávila. An interface damage model for the simulation of delamination under variable-mode ratio in composite materials. Technical Report NASA/TM-2004-213277, NASA, Langley, Research Center, Hampton, 2004.

[69] A. Turon, P. P. Camanho, J. Costa, and C. G. Dávila. A damage model for the simulation of delamination in advanced composites under variable mode loading. *Mechanics of Materials*, 38:1072–1089, 2006.

[70] A. Turon, C. G. Dávila, P. P. Camanho, and J. Costa. An engineering solution for mesh size effects in the simulation of delamination using cohesive zone models. *Engineering Fracture Mechanics*, 74:1665–1682, 2007.

[71] S. T. Pinho, C. G. Dávila, P. P. Camanho, L. Iannucci, and P. Robinson. Failure models and criteria for FRP under in-plane or three-dimensional stress states including shear non-linearity. Technical Report NASA/TM-2005-213530, NASA, Langley, Research Center, Hampton, February 2005.

[72] ISO-15024. Fiber-reinforced plastic composites-Delamination of mode I interlaminar fracture toughness, G_{Ic}, for unidirectional reinforced materials. ISO Standard, International Organization for Standardization, Geneva, Switzerland, 2001.

[73] H. Ghiasi, D. Pasini, and L. Lessard. Optimum stacking sequence design of composite materials Part I: Constant stiffness design. *Composite Structures*, 90:1–11, 2009.

[74] ASTM-D7136/D7136M. Standard test method for measuring the damage resistance of a fiber-reinforced polymer matrix composite to a drop-weight impact event. ASTM International, American Society for Testing and Materials, West Conshohocken, PA, USA, 2007.

[75] ASTM-D7137/D7137M. Standard test method for compressive residual strength properties of damaged polymer matrix composite plates. ASTM International, American Society for Testing and Materials, West Conshohocken, PA, USA, 2007.

[76] AITM1-0010. Fiber reinforced plastics; Determination of compression strength after impact. Airbus standard, Airbus S.A.S, Blagnac Cedex, France, 2005.

[77] P. W. Harper and S. R. Hallett. Cohesive zone length in numerical simulations of composite delamination. *Engineering Fracture Mechanics*, 75:4774–4792, 2008.

[78] A. B. de Morais, M. F. de Moura, J. P. M. Gonçalves, and P. P. de Camanho. Analysis of crack propagation in double cantilever beam tests of multidirectional laminates. *Mechanics of Materials*, 35:641–652, 2003.

[79] P. Prombut, L. Michel, F. Lachaud, and J. J. Barrau. Delamination of multidirectional composite laminates at $0°/\theta°$ ply interfaces. *Engineering Fracture Mechanics*, 73:2427–2442, 2006.

[80] A. B. Pereira and A. B. de Morais. Mixed mode I+II interlaminar fracture of carbon/epoxy laminates. *Composites: Part A*, 39:322–333, 2008.

[81] J. Schön, T. Nyman, and H. Ansell. A numerical and experimental investigation of delamination behavior in the DCB specimen. *Composites Science and Technology*, 60:173–184, 2000.

[82] V. La Saponara, H. Muliana, R. Haj-Ali, and G. A. Kardomateas. Experimental and numerical analysis of delamination growth in double cantilever laminated beams. *Engineering Fracture Mechanics*, 69:687–699, 2002.

[83] J. A. Nairn. Energy release rate analysis for adhesive and laminate double cantilever beam specimens emphasizing the effect of residual stresses. *International Journal of Adhesion & Adhesives*, 20:59–70, 2000.

[84] B. D. Davidson, R. Krüger, and M. König. Three dimensional analysis of center-delaminated unidirectional and multidirectional single-leg bending specimens. *Composites Science and Technology*, 54:385–394, 1995.

[85] C. T. Sun and S. Zheng. Delamination characteristics of double-cantilever beam and end-notched flexure composite specimens. *Composites Science and Technology*, 56:451–459, 1996.

[86] E. V. González. *Simulation of interlaminar and intralaminar damage in polymer-based composites for aeronautical applications under impact loading*. PhD thesis, Universitat de Girona, 2010.

[87] M. M. Shokrieh and P. H. M. Attar. A new method for modeling of initiation and propagation of delamination between $[0/\theta]$ layers of laminated composites. *Applied Composite Materials*, 17:441–452, 2010.

[88] M. R. Wisnom. Modeling discrete failures in composites with interface elements. *Composites: Part A*, 41:795–805, 2010.

[89] ASTM-D5528. Standard test method for mode I interlaminar fracture toughness of unidirectional fiber-reinforced polymer matrix composites. ASTM International, American Society for Testing and Materials, West Conshohocken, PA, USA, 2004.

[90] M. L. Benzeggagh and M. Kenane. Measurement of mixed-mode delamination fracture toughness of unidirectional glass. *Composites Science and Technology*, 56:439–449, 1996.

[91] P. P. Camanho, C. G. Dávila, and M. F. de Moura. Numerical simulation of mixed-mode progressive delamination in composite materials. *Journal of Composite Materials*, 37:1415–1438, 2003.

[92] P. P. Camanho, C. G. Dávila, S. T. Pinho, L. Iannucci, and P. Robinson. Prediction of in situ strengths and matrix cracking in composites under transverse tension and in-plane shear. *Composites: Part A*, 37:165–176, 2006.

[93] B. D. Davidson, R. Krüger, and M. König. Effect of stacking sequence on energy release rate distributions in multidirectional DCB and ENF specimens. *Engineering Fracture Mechanics*, 55:557–569, 1996.

[94] V. Mollón, J. Bonhomme, J. Viña, and A. Argüelles. Theoretical and experimental analysis of carbon epoxy asymmetric DCB specimens to characterize mixed mode fracture toughness. *Polymer Testing*, 29:766–770, 2010.

[95] S. Bennati, M. Colleluori, D. Corigliano, and P. S. Valvo. An enhanced beam-theory model of the asymmetric double cantilever beam (ADCB) test for composite laminates. *Composites Science and Technology*, 69:1735–1745, 2009.

[96] J. Renart, N. Blanco, E. Pajares, J. Costa, S. Lazcano, and G. Santacruz. Side Clamped Beam (SCB) hinge system for delamination tests in beam-type composite specimens. *Composites Science and Technology*, 71:1023–1029, 2011.

[97] N. S. Choi. Rate effects on the delamination fracture of multidirectional carbon-fiber/epoxy composites under mode I loading. *Journal of Materials Science*, 36:2257–2270, 2001.

[98] L. Peng, J. Zhang, L. Zhao, R. Bao, H. Yang, and B. Fei. Mode I delamination growth of multidirectional composite laminates under fatigue loading. *Journal of Composite Materials*, 45:1077–1090, 2011.

[99] X. J. Gong, A. Hurez, and G. Verchery. On the determination of delamination toughness by using multidirectional DCB specimens. *Polymer Testing*, 29: 658–666, 2010.

[100] J. H. Chen, E. Schulz, J. Bohse, and G. Hinrichsen. Effect of fibre content on the interlaminar fracture toughness of unidirectional glass-fibre/polyamide composite. *Composites: Part A*, 30:747–755, 1999.

[101] N. Blanco, E. K. Gamstedt, and J. Costa. Mechanical hinge system for delamination tests in beam-type composite specimens. *Composites Science and Technology*, 68:1837–1842, 2008.

[102] F. Ducept, D. Gamby, and P. Davies. A mixed-mode failure criterion derived from tests on symmetric and asymmetric specimens. *Composites Science and Technology*, 59:609–619, 1999.

[103] ASTM-D5573. Standard practice for classifying failure modes in fiber-reinforced-plastic FRP joints. ASTM International, American Society for Testing and Materials, West Conshohocken, PA, USA, 1999.

[104] M. D. Gilchrist and N. Svensson. A fractographic analysis of delamination within multidirectional carbon/epoxy laminates. *Composites Science and Technology*, 55:195–207, 1995.

[105] M. S. Mohamed Rehan, J. Rousseau, X. J. Gong, L. Guillaumat, and J. S. M. Ali. Effects of fiber orientation of adjacent plies on the mode I crack propagation in a carbon-epoxy laminates. *Procedia Engineering*, 10:3179–3184, 2011.

[106] M. M. Shokrieh and M. Heidari-Rarani. Effect of stacking sequence on R-curve behavior of glass/epoxy DCB laminates with 0°//0° crack interface. *Materials Science and Engineering A*, 529:265–269, 2011.

[107] M. Iwamoto, Q. Q. Ni, T. Fujiwara, and K. Kurashiki. Intralaminar fracture mechanism in unidirectional CFRP composites. Part I : Intralaminar toughness and AE characteristics. *Engineering Fracture Mechanics*, 64:721–745, 1999.

[108] M. F. S. F. de Moura, R. D. S. G. Campilho, A. M. Amaro, and P. N. B. Reis. Interlaminar and intralaminar fracture characterization of composites under mode I loading. *Composite Structures*, 92:144–149, 2010.

[109] J. H. Hwang, C. S. Lee, and W. Hwang. Effect of crack propagation directions on the interlaminar fracture toughness of carbon /epoxy composite materials. *Applied Composite Materials*, 8:411–433, 2001.

[110] F. Aymerich and M. Serra. Optimization of laminate stacking sequence for maximum buckling load using the ant colony optimization (ACO) metaheuristic. *Composites: Part A*, 39:262–272, 2008.

[111] C. W. Hudson, J. J. Carruthers, and A. M. Robinson. Multiple objective optimization of composite sandwich structures for real vehicle floor panels. *Composite Structures*, 92:2077–2082, 2010.

[112] M. W. Bloomfield, J. E. Herencia, and P. M. Weaver. Analysis and benchmarking of meta-heuristic techniques for lay-up optimization. *Computers and Structures*, 88:272–282, 2010.

[113] A. Rama Mohan Rao and N. Arvind. A scatter search algorithm for stacking sequence optimization of laminate composites. *Composite Structures*, 70:383–402, 2005.

[114] N. Kogiso, L. T. Watson, Z. Gürdal, and R. T. Haftka. Genetic algorithms with local improvement for composite laminate design. *Structural optimization*, 7: 207–218, 1994.

[115] Ş. Karakaya and Ö. Soykasap. Buckling optimization of laminated composite plates using genetic algorithm and generalized pattern search algorithm. *Structural and Multidisciplinary Optimization*, 39:477–486, 2009.

[116] C. C. Lin and Y. J. Lee. Stacking sequence optimization of laminated composite structures using genetic algorithm with local improvement. *Composite Structures*, 63:339–345, 2004.

[117] G. Soremekun, Z. Gürdal, R. T. Haftka, and L. T. Watson. Composite laminate design optimization by genetic algorithm with generalized elitist selection. *Computers and Structures*, 97:131–143, 2001.

[118] A. Todoroki and T. Ishikawa. Design of experiments for stacking sequence optimizations with genetic algorithm using response surface approximation. *Composite Structures*, 64:349–357, 2004.

[119] M. T. McMahon and L. T. Watson. A distributed genetic algorithm with migration for the design of composite laminate structures. *Parallel Algorithms and Applications*, 14:329–362, 2000.

[120] S. T. IJsselmuiden, M. M. Abdalla, and Z. Gürdal. Implementation of strength-based failure criteria in the lamination parameter design space. *AIAA Journal*, 46:1826–1834, 2008.

[121] O. Erdal and F. O. Sonmez. Optimum design of composite laminates for maximum buckling load capacity using simulated annealing. *Composite Structures*, 71:45–52, 2005.

[122] A. Todoroki and M. Sekishiro. Stacking sequence optimization to maximize the buckling load of blade-stiffened panels with strength constraints using the iterative fractal branch-and-bound method. *Composites: Part B*, 39:842–850, 2008.

[123] R. Matsuzaki and A. Todoroki. Stacking-sequence optimization using fractal branch-and-bound method for unsymmetrical laminates. *Composite Structures*, 78:537–550, 2007.

[124] N. Pai, A. Kaw, and M. Weng. Optimization of laminate stacking sequence for failure load maximization using tabu search. *Composites: Part B*, 34:405–413, 2003.

[125] N. Chang, W. Wang, W. Yang, and J. Wang. Ply stacking sequence optimization of composite laminate by permutation discrete particle swarm optimization. *Structural and Multidisciplinary Optimization*, 41:179–187, 2010.

[126] M. Dorigo, V. Maniezzo, and A. Colorni. The ant system: Optimization by a colony of cooperating agents. *IEEE Journal*, 26:29–41, 1996.

[127] S. Adali, F. Lene, G. Duvaut, and V. Chiaruttini. Optimization of laminated composites subject to uncertain buckling loads. *Composite Structures*, 62: 261–269, 2003.

[128] F. X. Irisarri, D. H. Bassir, N. Carrere, and J. F. Maire. Multiobjective stacking sequence optimization for laminated composite structures. *Composites Science and Technology*, 69:983–990, 2009.

[129] C. S. Lopes, P. P. Camanho, Z. Gürdal, P. Maimí, and E. V. González. Low-velocity impact damage on dispersed stacking sequence laminates. Part II: Numerical simulations. *Composites Science and Technology*, 69:937–947, 2009.

[130] R. Satheesh, G. N. Naik, and R. Ganguli. Conservative design optimization of laminated composite structures using genetic algorithms and multiple failure criteria. *Journal of Composite Materials*, 44:369–387, 2010.

[131] R. H. Lopez, M. A. Luersen, and E. S. Cursi. Optimization of laminated composites considering different failure criteria. *Composites: Part B*, 40:731–740, 2009.

[132] M. Kober and A. Kühhorn. Development of optimized washer-shape for damage-free load application to composites. *Composite Structures*, 92:1985–1991, 2010.

[133] C. G. Dávila and P. P. Camanho. Failure criteria for FRP laminates in plane stress. Technical Report NASA/TM-2003-212663, NASA, Langley, Research Center, Hampton, November 2003.

[134] A. K. Kaw. *Mechanics of composite materials*. Taylor & Francis, Boca Raton, Florida, USA, second edition, 2006.

[135] M Dorigo and T. Stutzle. *Ant Colony optimization*. MIT Press, Massachusetts, England, 2004.

[136] S. S. Rao. *Engineering optimization theory and practice*. John Wiley & Sons, Inc., Hoboken New Jersey, fourth edition, 2009.

[137] W. Wang, S. Guo, N. Chang, and W. Yang. Optimum buckling design of composite stiffened panels using ant colony algorithm. *Composite Structures*, 92:712–719, 2010.

[138] K. H. Nguyen, J. H. Ahn, J. H. Kweon, and J. H. Choi. Optimization of composite laminates subjected to high velocity impact using a genetic algorithm. *International Journal of Aeronatical & Space Science*, 11:227–233, 2010.

[139] R. T. L. Ferreira, M. V. Donadon, and J. A. Hernandes. Structural optimization of a composite plate subjected to a small mass impact. In *Proceeding of the 2nd International Conference on Engineering Optimization, Lisbon, Portugal, 6-9 Sept. 2010*, Lisbon, Portugal, September 2010.

[140] P. O. Sjöblom, J. T. Hartness, and T. M. Cordell. On low-velocity impact testing of composite materials. *Journal of Composite Materials*, 22:30–52, 1988.

[141] S. R. Swanson. Elastic impact stress analysis of composite plates and cylinders. In S. R. Reid and G. Zhou, editors, *Impact behavior of fiber-reinforced composite materials and structures*, pages 186–211. Woodhead Publishing Limited, 2000.

[142] F. Collombet, J. Bonini, and L. Lataillade. A three-dimensional modeling of low velocity impact damage in composite laminates. *International Journal for Numerical methods in Engineering*, 39:1491–1516, 1996.

[143] G. A. O. Davies and R. Olsson. Impact on composite structures. *The Aeto-nautical Journal*, 108:541–563, 2004.

[144] M. O. W. Richardson and M. J. Wisheart. Review of low-velocity impact properties of composite materials. *Composites: Part A*, 27:1123–1131, 1996.

[145] R. Olsson. Mass criterion for wave controlled impact response of composite plates. *Composites: Part A*, 31:879–887, 2000.

[146] A. P. Christoforou and A. S. Yigit. Characterization of impact in composite plates. *Composite Structures*, 43:15–24, 1998.

[147] A. P. Christoforou. Impact dymanics and damage in composite structures. *Composite Structures*, 52:181–188, 2001.

[148] A. P. Christoforou, A. A. Elsharkawy, and L. H. Guedouar. An inverse solution for low-velocity impact in composite plates. *Computers & Structures*, 79:2607–2619, 2001.

[149] A. S. Yigit and A. P. Christoforou. Limits of asymptotic solutions in low-velocity impact of composite plate. *Composite Structures*, 81:568–574, 2007.

[150] A. P. Christoforou and A. S. Yigit. Scaling of low-velocity impact response in composite structures. *Composite Structures*, 91:358–365, 2009.

[151] A. P. Christoforou, A. S. Yigit, W. J. Cantwell, and S. Wang. Impact response characterization in composite plates-Experimental validation. *Applied Composite Materials*, 17:463–472, 2010.

[152] S. R. Swanson. Limits of quasi-static solutions in impact of composite structures. *Composites Engineering*, 2:261–267, 1992.

[153] S. Abrate. Modeling of impacts on composite structures. *Composite Structures*, 51:129–138, 2001.

[154] R. Olsson. Closed form prediction of peak load and delamination onset under small mass impact. *Composite Structures*, 59:341–349, 2003.

[155] R. Olsson. Analytical model for delamination growth during small mass impact on plates. *International Journal of Solids and Structures*, 47:2884–2892, 2010.

[156] A. P. Christoforou and A. S. Yigit. Effect of flexibility on low velocity impact response. *Journal of Sound and Vibration*, 217:563–578, 1998.

[157] A. S. Yigit and A. P. Christoforou. Impact dynamics of composite beams. *Composite Structures*, 32:187–195, 1995.

[158] S. Abrate. *Impact on composite structures.* Cambridge University Press, Cambridge, UK, second edition, 1998.

[159] X. Zhang, G. A. O. Davies, and D. Hitchings. Impact damage with compressive preload and post-impact compression of carbon composite plates. *International Journal of Impact Engineering*, 22:485–509, 1999.

[160] D. Liu. Impact-induced delamination - A view of bending stiffness mismatching. *Journal of Composite Materials*, 22:674–692, 1988.

[161] H. Morita, T. Adachi, Y. Tateishi, and H. Matsumot. Characterization of impact damage resistance of CF/PEEK and CF/toughened epoxy laminates under low and high velocity impact tests. *Journal of Reinforced Plastics and Composites*, 16:131–143, 1997.

[162] W. C. Jackson and C. C. Poe. Use of impact force as a scale parameter for the impact response of composites laminates. *Journal of Composites Technology and Research*, 15:282–289, 1993.

[163] G. A. O. Davies and X. Zhang. Impact damage prediction in carbon composite structures. *International Journal of Impact Engineering*, 16:149–170, 1995.

[164] H. Saito, M. Morita, K. Kawaba, M. Kanesaki, H. Takeuchi, M. Tanaka, and I. Kimpara. Effect of ply-thickness on impact damage morphology in CFRP laminates. *Journal of Composite Materials*, 30:1097–1106, 2011.

[165] V. Tita, J. de Carvalho, and D. Vandepitte. Failure analysis of low velocity impact on thin composite laminates: Experimental and numerical approaches. *Composite Structures*, 83:413–428, 2008.

[166] H. Suemasu and O. Majima. Multiple delaminations and their severity in circular axisymmetric plates subjected to transverse loading. *Journal of Composite Materials*, 30:441–453, 1996.

[167] R. Olsson, M. V. Donadon, and B. G. Falzon. Delamination threshold load for dynamic impact on plates. *International Journal of Solids and Structures*, 43:3124–3141, 2006.

[168] G. Caprino and V. Lopresto. On the penetration energy for fibre-reinforced plastics under low-velocity impact conditions. *Composites Science and Technology*, 61:65–73, 2001.

[169] G. Caprino, A. Langella, and V. Lopresto. Indentation and penetration of carbon fibre reinforced plastic laminates. *Composites: Part A*, 34:319–325, 2003.

[170] L. S. Sutherland and C. Guedes Soares. Scaling of impact on low fibre-volume glass-polyester laminates. *Composites: Part A*, 38:307–317, 2007.

[171] S. T. Chiu, Y. Y. Liou, Y. C. Chang, and C. L. Ong. Low velocity impact behavior of prestressed composite laminates. *Material Chemistry and Physics*, 47:268–272, 1997.

[172] F. Mili and B. Necib. The effect of stacking sequence on the impact-induced damage in cross-ply e-glass/epoxy composite plates. *Archive of Applied Mechanics*, 97:1019–1031, 2009.

[173] R. Craven, P. Sztefek, and R. Olsson. Investigation of impact damage in multi-directional tape laminates and its effect on local tensile stiffness. *Composites Science and Technology*, 68:2518–2525, 2008.

[174] E. V. González, P. Maimí, P. P. Camanho, A. Turon, and J. A. Mayugo. Simulation of drop-weight impact and compression after impact tests on composite laminates. *Composite Structures*, 94:3364–3378, 2012.

[175] G. Caprino, V. Lopresto, C. Scarponi, and G. Briotti. Influence of material thickness on the response of carbon- fabric/epoxy panels to low velocity impact. *Composites Science and Technology*, 59:2279–2286, 1999.

[176] G. Caprino and V. Lopresto. The significance of indentation in the inspection of carbon fibre- reinforced plastic panels damaged by low-velocity impact. *Composites Science and Technology*, 60:1003–1012, 2000.

[177] O. S. David-West, N. V. Alexander, D. H. Nash, and W. M. Banks. Energy absorption and bending stiffness in CFRP laminates: The effect of 45° plies. *Thin-Walled Structures*, 46:860–869, 2008.

[178] Z. Aslan and M. Sahin. Buckling behavior and compressive failure of composite laminates containing multiple large delaminations. *Composites Structures*, 89: 382–390, 2009.

[179] X. W. Wang, I. Pont-Lezica, J. M. Harris, F. J. Guild, and M. J. Pavier. Compressive failure of composite laminates containing multiple delaminations. *Composite Science and Technology*, 65:191–200, 2005.

[180] F. K. Chang, R. A. Scott, and G. S. Springer. The effect of laminate configuration on characteristic lengths and rail shear strength. *Journal of Composite Materials*, 18:290–296, 1984.

[181] D. L. Flaggs and M. H. Kural. Experimental determination of the in situ transverse lamina strength in graphite/epoxy laminates. *Journal of Composite Materials*, 16:103–116, 1982.